Charles University in Prague

Faculty of Mathematics and Physics

DOCTORAL THESIS

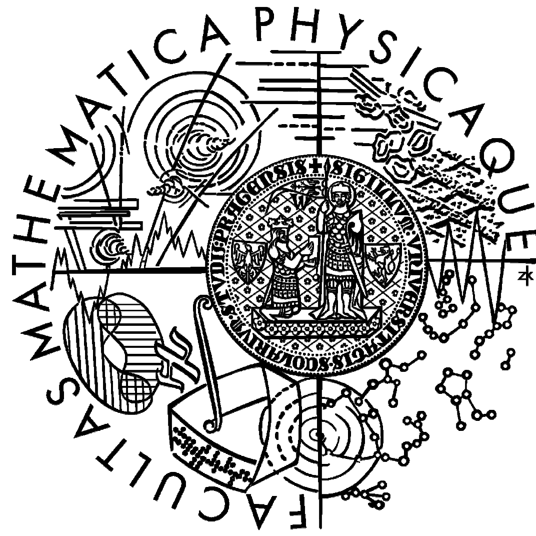

Marek Bugár

Dynamics of structural defects in CdTe-based semiconductors

Institute of Physics

Supervisor: Doc. Ing. Eduard Belas CSc.

Quantum optics and optoelectronics

Prague 2011

Acknowledgement

I would like to thank especially my supervisor Doc. Ing. Eduard Belas, CSc. for the procreative discussions about the ideas of the work and experiments. I am grateful to Doc. RNDr. Roman Grill, CSc. for theoretical discussions. I am also thankfull to Prof. Ing. Jan Franc, DrSc. and other colleagues at the Institute of Physics at Charles University in Prague for their help in my research and study.

I would like to acknowledge Prof. Dr. rer. nat. Georg Nachtwei for guidance during my stay in Germany. I would like to thank the Braunschweig International Graduate School of Metrology for the financial support of the part of my PhD study.

I declare that I carried out this doctoral thesis independently, and only with the cited sources, literature and other professional sources.

I understand that my work relates to the rights and obligations under the Act No. 121/2000 Coll., the Copyright Act, as amended, in particular the fact that the Charles University in Prague has the right to conclude a license agreement on the use of this work as a school work pursuant to Section 60 paragraph 1 of the Copyright Act.

Prague, 14.6.2011 Marek Bugár

Název práce: Dynamika strukturních defektů v polovodičích CdTe

Autor: RNDr. Marek Bugár

Ústav: Fyzikální ústav Univerzity Karlovy v Praze

Vedoucí doktorské práce: Doc. Ing. Eduard Belas CSc.; Fyzikální ústav Univerzity Karlovy v Praze

Abstrakt: Práce je zaměřena na výzkum vlivu žíhání na strukturní, elektrické a optické vlastnosti epitaxních podložek na bázi CdZnTe a detektorů rentgenového a gama záření na bázi CdTe a CdZnTe. První část práce zkoumá strukturní vlastnosti mikrodefektů – inkluzí – snižujících kvalitu obou typů materiálů a je zaměřena na nalezení efektivního žíhacího procesu pro jejich odstranění. V případě podložek CdZnTe se žíhací experimenty zaměřují také na nalezení temperančních podmínek zvyšujících jejich infračervenou propustnost. V detektorech vysokoenergetického záření je cílem žíhacích experimentů také zachování vysokoodporového stavu materiálu. Práce obsahuje také měření transportních vlastností CdTe přímo při vysokých teplotách.

Klíčová slova: CdTe, žíhaní, inkluze, detektor, defekty

Title: Dynamics of structural defects in CdTe-based semiconductors

Author: RNDr. Marek Bugár

Institute: Institute of Physics, Charles University in Prague

Supervisor of the doctoral thesis: Doc. Ing. Eduard Belas CSc.; Institute of Physics, Charles University in Prague

Abstract: The work is aimed at investigation of the effect of annealing on structural, electrical and optical properties of CdZnTe epitaxial substrates and CdTe-based and CdZnTe-based X-ray and gamma-ray detectors. The first part of the work is focused on investigation of structural properties of one type of second phase defects – inclusions – present in the material, which degrade the material quality. Consequent annealing experiments are aimed at reduction of these defects. In case of CdZnTe substrates, an annealing treatment leading to an increase of the infrared transmittance is investigated. On the other hand, annealing experiments on detectors of high-energetic radiation are focused on preservation of the high-resistive state. Moreover, the work contains detailed measurements of transport properties of CdTe taken directly at high temperatures.

Key words: CdTe, annealing, inclusions, detectors, defects

Contents

Introduction **1**

1. Properties of CdTe **3**
1.1. Crystal structure 3
1.2. Mechanical properties 3
1.3. Band structure 4
1.4. Crystal growth 5
1.4.1. Equilibrium solidification 5
1.4.2. Steady-state solidification 7
1.4.3. Crystal growth methods 7
1.4.4. Growth of CdTe crystals 9
1.5. Point defects 12
1.5.1. Native point defects 12
1.5.2. Extrinsic point defects 14
1.5.3. Compensation of CdTe 14
1.5.4. Segregation of extrinsic defects 16
1.6. Line defects 17
1.7. Plane defects 17
1.8. Second phase defects 18
1.8.1. Inclusions 18
1.8.2. Precipitates 19
1.9. Chemical diffusion 20
1.10. Transport properties 21
1.11. Optical properties 22
1.11.1. Photoluminescence 22
1.11.2. Infrared transmittance 23
1.12. Detection of X-ray and γ-ray radiation 24

2. Experimental techniques **27**
2.1. Crystal growth 27
2.2. Sample preparation 29
2.3. Annealing 30
2.4. Microscopes 30
2.4.1. Infrared microscope 30
2.4.2. Optical microscope 31
2.4.3. Scanning electron microscope 32
2.5. Transport measurements 32
2.5.1. Hall effect measurements at room temperature 32
2.5.2. COREMA 34
2.5.3. High-temperature "*in-situ*" Hall effect measurements 35
2.6. Optical properties 36
2.6.1. Infrared transmittance 36
2.6.2. Photoluminescence 37

2.7. Detection system 37

Results and discussion **39**

3. Elimination of second phase defects **39**
3.1. Introduction 39
3.2. Characterization of star-shaped inclusions 41
3.3. Characterization of triangle-shaped inclusions 43
3.4. Inclusion reduction 45
3.4.1. Annealing of crystals with Cd inclusions 45
3.4.2. Effect of the post-anneal cooling rate 48
3.4.3. Annealing of crystals with Te inclusions 50
3.5. Resistivity restoration of CdTe:Cl crystals 53
3.5.1. As-grown samples 53
3.5.2. The first annealing step – annealing in Cd vapor 54
3.5.3. The second annealing step – re-annealing in Te vapor 54
3.5.4. Photoluminescence spectra 58
3.5.5. Gamma-ray and Alpha-particle spectra 59
3.6. Summary 61

4. High-temperature transport properties of CdTe **62**
4.1. Introduction 62
4.2. "*In-situ*" high-temperature Hall effect measurements of undoped CdTe, CdTe:In and CdTe:Cl 63
4.3. Non-standard double relaxation 67
4.4. "*In-situ*" measurement of the second Te-rich annealing of two-step annealing 70
4.5. Summary 72

5. Infrared transmittance of CdTe **73**
5.1. Introduction 73
5.2. Annealing followed by a slow cooling 73
5.3. Annealing followed by a fast cooling 76
5.4. As-grown crystals highly doped by In and Cl 77
5.5. Absorption coefficient analysis 78
5.6. Summary 79

Conclusions **80**

References **82**

Introduction

A development of materials with semiconducting properties in the early 1950-ies led to a huge expansion of semiconductor technology based mainly on Si and Ge. Later also alternative semiconducting III-V and II-VI compound materials, like GaAs or CdTe, were explored and investigated. The first comprehensive study of CdTe material was published in 1959 by de Nobel [1], in which basic structural, electrical and optical properties of this material were described. Advantages of CdTe comparing to other wide-spread semiconductors were a direct band gap, high mobility of carriers and high atomic number. On the other hand, the toxicity of cadmium for the human body and rareness of tellurium have damped the expansion of the compound in commercial applications. Despite these aspects, materials based on CdTe have found utilization in various areas of the optoelectronic industry.

Undoped CdTe can be used for preparation of detecors of X-ray and gamma-ray radiation and is also used in the solar cells industry. Moreover, CdTe has one of the largest electro-optic coefficient of the linear electro-optic effect among II-VI compound crystals and in 1970s became an attractive choice as modulator for infrared lasers working at λ=10.6µm [2]. $Cd_{1-x}Zn_xTe$ is used as substrate for the epitaxial growth of $Hg_{1-x}Cd_xTe$ infrared detectors and also as detector of high energetic photons.

One of the biggest advantage of $Hg_{1-x}Cd_xTe$ materials is their suitability for preparation of infrared radiation detectors [3,4,5]. Since CdTe-related materials have a direct band gap structure, they exhibit strong optical absorption in the infrared region. The possibility of tuning the width of the energy bang gap by incorporation of Hg instead of Cd atoms enables preparation of infrared detectors with a tunable maximal detectivity in the range of λ=1-30µm. Since the absorption of IR light in HgCdTe is strong, the thickness of HgCdTe detector is usually ~10µm. Thinner layers lead to weaker absorption efficiency and, on the other hand, thicker material decreases the signal to noise ratio. HgCdTe layers are prepared by polishing of a bulk material produced by the Bridgman method to desirable thickness, or are prepared by deposition on a suitable substrate using an epitaxial technique (LPE, VPE, MOCVD, MBE). Infrared detectors are produced as backside illuminated detectors, where IR radiation passes through the substrate and is absorbed in a HgCdTe epilayer deposited on the substrate backside. Hence, substrates should exhibit minimal absorption of the incident IR light, their lattice constant should be close to the lattice constant of HgCdTe layer due to the interface stress minimization and should have similar thermal expansion coefficient as readout silicon electronics. Concerning these demands, several possible materials like Si, Ge, sapphire or CdZnTe can be taken into account. Among these substrates, CdZnTe has a relatively high transmissivity in the infrared region (above 60%), an excellent matching of the lattice constants and an acceptable difference of the thermal expansion comparing to the silicon-based readout electronics. These reasons have led to a proliferation of CdTe-based substrates in the infrared imaging industry. With improving of the epitaxial layer quality and minimization of pixels in IR array detectors was found out, that structural defects on the substrate surface (especially inclusions with the size up to tens of micrometers) significantly affect the quality of deposited epitaxial films [6,7,8].

CdTe-based material has also found utilization as room temperature X-ray and γ-ray detectors. From the 19th century a photographic plate has been used for detection of X-ray and gamma-ray radiation. During the second part of the 20th century the photographic plate was

replaced by ionization chambers and scintillators. From mid-nineties materials based on semi-insulating CdTe showed increased interest to be used in applications, which require high resolution and spectroscopic imaging in medical and security industry [9]. Advantages of CdTe material comparing to other wide-spread semiconductors (like Si:Li, Ge:Li, high purity Ge (HPGe) or HgI_2) are the absorption efficiency of high-energetic photons due to high atomic number Z and wide band gap allowing the fabrication of a highly resistive material ($\rho>10^8\Omega$cm) enabling the usage of detectors at room temperature. In recent years, problems with charge collection efficiency due to the detector polarization and the presence of second phase defects have limited the improvement of the detector quality.

In the first part of this work a theory of the crystal growth, defects present in the material and basic properties of CdTe is summarized. The following section describes used experimental techniques and the last part is focused on presentation of original results. Research is aimed at analysis of second phase defects present in CdTe and their reduction by a post-growth thermal treatment. Moreover, in case of substrate-grade CdZnTe material, annealing experiments are also focused on improvement of the infrared transmittance in the application interesting region at about $\lambda\sim10\mu$m. In case of CdTe-based radiation detectors, the thermal treatment is aimed at conservation of the material resistivity at value above $\rho>10^8\Omega$cm. One chapter is devoted to "*in-situ*" high-temperature transport measurements of CdTe crystals with different doping. The last part of the work deals of an influence of an annealing treatment under various annealing conditions on the infrared transmittance of CdTe in the energy range of 0.1-1.5eV. The work is finished by the summary of obtained results and their interpretation.

1. Properties of CdTe

1.1. Crystal structure

II-VI compound cadmium telluride (CdTe) crystallizes in a cubic zinc-blende structure. This structure is formed by a pair of interpenetrating face centered cubic (fcc) sublattices offset from each other by one quarter of a unit cell body diagonal (Fig.1.1). One sublattice contains only Cd atoms, the second one only Te atoms. The lattice constant of stoichiometric CdTe is 6.4825Å. Chemical bonds between cadmium and tellurium atoms are ionic-covalent with prevalent portion of the ionic bond (Fig.1.2). Atomic orbitals are mixed and form new sp^3 hybrid orbitals.

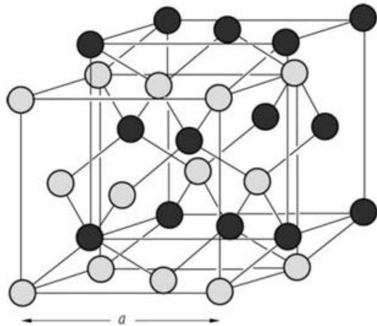

Fig.1.1: Zinc-blende crystal structure [10].

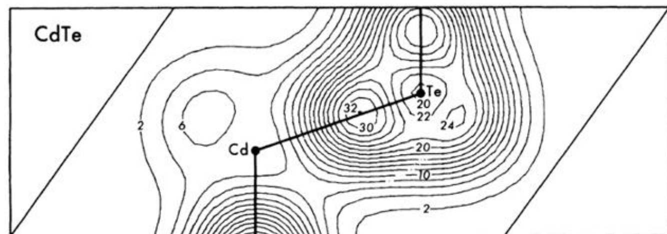

Fig.1.2: Valence charge densities of CdTe [11].

1.2. Mechanical properties

Plastic deformation and stress experiments indicate that CdTe has low hardness at all temperatures and especially near the melting point [12]. The density of CdTe is 5.85 g/cm^3 and the

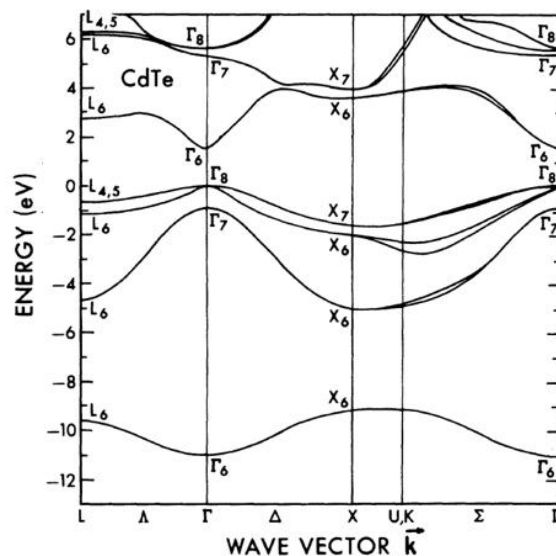

Fig.1.3: Band structure of CdTe [11].

hardness is approximately 45 kg/mm^2.

1.3. Band structure

CdTe is a semiconductor with a direct band gap structure with the forbidden gap of about 1.5eV at room temperature. The band structure has been acquired using various numerical (density functional theory, nonlocal pseudopotential method, local density approximation) and experimental (reflectivity, transmisivity, X-ray measurements) methods [10] and is plotted in Fig.1.3. The valence band consists of three bands, two of them are degenerated at $\vec{k} = 0$, the third sub-band is split-off by the spin-orbital coupling. The conduction band and the light hole valence band are non-parabolic.

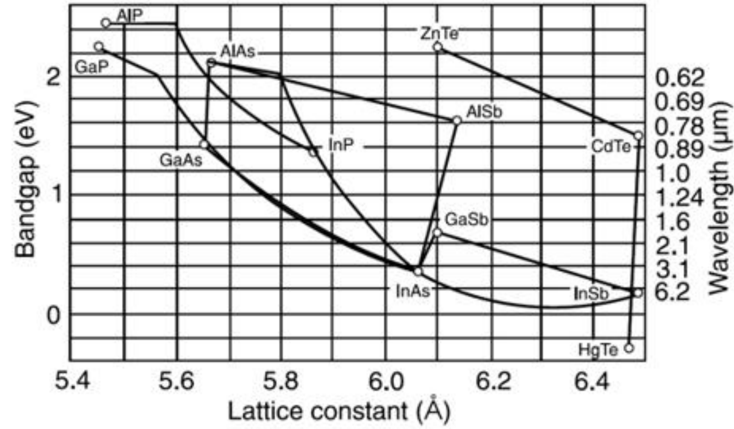

Fig.1.4: Modulation of band gap and lattice constant of CdTe by incorporation of Zn or Hg instead of Cd atoms [13].

The width of CdTe bandgap depends on the temperature *T* and external pressure *P*. Recently, the temperature dependence of the bandgap was measured up to 1000K with the result [14]:

$$E_g(T) = 1.5860 - 5.9117 \times 10^{-4} \frac{T^2}{(T + 160)} \tag{1.1}$$

Isothermal compression measurements lead to a more general term [15]:

$$E_g(T, P) = 1.606 + 0.070P - 3.763 \times 10^{-4} \frac{T^2}{(T + 60.28)} \tag{1.2}$$

The forbidden band gap width at room temperature can be modulated by a substitution of Cd atoms by atoms of Zn or Hg in the cadmium sublattice. The possibility of preparation of ternary compounds $Hg_xCd_{1-x}Te$ or $Cd_xZn_{1-x}Te$ enables to prepare materials with a bandgap in the energy range of 0-2.5eV (Fig.1.4). Another important parameter, especially in the infrared detector industry, is also the lattice constant of the material. Commercially interesting infrared detectors $Hg_{0.8}Cd_{0.2}Te$ are mostly grown on $Cd_{0.96}Zn_{0.04}Te$ substrates due to matching of lattice constants, which suppress the formation of an interface stress.

1.4. Crystal growth

In this chapter the basic thermodynamic theory of solidification and various technologies of crystal growth will be described based on [16]. The last part of the chapter is focused on a description of CdTe crystallization using the Bridgman method.

1.4.1 Equilibrium solidification

At the beginning of the crystal growth, the starting material is inserted to the ampoule and warmed-up slightly up to the melting temperature, then the material is held at temperature above the melting point for homogenization of the melt. Afterwards, the temperature of the melt slowly decreases down to the room temperature. The transformation of the melt to solid can be described by processes in a thermodynamic system as changes of thermodynamic potentials. Processes at constant pressure during which the volume is changed only slightly, what corresponds with the solidification of the melt, can be described by a change of the free energy F:

$$dF = dU - TdS - SdT \tag{1.3}$$

where U is the internal energy, S is the entropy and T is temperature. On the other hand, the stability of the thermodynamic system is characterized by the minimum of the Gibbs free energy G:

$$dG = dH - TdS - SdT = dU - TdS - SdT + VdP + pdV \tag{1.4}$$

where H is the enthalpy, V is the volume and P is the pressure of the system. In case of isobaric and isochoric processes the last two equation terms in equation (1.4) can be neglected. This leads to formally identical equations (1.3) and (1.4). Hence, for description of stability of the thermodynamic system the minimum of the free energy can be used. Minimums of the free energy in dependence on the system composition and system temperature can be derived and plotted as *an isobaric phase T-x diagram*. Fig.1.5 shows simplified phase *T-x* diagram of binary compound formed from components A and B. At high temperatures above the liquidus line, the system consists of a liquid solution; between the liquidus and solidus line the system consists of the mixture of a liquid solution and solid and bellow the solidus line the system consists of solid.

Ideally, an infinitely slow temperature decrease of the liquid phase and its transformation (so called equilibrium solidification) to the solid is plotted in Fig.1.6 (detail of the Fig.1.5). At temperature T_1 the equilibrium state is given by the point 1 in the phase diagram. At this state, the

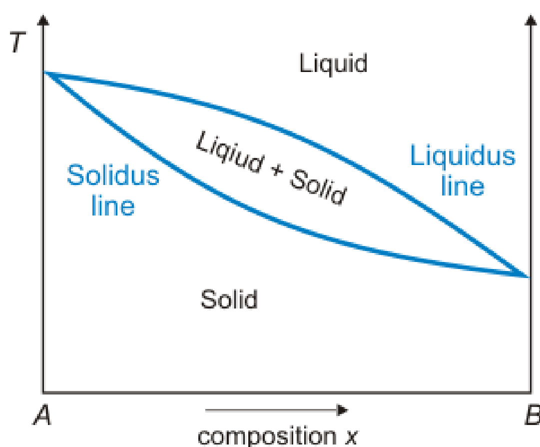

Fig.1.5: Equilibrium isobaric phase T-x diagram of the binary compound.

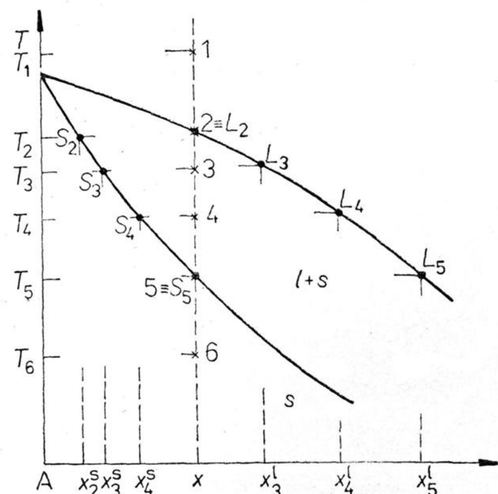

Fig.1.6: Temperature dependence of the liquid and solid phase composition during equilibration solidification [17].

whole system consists of the liquid solution with the composition *x*. When the temperature reaches the value T_2, the system state is given by the point 2 laying on the liquidus curve and particles of the solid phase appear. The composition of appearing particles x_2^S is given by the point S_2 on the solidus line, the composition of the liquid solution remains *x*. During a gradual decreasing of the temperature to values T_3 and T_4 the system phase state is given by points 3 and 4 inside of the two-phase area between the liquidus and solidus lines. The composition of the solid phase is gradually changing ($S_2 \rightarrow S_3 \rightarrow S_4 \rightarrow ..$) as well as the composition of the liquid solution ($L_2 \rightarrow L_3 \rightarrow L_4 \rightarrow ..$). Mutual ratio of the liquid phase (*l*) and the solid phase (*s*) in the saturated solution (*l*+*s*) is given by *the lever rule:*

$$n_l(x - x_l) = n_s(x_s - x) \tag{1.5}$$

where *x* is the system composition, x_l and x_s are molar atomic fractions of liquid and solid, n_l and n_s is a material amount in the liquid and solid phase, respectively. Since the first solid particles solidify with the composition S_2, it is necessary to suppose, that the temperature decrease is slow enough to equilibration of the composition differences in particles solidified at different temperatures by a diffusion mechanism. At temperature T_5 all liquid droplets solidify. At temperature T_6 the whole system consist of one-phase solid material with the composition *x* and the crystal ingot has the same composition *x* along its entire length.

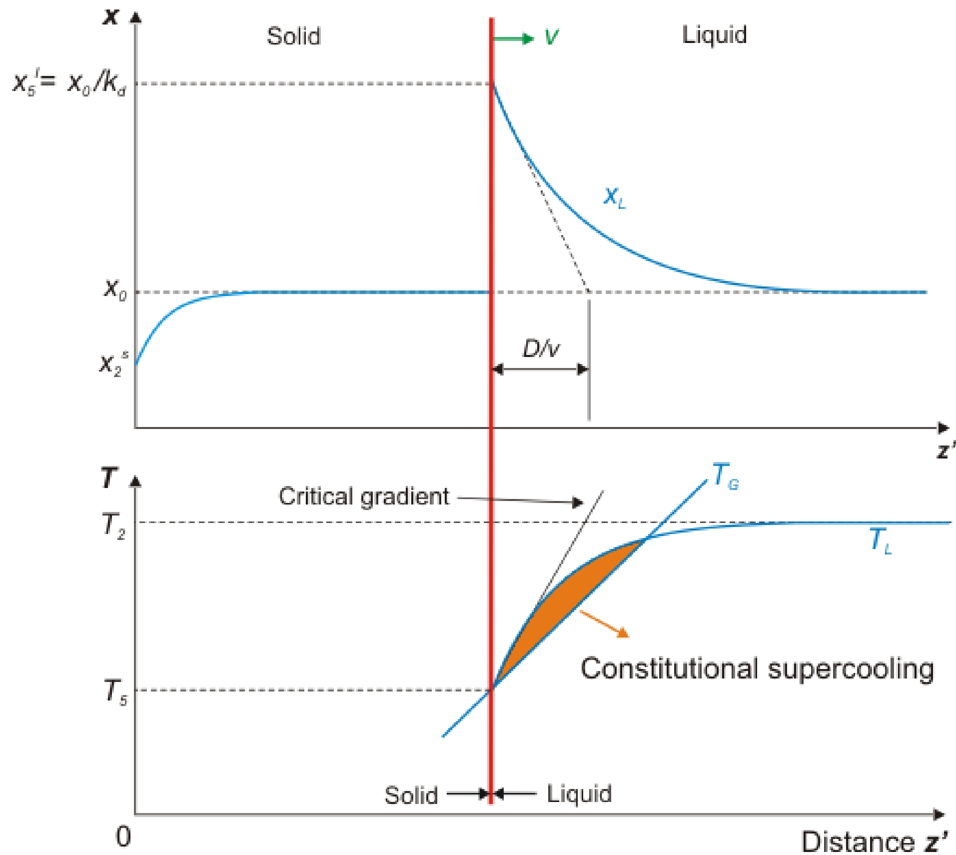

Fig.1.7: The profile of the accumulation layer across of the crystallization interface during steady-state solidification and the origin of the constitutional supercooling ahead of the planar solidification front.

1.4.2. Steady-state solidification

In practice, the cooling rate during the compound solidification is too rapid to allow substantial diffusion in the solid phase. In addition, there is only a weak stirring or convection in the melt. The solute (enriched by a component B with the composition L_2 in Fig.1.6) rejected from the solid with the composition S_2 in Fig.1.6 is only transported away by diffusion. Hence, a zone enriched by a component B appears in the liquid phase ahead of the crystallization interface. This situation is sketched in Fig.1.7. If the solidification proceeds at a constant rate v, it can be shown that the steady state is finally obtained when the interface temperature reaches T_5 in Fig.1.6. The liquid adjacent to the solid then has a composition x_0/k_d and the solid is formed with the bulk composition x_0 (corresponds to the composition x in Fig.1.6). This situation is called *a steady-state solidification*. From the solution of the diffusion equation for steady-state growth it can be written the concentration profile in the liquid:

$$x_L = x_0\left[1 + \frac{1-k_d}{k_d}\exp\left(-\frac{x}{\left(D/v\right)}\right)\right] \tag{1.6}$$

where D is diffusivity in the liquid and k_d is a segregation coefficient of the component B:

$$k_d = \frac{x_S}{x_L} \tag{1.7}$$

where x_S and x_L are the mole fractions of the component B in the solid and liquid in equilibrium at given temperature, respectively. In (1.6) x_L decreases exponentially from x_0/k_d at the interface to x_0 at large distances from the interface. The concentration profile has a characteristic width of D/v.

As a result of the varying liquid concentration ahead of the solidification front there is a corresponding variation of the solidification temperature (the liquidus temperature) given by the line T_L in Fig.1.7. On the other hand, the actual temperature of the liquid follows line such as T_G. If applied temperature gradient represented by T_G is less than the critical value shown in Fig.1.7 the liquid in front of the solidification interface exists below its equilibrium melting temperature and is *supercooled*. At this state, thermodynamic instabilities at the crystallization front and a premature solidification leading to creation of second phase defects enriched by a component B can occur. Therefore, for the most stable steady-state crystallization an applied temperature gradient should be as close as possible to the critical gradient sketched in Fig.1.7.

1.4.3. Crystal growth methods

Until these days various growth methods for preparation of compound crystals have been developed. The most frequent methods and their derivations are based on the Czochralski and Bridgman method, which are described in the following section.

Czochralski method

Generally, the Czochralski method is one of the most widespread method used for semiconducting crystals preparation. The technique is based on pulling of the crystal from the melt. At the beginning, a seed crystal, mounted on a rod, is dipped into the molten material and pulled upwards. Simultaneously with crystal pulling, the crystal rod and a crucible with a melt rotate in

opposite direction. Unfortunately, this growth technique is not suitable for CdTe preparation due to large temperature instabilities and high thermal stress during solidification.

Bridgman method

This technique is based on solidification of the melt sealed in an ampoule moving in the temperature gradient. During the crystal growth one ampoule end is held at lower temperature to define a component vapor pressure of the system (P_{Cd}). The melt composition is controlled by the vapor pressure leading to crystallization of the material with well defined composition. The growth proceeds by a mechanical movement of the ampoule or the furnace (Fig.1.8), respectively. Many modifications of the Bridgman method have been developed until these days. In the industrial production both vertical and horizontal configuration is used.

Vertical gradient freeze method

The Vertical Gradient Freeze (VGF) technique is a relatively simple modification of the Bridgman method. Temperature gradient necessary for the solidification of the melt is not shifted mechanically, but is modulated electronically in the furnace coil (Fig.1.8). Both, Bridgman and VGF techniques are widely used for production of $Cd_{0.96}Zn_{0.04}Te$ substrates and $Cd_{0.9}Zn_{0.1}Te$:In(or Al) detectors.

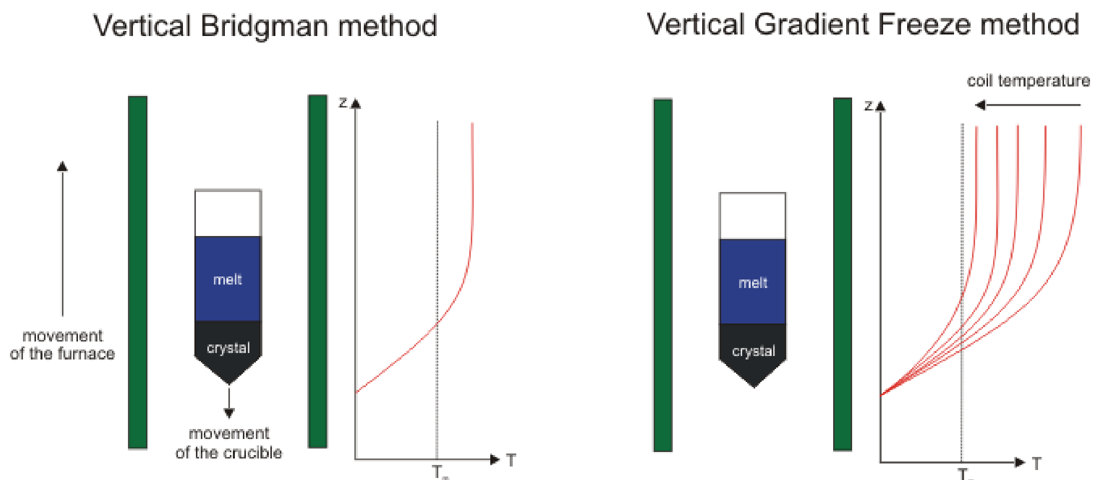

Fig.1.8: The difference between the Bridgman and the Vertical Gradient Freeze method. Bridgman method is based on a mechanical movement of the crucible or a mechanical movement of the furnace resulting in a change of the temperature gradient. Contrary to this, the temperature gradient in VGF method is gradually shifted electronically along the ampoule.

Travelling heater method

The zone refining technique is a method developed to purification of metal elements from impurities. Analogous method has been utilized for purification of crystals or even crystal growth and is called "*Travelling heater method*" (THM). Polycrystalline material is placed into an evacuated chamber or into an inert gas purge. A movable radio-frequency heating coil is used to produce local melted zone moving from the top to the end of the polycrystal. Floating zone engorges impurities with segregation coefficient lower than 1 (e.g. Na, Li, Ag, K..[18]) and usually monocrystalic material is solidified behind the floating zone. The moving rate of the zone is very

slow (<5mm/day) to suppress the constitutional supercooling effect. This method is successfully used for production of high-resistive CdTe:Cl detectors.

1.4.4. Growth of CdTe crystals

Prevalent growth techniques used for preparation of CdTe crystals are derived from the Bridgman method (vertical BM, horizontal BM, VGF) or from the THM technique. In the

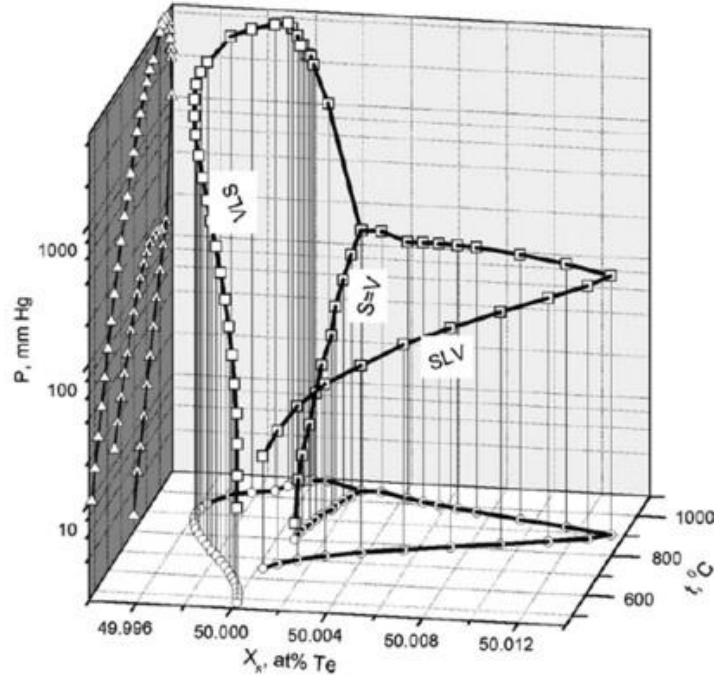

Fig.1.9: 3D illustration of 3-phase line denoted VLS and SLV are shown (from [19]). VLS curve represents cadmium saturated part of the 3-phase line, SLV depicts tellurium saturated part of the 3-phase line. S=V represents the sublimation line.

following text, thermodynamic aspects of the CdTe crystal growth using the Bridgman method will be described.

CdTe is a binary compound. If the thermodynamic system contains φ phases and consists of c components, then the number of degrees of freedom Φ is given by the Gibbs phase rule $\Phi = c - \varphi + 2$. During CdTe solidification two phases (liquid and solid, φ=2) and two components Cd and Te (c=2) are present and the number of degrees of freedom is then equal 2. Therefore, for a given compound composition the equilibrium can be achieved in a certain interval of intensive quantities – temperature and pressure of the system. This leads to formation of a three-dimensional system given by the system composition x, temperature T and partial pressure P. Part of the 3-dimensional P-T-x phase diagram (solidus and liquidus lines) is displayed in Fig.1.9 [19]. As can be seen, properties of the system are hardly readable within the 3D-phase diagram and its projections into T-x diagram (Fig.1.10) and P-T diagram (Fig.1.11) are usually used for the system description.

The equilibrium T-x diagram is plotted in Fig.1.10. In the region 1 melt with given composition is in the thermodynamic equilibrium, the region 2 corresponds to the mixture of solid and melt, in the region 3 a solid state is in the equilibrium and finally the 4th region represents two solid phases with different compositions. The region 3 determinate by the solidus line constitutes

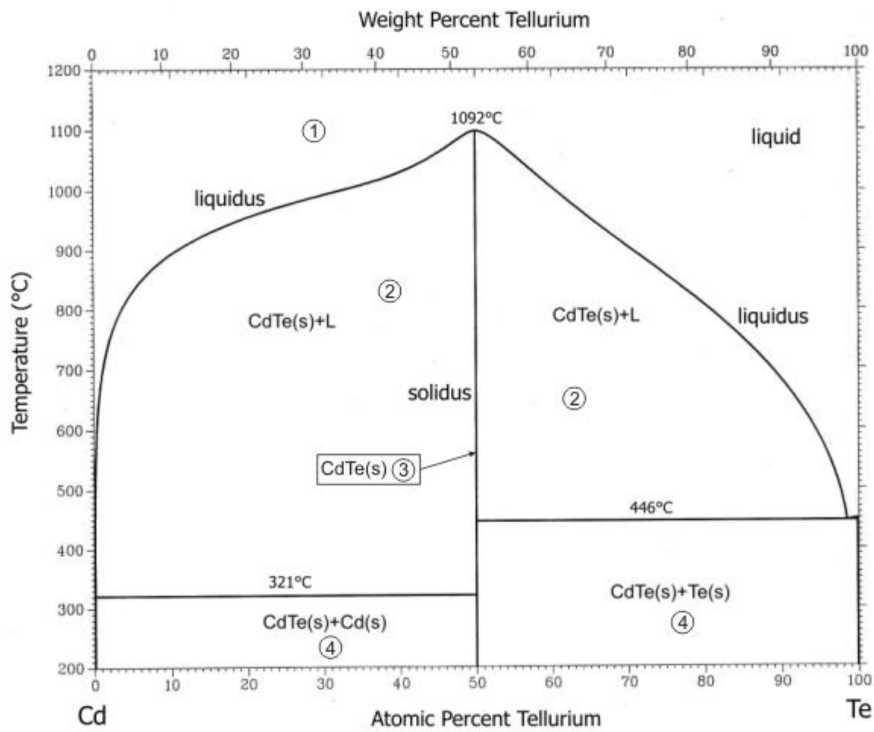

Fig.1.10: Equilibrium *T*-*x* diagram of CdTe [20].

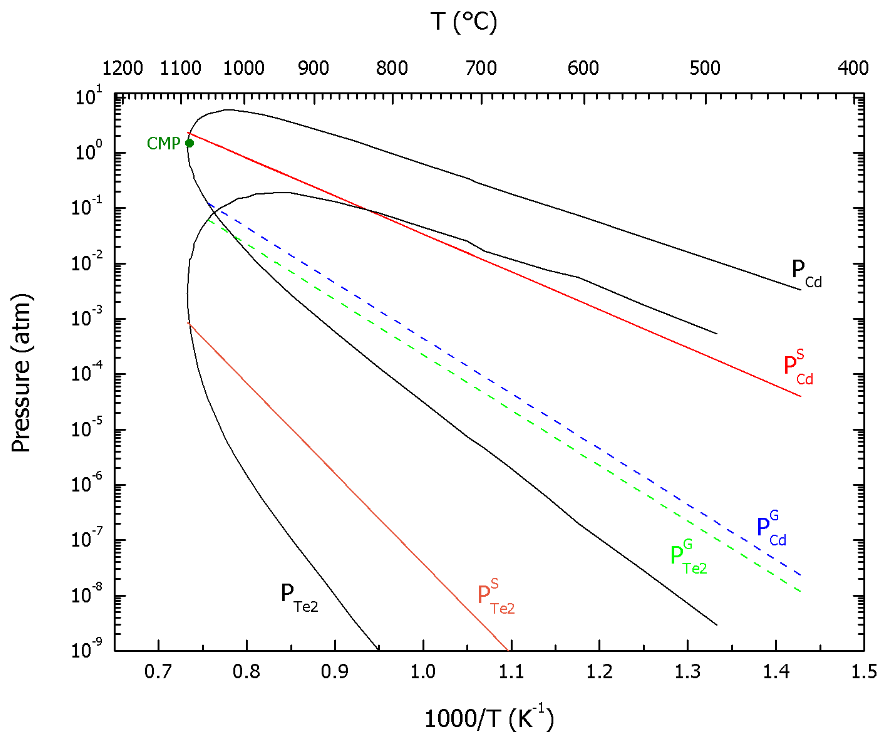

Fig.1.11: Equilibrium *P*-*T* diagram of CdTe (based on [21]). P_{Cd} and P_{Te_2} represent the 3-phase line at pressure given by cadmium and tellurium vapor, respectively. P^S_{Cd} and $P^S_{Te_2}$ are the stoichiometric lines and P^G_{Cd} and $P^G_{Te_2}$ are the sublimation lines.

the stability region of the CdTe compound.

The second projection of the 3-D *P-T-x* diagram forms the equilibrium *P-T* diagram showed in Fig.1.11. The stability region is defined by the area within the 3-phase line, at which all three phases (solid, liquid and vapor) are in the equilibrium. The stoichiometric line describes the situation, when the atomic ratio of Cd and Te in the crystal lattice is 1:1. The sublimation line represents an equilibrium state of the solid and vapor phase leading to sublimation of the solid material.

Beside the certain composition of the melt, temperature at the crystallization interface and pressure of the system has to be controlled during the crystallization. From the equilibrium thermodynamics and the Pascal law implies that pressure of the system is determined by the pressure in the coldest place of the system. The pressure is then controlled by the partial pressure formed above the cadmium (tellurium) source placed in the coldest place of the evacuated system. The pressure of the system is determined by the Dalton's law at constant temperature and volume:

$$P_{tot} = P_{Cd} + P_{Te_2} \quad (1.8)$$

Partial pressures are linked by the equilibrium constant:

$$P_{Cd} P_{Te_2}^{1/2} = \exp\left(\frac{G^0}{RT}\right) = K_{CdTe} \quad (1.9)$$

where R is molar gas constant and G^0 is a standard Gibbs potential (standard state for gasses is usually an ideal gas at pressure 101.325kPa at given temperature). Experimental temperature dependence of G^0 is [22]:

$$\Delta G^0 = -2.975 + 1.360 \times 10^{-3} T\,. \quad (1.10)$$

An ideal crystal growth using the Bridgman method is based on solidification of the melt with a stoichiometric composition using starting materials as pure as possible (6N-7N). During the solidification, the system state proceeds through the congruent melting point (labeled by temperature 1092°C in the *T-x* diagram in Fig.1.10 and by the point CMP in the *P-T* diagram in Fig.1.11), where the melt and occurring solid state have the same composition. As the melt is solidified, the system state should follow the solidus line in the *T-x* diagram and simultaneously the stoichiometric line in the *P-T* diagram by control of the crystal temperature and P_{Cd} of the system. As can be seen in Fig.1.11 the CMP is slightly shifted to the composition with tellurium enrichment and after the solidification of the melt is necessary to shift the system state toward the stoichiometric line. After cooling of the crystal to room temperature a material with stoichiometric composition should be obtained. However, described situation represents only an ideal case of solidification. During the real crystal growth various deviations from the presented situation can occur.

Finally, it is necessary to note that described solidification process is very similar also for the crystal growth of $Cd_{0.96}Zn_{0.04}Te$ and $Cd_{0.9}Zn_{0.1}Te$. It is expected that in case of such small concentration of Zn in CdTe the *T-x* and *P-T* diagrams as well as equations (1.9) and (1.10) differ from there for CdTe only slightly.

1.5. Point defects

1.5.1. Native point defects

In an ideal crystal all atoms form an ideal crystalline lattice. However, this situation is theoretically possible only at $T = 0K$. At nonzero temperature, deviations from the ideal distribution of atoms occur and native defects are formed. In a binary compound *AB* cation and anion vacancies V_A , V_B, interstitials A_i, B_i, antisite defects B_A, A_B, and complex defects like vacancy-antisite complex B_AV_A can be created (see Fig.1.12).

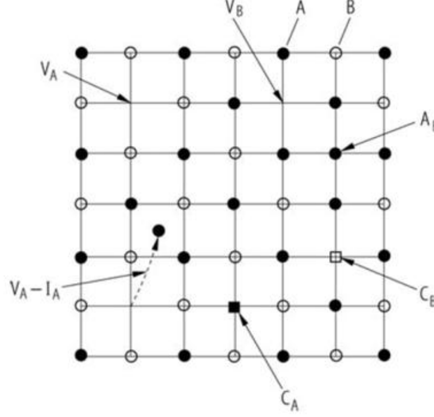

Fig.1.12: Types of defects in a crystal lattice [33]. The notation in this picture represents A, B – crystal atoms, V – vacancy, I – interstitial, C – impurity atom.

Properties of native point defects are well described by considering the equilibrium between a non-stoichiometric solid phase and some external phase defined by the activities of the material components [23]. An analysis of such an equilibrium leads to knowledge about the two fundamental quantities characterizing point defects: (i) the formation energy and (ii) the spectrum of energy levels in the semiconductor gap. In the following the principles and the main relations describing defect equilibrium within the quasi-chemical formalism are derived.

First the case of vacancy of the atom *A* in II-VI compound *AB* is considered. Anion vacancies (V_A) are supposed to introduce two acceptor ionization energy levels in the bandgap. These levels are labeled by E_{A_1} and E_{A_2}, corresponding to the first and the second ionization state respectively ($E_{A_2} > E_{A_1}$). Equilibrium with an external phase containing *A* in the vapor (A_g) is written as:

$$AB \Leftrightarrow V_A B + A_g \qquad (1.11)$$

Mass-action law leads to

$$\left[V_A^0\right] = K_{V_A^0} / P_A \qquad (1.12)$$

where the concentration of neutral V_A is related to the reaction constant $K_{V_A^0}$ and to the partial pressure P_A of *A* in the vapor phase. The reaction constant can be expressed in terms of the formation energy parameters: enthalpy $H_{V_A^0}$ and entropy $S_{V_A^0}$

$$K_{V_A^0} = (k_B T)^{5/2} (2\pi m_A)^{3/2} h^{-3} \exp\left(-\frac{H_{V_A^0}}{k_B T}\right) \exp\left(\frac{S_{V_A^0}}{k_B}\right) \qquad (1.13)$$

where m_A is the mass of A, h is the Planck's constant and k_B in the Boltzmann's constant. The last expression holds when concentrations are expressed in site fractions and pressure in atmospheres. The formation enthalpy H is more readily accessible to experiments and theory and is often quoted as the formation energy itself. The concentrations of singly and doubly ionized vacancies $\left[V_A^-\right]$ and $\left[V_A^{2-}\right]$ respectively, are given by the ionization relations

$$\left[V_A^-\right] = \left(g_{V_A^-} / g_{V_A^0}\right)\exp\left(\frac{E_F - E_{A_1}}{kT}\right)\left[V_A^0\right] \tag{1.14}$$

$$\left[V_A^{2-}\right] = \left(g_{V_A^{2-}} / g_{V_A^-}\right)\exp\left(\frac{E_F - E_{A_2}}{kT}\right)\left[V_A^-\right] \tag{1.15}$$

where the g-s are degeneracy factors relative to the labeled ionization states. E_F is the Fermi level energy, the position of which depends on the electronic equilibrium in the solid, formulated by the electrical neutrality condition

$$n + \left[V_A^-\right] + 2\left[V_A^{2-}\right] + N_A^- = p + N_D^+ \tag{1.16}$$

where n and p are the free electron and hole concentrations, N_A^- and N_D^+ are concentrations of any foreign ionized donor and acceptor impurities, respectively. Similar formalism can be also applied to other types of defects like A interstitial (A_i)

$$A_g \Leftrightarrow A_i \tag{1.17}$$

$$\left[A_i^0\right] = K_{A_i^0} P_A \tag{1.18}$$

or antisite B_A

$$2AB \Leftrightarrow B_A B + 2A_g \tag{1.19}$$

$$\left[B_A^0\right] = K_{B_A^0} / P_A^2 \, . \tag{1.20}$$

Calculated formation energies of particular neutral native point defects in CdTe are listed in Tab.1.1 [24]. There are two interstitial sites in the zinc-blende structure. One site is surrounded by anions (a) and the other one by cations (c). For neutral Cd_i the lowest possible formation energy is $\Delta H(Cd_i^0)$=2.04eV. Cadmium antisite defect Cd_{Te} hasn't been observed experimentally and is only predicted from numerical calculations [24].

Energy levels of the most frequent native point defects are presented in Fig.1.13. These levels correspond to electrically active ionized native defects, which have been observed using various experimental methods (PICTS, DLTS, TEES, PL, Hall effect measurements..) [10]. Dominant donor-like native defects in Cd-rich crystals are singly ionized Cd_i^+, doubly ionized Cd_i^{2+} and doubly ionized Te_{Cd}^{2+}. The main acceptor-like native defects are monovalent and divalent

Tab.1.1: Formation energies of native point defects in CdTe at neutral charged state [24].

defect	*Formation energy ΔH in CdTe (eV)*	*defect*	*Formation energy ΔH in CdTe (eV)*
V_{Cd}	1.88	V_{Te}	2.45
Te_i	2.62	Te_{Cd}	2.91
Cd_i^a	1.47	Cd_{Te}	3.13
Cd_i^c	1.25		

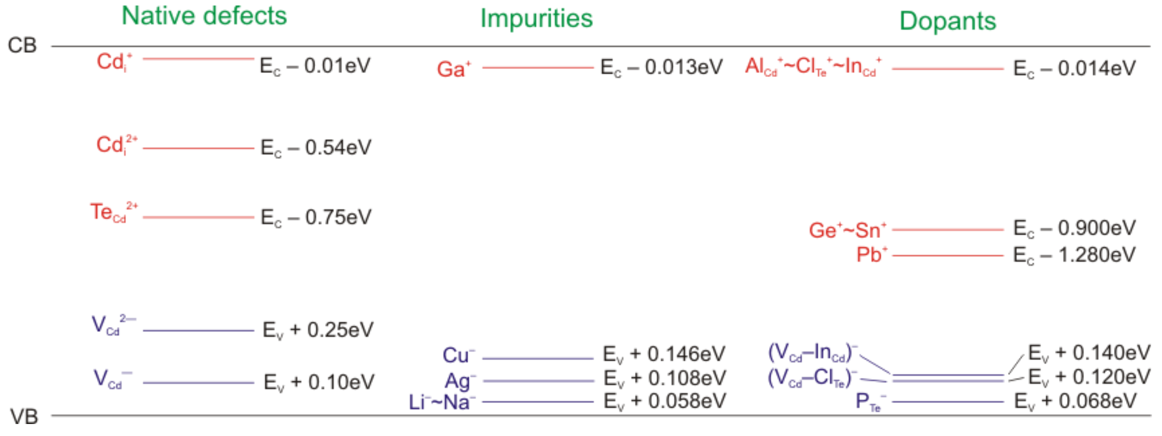

Fig.1.13: Scheme of energy levels of the most common native defects, impurities and dopants in CdTe [10,25,26]. Red lines represent donor levels, blue lines denote acceptor levels.

V_{Cd}^{-} and V_{Cd}^{2-}, respectively. In contrast to V_{Cd}^{-}, which energy level is intended more or less precisely, the energy level of V_{Cd}^{2-} varies from 0.2 to 0.45 eV depending on the used measurement technique [10].

1.5.2. Extrinsic point defects

Since it is not possible to prepare absolutely pure CdTe crystals, the extrinsic defects play important role in the point defect structure of CdTe. Extrinsic defects can be divided into (i) impurities uncontrollable present in crystals and (ii) dopants specially introduced into the crystal to modify the physical and chemical properties of the material (see Fig.1.13). The main aim is to prepare material with impurity concentrations as low as possible to attenuate their influence on the crystal properties. The concentration level of impurities should be lower than the concentration of the native point defects, which is about $10^{15}cm^{-3}$ at room temperature. This goal is successfully reached by combination of purification methods (i) repeated vacuum distillation and (ii) zone refining. Such methods result in impurity content at the level about 10^{15}-$10^{16}cm^{-3}$. Typical uncontrollable impurities are Cu, Li, Na, Ag, K and O. The formation energies of neutral and ionized impurity-related point defects are listed in ref. [24] and their energy levels are plotted in Fig.1.13. Contrary to impurities, dopants are atoms which are intentionally introduced to the material resulting in changing of its physical properties. The most important ones are indium and chlorine dopants. Both behave as shallow donors and together with a cadmium vacancy create also an acceptor-like complex defect called "*A-center*". In case of indium doping, indium atoms are embedded in the cadmium sublattice and form a shallow donor with the ionization energy $E_i^{In} = 14.15meV$. Interaction of In_{Cd}^{+} with a divalent cadmium vacancy V_{Cd}^{2-} on the closest available site form an additional monovalent acceptor-like A-center $\left(V_{Cd} - In_{Cd}\right)^{-}$. The binding energy of the indium A-center is 140meV. Contrary to indium, chlorine doping atoms are incorporated in the tellurium sublattice and form more stable donor-like defects with the ionization energy $E_i^{Cl} = 14.48meV$. The chlorine A-center consisting of V_{Cd}^{2-} and Cl_{Te}^{+} exhibits the binding energy of about 120meV.

1.5.3. Compensation of CdTe

Many of point defects present in the crystal are electrically active. Impurity compensation refers to the fact, that the doping efficiency is reduced by the presence of oppositely charged point

defects or complexes [10]. It is common to distinguish between different cases, depending on the compensation degree. In well-defined n-type (or p-type) material, increasing of the doping level is compensated by formation of oppositely charged native defects. However, strong compensation of charged defects doesn't occur. In strongly compensated (semi-insulating) case, the compensation is based on precise compensation of shallow charged defects and presence of one deep level responsible for the pinning of the Fermi level in the midgap position.

Self-compensation

If we consider well defined n-type material doped by *In* with concentration [*In*], compensation is then attributed to two main native acceptor defects: doubly ionized acceptor V_{Cd} and singly ionized indium A-center (V_{Cd}-In_{Cd}). Electrical neutrality and mass conservation are expressed by:

$$n = \left[In_{Cd}^{+}\right] - \left[V_{Cd}^{-}\right] - 2\left[V_{Cd}^{2-}\right] - \left[\left(V_{Cd}^{2-} - In_{Cd}^{+}\right)^{-}\right] \tag{1.21}$$

$$\left[In\right] = \left[In_{Cd}^{+}\right] + \left[\left(V_{Cd}^{2-} - In_{Cd}^{+}\right)^{-}\right] \tag{1.22}$$

where n is the free electron concentration. Equation (1.22) implies that the indium donor and the acceptor complex are fully ionized in n-type CdTe at the doping temperature. Ionization of V_{Cd} is described by the relations (omitting the degeneracy factors):

$$\left[V_{Cd}^{-}\right] = \left[V_{Cd}^{0}\right] \exp\left(\frac{E_F - E_1}{k_B T}\right) \tag{1.23}$$

$$\left[V_{Cd}^{2-}\right] = \left[V_{Cd}^{0}\right] \exp\left(\frac{2E_F - E_1 - E_2}{k_B T}\right) \tag{1.24}$$

where T is the temperature. E_1 and E_2 represent the first and second ionization levels of the vacancy in the band gap, respectively. V_{Cd}^{0} designates the neutral cadmium vacancy the concentration of which is directly linked to the Cd chemical potential in the external phase (in case of a gaseous phase given by the partial pressure P_{Cd}). One clearly sees from (1.23) and (1.24) that the concentrations of negatively charged vacancies increase for increasing of the Fermi level due to enhancing of $[In_{Cd}^{+}]$. This situation represents the *self-compensation* effect in well-defined n-type material.

Similar description can be written for well-defined p-type material. In this case, Cu_{Cd} or P_{Te} are used as a doping material. Compensating native point defects to be considered are doubly ionized donors Cd_i^{2+} and V_{Te}^{2+}.

Semi-insulating state

Strong compensation of point defects can lead to a semi-insulating (SI) state. It makes possible such important applications as optical modulators and radiation detectors [10]. Preparation of semi-insulating CdTe only by balanced concentration of shallow donors and acceptors is practically impossible. Beside similar concentration of dominant shallow donors and acceptors also a deep donor/acceptor level is necessary to fix the position of the Fermi level in the midgap. For n-type high-resistive material a strong compensation occurs when:

$$N_D < N_A < \left(N_D + N_{DD}\right) \tag{1.25}$$

where N_D represents the concentration of shallow donors, N_{DD} deep donor level and N_A shallow acceptors. In this situation the Fermi energy drops from a position close to the shallow

impurity/doping level to pin at the deep level. Analogical equation can be written for strong compensation of a p-type material.

The situation with preparation of semi-insulating CdTe is quite complicated. The concentration of residual acceptor impurities (Cu_{Cd}, Li_{Cd}, Na_{Cd}…) in undoped CdTe is at level ~10^{15}cm^{-3}. Moreover, also the concentration of V_{Cd} in the crystal grown under Te-rich conditions is at the same level. Therefore, undoped CdTe crystals are usually low-resistive p-types with p~10^{15}-10^{16}cm^{-3}. For the compensation of shallow acceptors, CdTe is intentionally doped by In, Cl or Al in the concentration range from 10^{16}cm^{-3} to few 10^{17}cm^{-3}, which must be higher than the total concentration of shallow acceptors. Doping leads to formation of shallow singly ionized donor states In_{Cd}^{+}, Cl_{Te}^{+} or Al_{Cd}^{+} and simultaneously to formation of acceptor complexes created by singly ionized shallow doping donor and V_{Cd}^{2-}. Consequently the concentration of all electrically active shallow donors and shallow acceptors is close to each other. For pinning of the Fermi energy close to midgap a deep midgap level is necessary. The deep level can be incorporated intentionally to the material by Ge or Sn doping. These elements form deep levels at concentrations of about 10^{15}cm^{-3}. However, such a concentrations of deep levels degrade the operation of X-ray and γ-ray CdTe detectors. Optimal deep level concentration was found to be lower than 10^{11}cm^{-3}. This concentration can be reached without doping of the material by deep impurities. In CdTe crystal always one or more deep levels with such a concentration are present. However, the origin of these levels is still not completely clear. In few works one of them is attributed to the native defect Te_{Cd}. Finally, strong compensated CdTe exhibits resistivity higher than 10^{8}Ωcm. Nevertheless, the reproducibility of production of SI CdTe crystals is not high. Hence, one of the main goals of the research in presence is to find reproducible methods of preparation of SI CdTe either by an improvement of crystal growing techniques or by application of post-growth annealing steps.

1.5.4. Segregation of extrinsic defects

The distribution of extrinsic defects (impurities, dopants) along the ingot (especially if the Bridgman method or the VGF method is used) is not constant, however, is determined by the segregation coefficient k_d (see the equation (1.7)) of certain impurity/dopant in CdTe given by the Scheil-Gulliver expression [18]:

$$C_S(z) = k_d C_0 (1-z)^{k_d - 1} \tag{1.26}$$

where C_0 is the initial concentration of extrinsic defect in the charge and z represents the fractional distance from the first to freeze part of the ingot. The segregation coefficient k_d is defined as the ratio of the mole fraction of the extrinsic defect in the crystal to that in the liquid. Segregation coefficients of most common impurities/dopants in CdTe are listed in Table 1.2.

Tab.1.2: Segregation coefficients of most common extrinsic defects in CdTe [18].

extrinsic defect	*Segregation coefficient*	*extrinsic defect*	*Segregation coefficient*
Zn	4	In	~0.1
Li	0.3	Cl	0.005
Na	0.02	Al	0.1
Cu	0.2	Ag	0.009

1.6. Line defects

During solidification of the melt an ideal crystal without structural defects should be created. However, crystals are usually grown in a crucible, what leads to formation of an additional stress in the solidified material. This stress is relaxed by formation of line discontinuities in the crystal lattice – *dislocations*. Generally, dislocations are formed randomly within the whole crystal grain. A systematic research of dislocations in CdTe induced by a mechanical stress was performed by Schreiber et al. [27]. After application of well defined stress on the CdTe surface, dislocation loops in preferential crystallographic directions were formed (Fig.1.14). Induced dislocations formed star-shaped rosettes in <110> directions with the size tens of micrometers. The concentration of dislocations can be evaluated by etch-pits density measurements, during which dislocations perpendicular to the surface are revealed on surface by etching of the material using specialized etchants [28]. Their typical density in CdTe is at level about 10^4-10^5cm^{-3}.

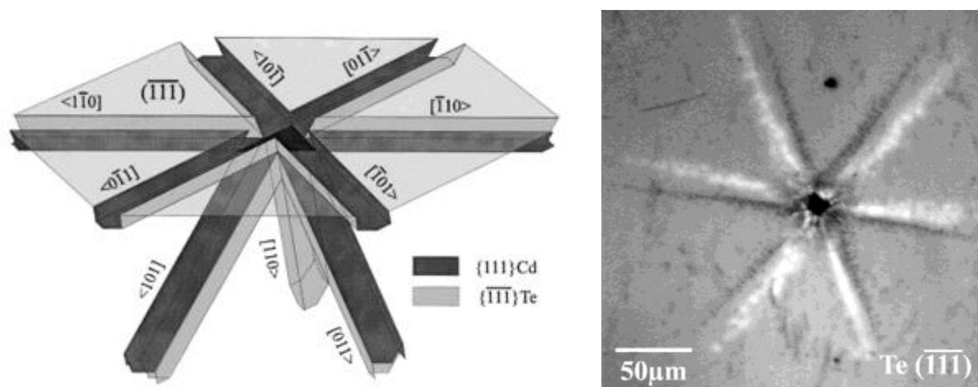

Fig.1.14: Theoretical description and experimental investigation of dislocations on (111) Te-oriented CdTe surface. Mechanically induced tension is relaxed by formation of dislocations in <110> directions [27].

1.7. Plane defects

Solidification of the melt should proceed under very stable conditions in a crucible with as pure as possible walls. However, residual impurity clusters present on the crucible walls, crucible asperity or vibrations behave as nucleation centers. These effects cause a formation of higher number of smaller crystal grains, what results in a polycrystalline material formed by small grains with slightly different crystallographic orientations. Planes between individual grains are *grain boundaries*, which often significantly affect the electrical and thermal properties of materials and also play role as nucleation centers for precipitation of new phases from the solid. CdTe crystals prepared by the Bridgman method (or by its modifications) are generally polycrystalline. Nevertheless, the size of grown grains is usually sufficient (about few centimeters in diameter) for preparation of monocrystalic pieces used as substrates for IR radiation detectors or as X-ray and γ-ray detectors.

Very often a specific grain boundary – *twin boundary* – can be found in CdTe crystals. Crystal twinning occurs when two separate crystals share some of the same crystal lattice points in a symmetrical manner. The origin of twin boundaries in CdTe is not completely clear until these days.

1.8. Second phase defects

An ideal process of CdTe crystallization was described in chapter 1.4.4. However, real crystal growth is much more complicated at least due to the complex shape of the solidus line plotted in Fig.1.10, which is in detail shown in Fig.1.15. During the crystal growth and following cooling process down to the room temperature two types of second phase defects can be created [18,29,30]: a) inclusions – defects with size up to tens of micrometers formed during solidification of the melt and b) precipitates – new second phases with size up to tens of nanometers created during cooling of the crystal.

1.8.1. Inclusions

During solidification of the melt, composition deviations from the thermodynamic equilibrium can occur. Solidification of the melt in local places of the crystallization interface doesn't proceeds through the CMP and two different phases - solid and melt with nonstoichiometry composition – are formed. The process of real crystallization is depicted in Fig.1.15 by the blue line. In the region marked by the red arrow the system passes through the two phase region, where thermal fluctuations on the crystallization interface lead to creation of Te-rich droplets. This effect can be emphasized by the effect of a constitutional supercooling, which occurs in front of the crystallization interface, where an accumulation of excess tellurium appears (see also the chapter 1.4.2.). The solution at the solid-liquid interface is depleted of Cd and becomes more tellurium-rich. As a consequence, the liquidus temperature at the interface is lower than that of the rest melt. This encourages a dendritic growth through undepleted regions and subsequent entrapment of Te-rich droplets. With decreasing temperature, CdTe from Te-rich droplets crystallizes leading to reduction of their size and after their solidification *inclusions* are formed.

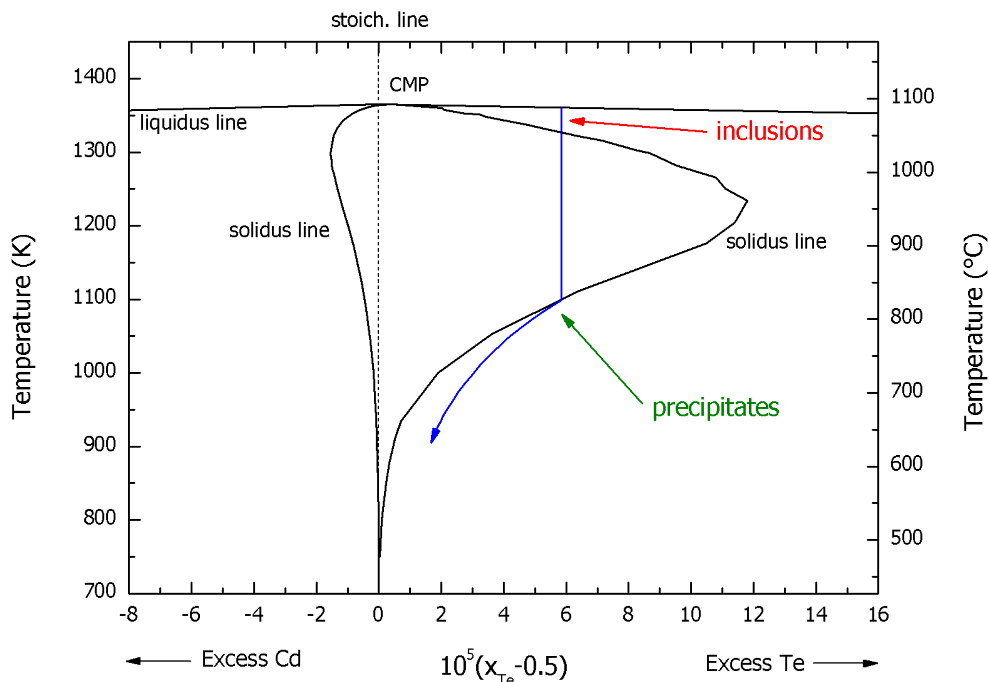

Fig.1.15: Detail of the stability region of CdTe defined by the solidus lines (based on [21]).

1.8.2. Precipitates

Cooling of the crystal continues along the blue line between the solidus lines. The excess of tellurium in the crystal is smaller than the maximal solubility limit given by the solidus line. With decreasing temperature, the solubility limit starts to be retrograde. At certain temperature the Te excess reaches the solubility limit (break of the blue line) and with further cooling of the crystal the tellurium excess starts to diffuse out from the material (blue arrow). However, the diffusion rate of Te also decreases with decreasing temperature. Hence, at certain temperature the tellurium excess remains in the crystal lattice and starts to nucleate resulting in formation of a second phase – *precipitates*.

Precipitates can be created in the solid randomly in the whole volume (*homogeneous* precipitation) or in energetically favorable places (*heterogeneous* precipitation) [16]. Formation of precipitates can be described using basic thermodynamic quantities. First we will consider a *homogeneous* precipitation. The surface energy E_σ of a new interface between the initial and originating new phase is the energy reacting against the formation of new a precipitate. The formation of precipitate is energetically favorable when the "volume" energy (free enthalpy) of a new phase is lower than energy of an initial state. δG represents a change of the Gibbs potential connected with a precipitate formation; and can be written as a sum of δG_g describing the difference of free enthalpy of an initial phase g_1 and an originating phase g_2, and δG_σ connected with a formation of the phase interface. Assuming that $\delta G \cong \delta F$ we can write:

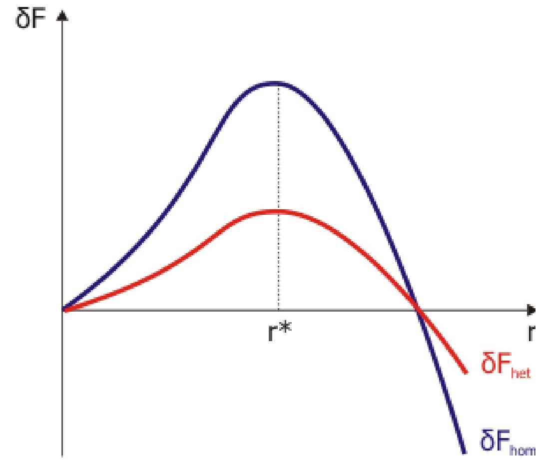

Fig.1.16: Dependence of the free energy on the size of an occurring precipitate.

$$\delta F = \delta F_g + \delta F_\sigma \tag{1.27}$$

$$\delta F_\sigma = E_\sigma S_p \tag{1.28}$$

$$\delta F_g = V_p (f_2 - f_1) \tag{1.29}$$

where V_p and S_p is volume and surface of occurring precipitate; f_1 and f_2 is free energies of phase 1 and 2 per volume unit, respectively. Assuming that precipitates occur homogeneously, have a spherical shape and the surface energy is positive $E_\sigma > 0$, we can write:

$$\delta F = \frac{4}{3}\pi r^3 (f_2 - f_1) + 4\pi r^2 E_\sigma \tag{1.30}$$

where we suppose that f_1, f_2 and E_σ are independent on r. Precipitate formation occurs only at such temperature, where $f_2 < f_1$. We define temperature T_C at which $f_2 = f_1$ and supercooling Θ by the relation $\Theta = T_C - T$. Assuming that $\Theta > 0$ together with $f_2(T) < f_1(T)$. From the equation (1.30) leads the dependence $\delta F = \delta F(r)$ plotted as the blue line in Fig.1.16. The condition for an extreme $\left(\frac{\partial F}{\partial r}\right)_{r^*} = 0$ gives:

$$r^* = \frac{2E_\sigma}{(f_1 - f_2)} > 0 \tag{1.31}$$

Above the value r^* the new precipitate is stable and starts to increase its volume. With increasing supercooling Θ the size of precipitates decreasing and their amount is increasing. The final size and space distribution of precipitates is given not only by the shape of the phase diagram but also by the cooling rate of the crystal and by the type and distribution of lattice defects.

If lattice defects (e.g. dislocations, grain boundaries) are present in the crystal, precipitation can preferentially occur on these defects. For such a *heterogeneous* precipitation can be written:

$$\delta F_{het} = S(\vartheta)\delta F_{\hom} \tag{1.32}$$

where $S(\vartheta)$ is the shape factor depending on the lattice defect properties and is usually much smaller than 1. From the Fig.1.16 can be seen that the heterogeneous precipitation occurs easier comparing to uniformly distributed homogeneous precipitation.

1.9. Chemical diffusion

The crystal lattice of CdTe consists of the cadmium and tellurium sublattice. Most of native (Cd_i, V_{Cd}) and extrinsic (In_{Cd}, Al_{Cd}, Cu_{Cd}, Na_{Cd}, Li_{Cd}..) point defects are incorporated in the cadmium sublattice and also most of diffusion processes proceed within it. The chemical diffusion changes the point defect distribution in the crystal lattice. Its rate is negligible for CdTe at room temperature and starts to be significant at temperatures above 500°C. In CdTe, three diffusion processes are present: interstitial, vacancy and antisite diffusion mechanism. It is expected that the chemical diffusion coefficient doesn't depend on whether the diffusion proceeds in the Te subulattice or within the Cd sublattice [31]. The concentration of native point defects can be intentionally modulated by post-growth annealing of the material in a Cd-rich or Te-rich atmosphere at temperatures higher than 500°C.

As an example, basic parameters of the chemical diffusion in Te-rich CdTe:Cl will be described in this paragraph based on [32]. Given concentration $[X^q]$ of defect X with a charge q, the one-dimensional flux of X^q with the diffusion coefficient D_X^q is expressed by:

$$J_X^q = -D_X^q \frac{\partial [X^q]}{\partial z} + \langle v_X^q \rangle [X^q]. \tag{1.33}$$

The average velocity $\langle v_X^q \rangle$ is specified by an internal electric field induced by the charged defect distribution. Using the Nerst-Einstein relation and basic charge defects statistics, J_X^q can be simplified to the form

$$J_X^q = -D_X^q \frac{[X^q]}{[X^0]} \frac{\partial [X^0]}{\partial z}. \tag{1.34}$$

The flux of the stoichiometry deviation Δ is equal to

$$J_\Delta = \sum_{X,q} \frac{\partial \Delta}{\partial [X^0]} J_X^q \tag{1.35}$$

where

$$\Delta = [Cd] - [Te] = [Cd_I^0] + [Cd_I^+] + [Cd_I^{2+}] - [V_{Cd}^0] - [V_{Cd}^-] - [V_{Cd}^{2-}] + [B^0] + [B^+] \tag{1.36}$$

where B represents donor doping atoms. A-center does not appear in Δ explicitly because it represents both one Cd and one Te atoms missing in the lattice. The diffusion of a dopant B is not assumed. After involving local defect equilibrium and quasi-neutral approximation and after combining equations (1.34) and (1.35), the chemical diffusion coefficient $\tilde{D}$ is expressed in the form

$$\tilde{D} = -\frac{J_\Delta}{\partial\Delta / \partial z} = \sum_{X,q} D_X^q \frac{[X^q]}{[X^0]} \left| \frac{d[X^0]}{d\Delta} \right|. \quad (1.37)$$

Consequently, all defects densities as well as μ_F may be expressed by means of Cd chemical potential, or Δ, or P_{Cd} alternatively. For example, in CdTe:Cl with V_{Cd}^{2-} as dominant diffusing entity, $\tilde{D}$ is well approximated with

$$\tilde{D} = \frac{D(V_{Cd}^{2-})[V_{Cd}^{2-}]}{P_{Cd} \frac{d([V_{Cd}^{2-}] - [Cl_{Te}^{+}] + n)}{dP_{Cd}}}. \quad (1.38)$$

1.10. Transport properties

The electrical current density is determined by the concentration and charge of mobile carriers and by their average velocity [33]. In semiconductors the former can be tuned in a wide range by doping and by changing the temperature, while the latter depends on the driving force and on the scattering processes with crystal imperfections. The driving force can be an electrical field as well as a temperature gradient or an inhomogeneity in the doping (gradient of the chemical potential). A simultaneously applied magnetic field can be used to provide additional relevant information on the carrier concentration and mobility. The different scattering processes of free carriers exhibit characteristic temperature dependencies.

Free carriers

The single particle states in the band structure and the impurity states are occupied by electrons according to the Fermi-Dirac distribution function

$$f_0(E,T) = \frac{1}{\exp\left[\frac{E(k) - \mu_{chem}}{k_B T}\right] + 1} \quad (1.39)$$

with the chemical potential μ_{chem}. It depends on the temperature and is identified at T=0 with the Fermi energy E_F. In the intrinsic case (no crystal defects) at T=0 all valence band states are occupied and all conduction states are empty, thus the Fermi energy is positioned in the bandgap. For the intrinsic electron and hole concentration can be written:

$$n_i(T) = \int g_c(E) f_0(E,T) dE \quad (1.40)$$

$$p_i(T) = \int g_v(E)(1 - f_0(E,T)) dE \quad (1.41)$$

with the density of states *g(E)* for the conduction and valence band, respectively. Assuming isotropic parabolic energy bands and the neutrality condition $n_i(T) = p_i(T)$ leads to the chemical potential

$$\mu_{chem}^i(T) = \frac{E_c + E_v}{2} + \frac{3}{4} k_B T \ln \frac{m_v^*}{m_c^*} \quad (1.42)$$

for the intrinsic case. Hence, the intrinsic Fermi energy $E_{F,i} = \mu_{chem}^i(T=0)$ is in the middle of the bandgap and is shifted towards the band edge with the smaller effective mass. The neutrality condition leads to the intrinsic carrier concentration

$$n_i p_i = n_i^2. \quad (1.43)$$

In extrinsic semiconductors with donor and acceptor concentration N_D and N_A, the electrical neutrality condition $p + N_D^+ = n + N_A^-$ leads to the chemical potential

$$\mu_{chem}(T) = \mu_{chem}^i(T) + \frac{k_B T}{2} \ln \frac{n}{p} \ . \qquad (1.44)$$

Hence, doping leads to an additional temperature dependent shift of the chemical potential away from the midgap. For predominantly *n* or *p* doped semiconductors the chemical potential μ_{chem} will be close to the impurity level (shallow or deep).

Scattering of free carriers

The mobility μ of dominant free carriers in the material is affected by the temperature dependent scattering mechanism. At low temperature a scattering on ionized impurities dominates and $\mu \approx T^{3/2}$. At higher temperature a scattering on polar optical phonons is dominant in CdTe and $\mu \approx T^{-1/2}$.

1.11. Optical properties

1.11.1. Photoluminescence

Recombination processes in semiconductors can be radiative, represented for example by photoluminescence (PL) emission spectra and non-radiative with only indirect influence on optical properties. PL spectra of CdTe exhibit usually few types of radiative transition like free and bound excitons, donor-acceptor-pairs, A-centers and deep levels [33,34]. Basic properties of every transition will be briefly described.

Excitons

Energy of an electron-hole pair created by photon excitation can be lowered by their mutual electron-hole Coulomb interaction. This situation can be described within the hydrogen model. If we consider the total mass $M_{ex} = m_e + m_h$ and the reduced mass $\mu_{ex} = \frac{m_e m_h}{(m_e + m_h)}$ of the electron-hole pair as exciton mass parameters, the characteristic energy and length of the system are given by the effective Rydberg constant of the exciton $R_{eff} = \mu_{ex} / \varepsilon^2 R_{Rydberg}$ and the effective Bohr radius $a_{B,eff} = m_0 \varepsilon / \mu_{ex} a_B$, where ε is the dielectric constant of the semiconductor and $R_{Rydberg}$ and a_B are the Rydberg constant and the Bohr radius of the hydrogen atom, respectively. With μ_{ex} being of order of $0.1m_0$ and $\varepsilon_{CdTe} \cong 10$ for CdTe one finds R_{eff} in the order of a few meV (comparing to gap energies in the order of eV) and $a_{B,eff}$ in the order of 100Å (comparing to lattice constants of a few Å). Thus, excitons usually create additional shallow levels near the conduction or valence band.

Free and bound excitons

Electron-hole pair interacting via Coulomb interaction described in the previous section is called a *free exciton* (FE). There exists also another type of excitons, which is bounded to shallow

point defect present in the crystal lattice – *bound exciton*. Depending on the nature of the point defect, bound excitons are classified as

(D^0,X) – exciton bound to neutral donor (in CdTe usually about 4meV)

(A^0,X) – exciton bound to neutral acceptor (in CdTe usually 6-16meV).

Shallow and deep impurities

An impurity, weakly localized in the crystal lattice, interacts with neighbor atoms by a long-range Coulomb interaction described by the effective-mass approximation. Such an impurity behaves as a *shallow impurity* forming an energy level close to the conductive or valence band. On the other hand, an impurity strongly localized in the unit cell around the impurity and described by the central cell correction theory behaves like a *deep impurity* with energy level situated close to the midgap.

Specific complex defect is a *donor-acceptor pair*, which corresponds to transition of an electron between the donor and acceptor state. Its energy is described by the relation

$$E_{DAP} = E_g - E_A - E_D + \frac{e^2}{4\pi\varepsilon r_{DA}} \tag{1.45}$$

where r_{DA} is the distance between donor and acceptor in the crystal lattice.

A-center

In CdTe, the complex of acceptor $\left(V_{Cd}^{2-}\right)$ together with shallow donor impurity $\left(In_{Cd}^{+}, Cl_{Te}^{+}, Al_{Cd}^{+}, Cu_{Cd}^{+}\right)$ form an acceptor-like complex called an *A-center* (e.g. $\left(V_{Cd}^{2-} - In_{Cd}^{+}\right)^{-}$). Moreover, the electron-phonon interaction in II-VI semiconductors is very strong and is manifested by strong intensity of so-called longitudinal optical (LO) phonon replicas. The strength of such a electron-phonon interaction is described by the Huang-Rhys factor S (in CdTe $S \approx 3$-4). In CdTe, the individual phonons replicas are separated by energy of about 21meV.

1.11.2. Infrared transmittance

General formula for the infrared transmittance (***T***) is

$$\boldsymbol{T} = \frac{(1-R)^2 e^{-\alpha d}}{1 - R^2 e^{-2\alpha d}} \tag{1.46}$$

where R is the reflectivity of the sample surface, α is the absorption coefficient and d is the thickness of the sample. In the investigated band-gap range of the intrinsic CdTe-related crystals the imaginary part of the complex refraction index is small compared to the real part, therefore we can write for R:

$$R = \frac{(n-1)^2}{(n+1)^2} \tag{1.47}$$

Solving quadratic equation (1.46) for $\exp(-\alpha d)$, the absorption coefficient is calculated from:

$$\alpha = \frac{1}{d} \ln \frac{(1-R)^2 + \sqrt{(1-R)^4 + 4\boldsymbol{T}_{\max}^2 R^2}}{2\boldsymbol{T}} \tag{1.48}$$

where $\boldsymbol{T}_{\max}$ is the maximal value of $\boldsymbol{T}$ in every spectrum.

Free carrier absorption

The free carrier absorption of the radiation is well known from metals and heavily-doped semiconductors. In mentioned types of materials, the Fermi energy is situated in (or close to) the valence (or conductive) band and material exhibits a high free carrier concentration. Light with wavelength in the infrared region focused on such type of material is absorbed by free carriers. By this process, the initial energy of holes (electrons) is enhanced and excited carriers start to loss their enhanced energy either by an interaction with phonons or by the Coulomb interaction with ionized impurities.

High concentration of free carriers in CdTe can be obtained by doping of the material by donors (or acceptors) resulting in a heavily conductive crystal. Free carrier absorption (FCA) in CdTe starts to be significant in IR transmittance spectra, when the free carrier concentration exceeds $3\times10^{15}cm^{-3}$. FCA on longitudinal optical phonons dominates in the concentration range of 3×10^{15}- 4×10^{17} cm^{-3}. FCA on ionized impurities modulates spectra in crystals with concentration higher than 4×10^{17} cm^{-3}. Both mentioned absorption mechanisms can be distinguished using the analysis of the absorption coefficient α versus wavelength $\alpha=k\lambda^{m}$, where k is a constant and m is an exponent. For the FCA on phonons m~3. FCA on ionized impurities exhibits m~4 [35].

1.12. Detection of X-ray and γ-ray radiation

High-resistive semiconductors with planar contacts on opposite surfaces can be used as detectors of X-ray and γ-ray radiation [9,36]. Incident high-energetic photons pass through the cathode and crate electron-hole pairs in the material volume through the dominant interaction – the photoelectric effect, Compton scattering or electron-positron pair production.

If case of the photoelectric effect, the whole photon energy is transferred into an excitation of an electron in a deeper atomic shell of one atom in the crystal lattice and the rest energy is transferred into the kinetic energy of the atom. High kinetic energy of the electron is relaxed by further excitation of other electrons. Since the energy of the incident photon is completely transferred to creation of electron-hole pairs, this type of interaction leads to an ideal charge generation. If the charge collection toward electrodes proceeds without any recombination or trapping mechanism, the output signal from the detector is proportional to the energy of the absorbed photon. This leads to a creation of a photopeak in the final energy spectrum. It should be noted that a hole in a deeper atomic shell (created after the first photolelectric event) is filled by an electron from higher shell resulting in an emission of a characteristic X-ray photon. Emitted X-rays can either repeatedly created electron-hole pairs or escape the detector. In the latter case, part of the energy of the incident photon is lost and new escape peak appears in the spectrum at lower energies. Its position is shifted from the photopeak position by the energy of the characteristic radiation.

In case of a Compton interaction, the amount of energy transferred from the photon to an electron in deeper atomic shell depends also on the collision geometry. Reflected photon with lower energy escape the detector and part of the incident photon energy is lost. A generation of electron-hole pairs continues similarly as was described in the previous paragraph. Finally, a Compton continuum appears in the energy spectrum at low energies. If the detector is large, incident photon interacts with a matter via multiple Compton interaction and the whole photon energy is transferred into the electron-hole pair generation. In this case, final spectrum exhibits only one main photopeak at energy corresponding to the energy of the incident photon. Moreover,

similarly as in case of photoelectric event, a peak connected with the characteristic radiation can occur.

If the energy of the incident photon is above 1.022MeV, the photon can annihilate in a matter and create an electron-positron pair. Both created charged particles start to move to opposite directions. Electron start to interact via Compton interactions described in the previous paragraph. Positron starts to interact with electrons and annihilates. This leads to creation of two photons with energy of 511keV, which are emitted to opposite directions. Emitted photons interact with a matter through the photoelectric and consequently Compton interactions. If the detector is large, all energy of the incident photon is transferred into the photopeak in the energy spectrum. If some energy is lost, new peaks can appear at lower energies.

The type of interaction depends on the energy of incident photons (Fig.1.17). X-ray radiation (120eV– 120keV) interacts mainly via photoelectric and Compton interaction, partly also via elastic Rayleigh scattering (doesn't deposit any energy in the detector). On the other hand, absorption of gamma-ray radiation (120keV – 10MeV) proceeds usually through the Compton interaction or by generation of electron-positron pairs. The efficiency of interaction depends on the atomic number Z of the matter:

Photoelectric effect ~ Z^4-Z^5

Compton scattering ~ Z

Electron-positron pair creation ~ Z^2

As can be seen, the efficiency of interaction strongly depends on the atomic number Z. Due to high average atomic number (Z_{Cd}=48 and Z_{Te}=52), CdTe exhibits higher interaction efficiency comparing to other semiconducting detectors (Z_{Si}=14, Z_{Ge}=32). Moreover, CdTe has wider bandgap (~1.5eV) comparing to Si (1.11eV) or Ge (0.66eV), what enables an operation of CdTe-based detectors even at room temperature without necessity of cooling. If we consider detection of X-ray radiation, high-energetic electrons created in the photoelectric or Compton event lose their energy through repeated electron-hole ionization. Due to the high cross section of this process, the electron-hole pairs form a highly localized charge cloud (with size up to few microns). The charge cloud of electrons and holes is separated in the electric field (applied between the electrodes using an external bias) and the electrons and holes move toward the opposite electrodes, creating a

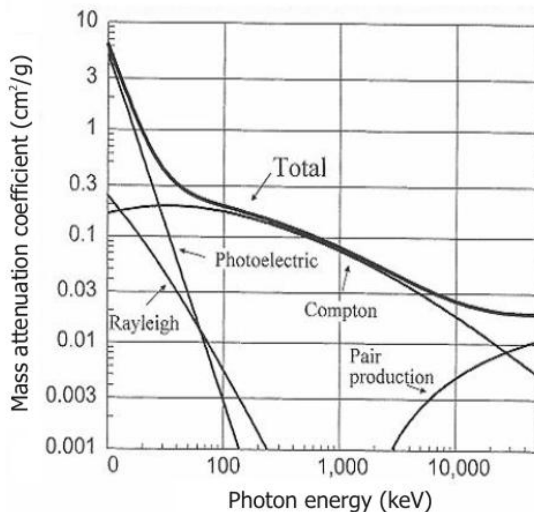

Fig.1.17: High-energetic photons interact with the matter by various mechanisms depending on their photon energy (from [36]).

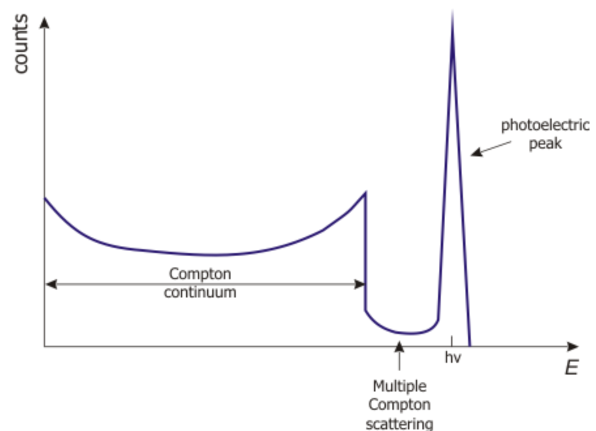

Fig.1.18: Typical pulse height spectrum (based on [36]). The position and shape of the "photopeak" is important for spectroscopic applications.

temporary current through the device. The transport of charged cloud can be described by solving of the drift-diffusion equation (concerning moving and simultaneous spreading of the charged cloud) resulting in an output current pulse [37]:

$$J_{pulse} = e(\mu_n n + \mu_p p)E(x) - e(\mu_n n_0 + \mu_p p_0)E(x) = eE(x)(\mu_n \Delta n + \mu_p \Delta p) \quad (1.49)$$

where $\mu_{n(p)}$ is the electron (hole) drift mobility; $n(p)_0$ is the electron (hole) concentration before excitation; $n(p)$ is the electron (hole) concentration after absorption of a X-ray photon and $E(x)$ is the electric field across the detector. Output signal is amplified by a charge-sensitive pre-amplifier and shaping amplifier and recorded by the multichannel analyzer. Typical final X-ray detection spectrum is showed in Fig.1.18. The main parameter characterizing the quality of the detector is the mobility-lifetime ($\mu\tau$) product of charged carriers. $\mu\tau$ is given by the mobility of electrons μ_e (or holes μ_h) and by lifetime of excited electrons τ_e (τ_h for holes) before their recombination with holes (electrons) or trapping on trapping centers. Moreover, the value of $\mu\tau$ depends also on the illumination intensity.

The shape of final X-ray spectrum (especially the shape of the photopeak) can be strongly affected by various mechanisms present in the detector material:

a) Homogeneous electric field distribution in the detector can be distorted by nonohmic electrodes forming Schottky contacts. This leads to creation of space charge effect (polarization) and consequently to degradation of detection ability of the material.
b) Deep levels, which act as recombination or trapping centers, significantly decrease the lifetime of electrons (holes) resulting in low-energy widening of the photopeak.
c) Second phase defects larger than 3μm play role as trapping centers for electrons and decrease the charge collection efficiency. Final spectrum exhibits a photopeak with higher FWHM (full width in half maximum) shifted to lower energies.
d) The detection response can be also affected by dislocations. This phenomenon is widely investigated and discussed at present time.

2. Experimental techniques

2.1. Crystal growth

Crystals based on CdTe grown by the Vertical Gradient Freeze (VGF) method and by the Vertical Bridgman method (VBM) were prepared at Institute of Physics at Charles University in Prague. The crystal AC31 was produced by Acrorad Ltd. using the Travelling Heater Method (THM).

Growth of VGF and VBM crystals was performed in two steps [38]. In the first step, 6N starting materials Cd and Te (produced by Nippon Ltd.) together with Zn or doping elements (In or $CdCl_2$) were synthesized in a synthetization furnace. At the beginning, materials were placed into the quartz ampoule with inner walls covered by graphite. The ampoule was evacuated up to 5×10^{-6}mbar, sealed and placed into the one-zone synthetization furnace, which was heated up to 450°C where materials started to form a melt. Because of strong endothermic reaction occurring during the synthesis, temperature of the ampoule was slowly heated up to 1100°C. Molten material was held at this temperature for 10 hours for homogenization and cooled down to room temperature with a cooling rate of 3°C/min. Obtained solid was used as a starting material for the second growth step – single crystal growth using VGF or VBM technique.

Slightly different technological procedures were used for VGF and BM growth. In case of the VGF growth method, the synthesized solid was placed into the boron nitride (BN) crucible with diameter 100mm. The crucible and cadmium source (intended for the pressure control) were loaded into the quartz ampoule, evacuated to 5×10^{-6}mbar, sealed off and placed into the two-zone VGF furnace. The source material was heated up to 1100°C and held for 12 hours for homogenization, then the temperature was lowered to 1085°C and the cadmium pressure was set to value 1.2atm (system state near to the CMP in Fig.1.11). The temperature gradient of the melt-solid interface was ~5°C/cm and was moved with a rate 0.5°C/h. After solidification of the melt, the crystal was cooled slowly to room temperature.

The BM growth was performed in a two-zone Bridgman furnace. Synthesized material together with a cadmium source was loaded into the carbon-coated quartz ampoule with diameter 45mm. After sealing off the ampoule, the growth process proceeded similarly as in the VGF case. Only one difference comparing to VGF growth was that during the BM growth the ampoule was moved mechanically in the temperature gradient with the speed of 3mm/h.

CdTe:Cl crystal AC31 was prepared commercially using the THM technique, whose growth conditions were unknown. Generally, 7N polycrystalline CdTe together with 6N $CdCl_2$ are loaded in a graphite-coated quartz ampoule sealed in a pure Ar gas [39]. The floating zone enriched by tellurium is heated up at temperature above 750°C with the crystallization temperature 725°C. The gradient at the crystallization interface is about 40°C/cm and its moving rate is 2mm/day (due to high constitutional supercooling which occurs during the THM growth). Finally, behind the melt-solid interface a single-crystal material is produced.

Types and properties of crystals investigated in this work are listed in Tab.2.1. To obtain relatively comprehensive understanding of the physical background, crystals with miscellaneous properties were used (crystals with or without Zn or doping elements; high and low resistive crystals; different types of inclusions; etc..). Moreover, the properties of crystals varied also within the one ingot. An example of such variances is plotted in Fig.2.1, where the material resistivity along the ingot S56 depended on the chlorine concentration. From Fig.2.2 also modulations of peak intensities in PL spectra within the same ingot can be seen.

Tab.2.1: Summary of investigated crystals and their properties.

Crystal	Growth technique	Zn concentration (%)	Doping	Doping concentration (cm^{-3})	Resistivity (Ωcm)	Type and concentration of major carriers (cm^{-3})	Shape and size of inclusions
NUK 131	VGF	4	-	-	3.5	$p=1.6\times10^{16}$	triangle-shaped up to 25µm
E20	VGF	4	-	-	2.2×10^{8}	$n\sim7\times10^{8}$	star-shaped up to 100µm
E35	VGF	-	-	-	~120	$p=5\times10^{14}$	triangle-shaped up to 30µm
E36	VGF	-	In	4×10^{14}-4×10^{15}	1.1-10	$n=4\times10^{14}$-4×10^{15}	star-shaped up to 30µm
B39	BM	-	In	4×10^{14}-4×10^{15}	7×10^{7}-4×10^{8}	$n=1\times10^{9}$-1×10^{8}	triangle-shaped up to 15µm
S53W	VGF	-	In	4×10^{16}	0.1	$n=4\times10^{16}$	no inclusions
S56	VGF	-	Cl	3×10^{16}-2×10^{17}	2×10^{5}-2×10^{9}	p-type	triangle-shaped up to 25µm
S57X	VGF	-	Cl	2×10^{17}	0.0175	$n=3\times10^{17}$	no inclusions
F44	VGF	-	Cl	4×10^{17}	1.2×10^{7}	p-type	triangle-shaped up to 30µm
AC31	THM	-	Cl	2×10^{17}	2×10^{9}	n-type	triangle-shaped up to 25µm

VGF – Vertical Gradient Freeze method, BM – Bridgman method, THM – Travelling Heater Method.

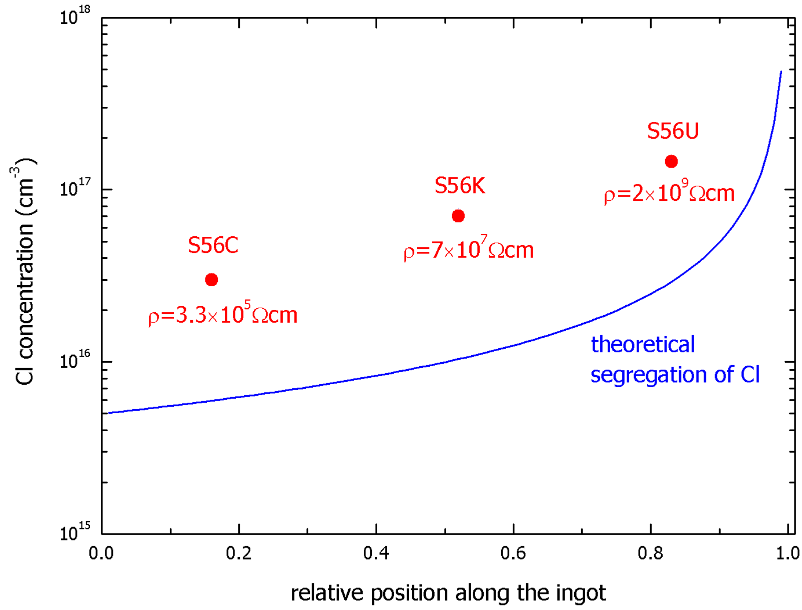

Fig.2.1: The chlorine concentration and the resistivity in different parts of the ingot S56 is depicted as red points and notes, respectively. The theoretical segregation of chlorine in CdTe calculated based on [18] is plotted by the blue line. The difference between theoretical and observed chlorine concentration segregation can be explained by a faster crystallization of the melt than optimal.

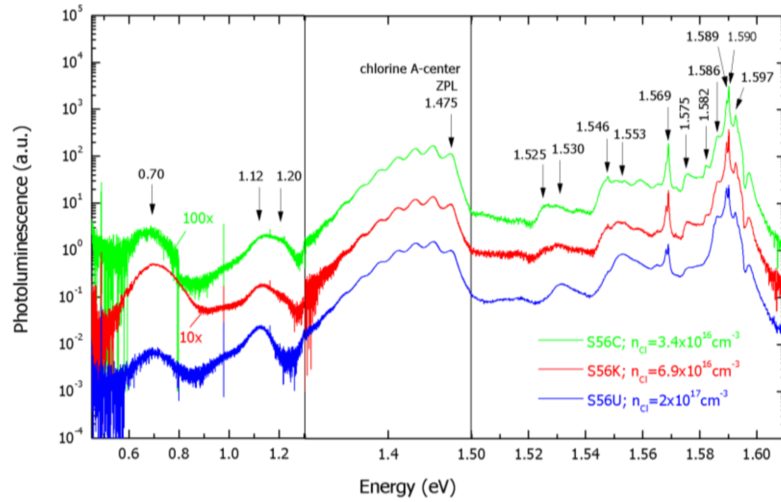

Fig.2.2: Photoluminescence spectra of samples cut from different parts along the CdTe:Cl ingot S56. Modulation of peak intensity at 1.12eV, 1.530eV, 1.553eV and 1.589eV was observed with increasing position along the ingot from the tip toward heal of the crystal. Increasing of the peak intensity at 1.589eV could be assigned to acceptor impurities (Li or Na), whose concentration increases with the position along the ingot in agreement with their segregation coefficient in CdTe [18].

2.2. Sample preparation

Planparallel wafers were sliced perpendicularly to the growth direction from grown ingots by a diamond wire saw Well Diamond Wire Saws Inc. (model 6234) with wire diameter 0.3mm (cooled by water). The thickness of wafers was usually in the range of 2-3mm. Wafers were polished by boron carbide abrasive B_4C F400 (grit size 32-8µm) to reveal the structure of grains on the wafer surface. Consequently, squared monocrystalline planparallel samples were cut from wafers by a wire saw South Bay Technology Inc. (model 850) using stainless steel wire with

diameter of 0.1mm (with abrasive boroncarbide-glycerine solution). Most of samples had dimensions $5\times5\times2.5mm^3$, the samples used for infrared transmittance measurements had dimensions $10\times10\times2mm^3$, and the samples prepared for high-temperature "*in-situ*" Hall effect measurements were $3\times3\times15mm^3$ large. After cutting, the samples were polished using finer B_4C abrasive F1000 (grit size 10-1μm) followed by a chemo-mechanical polishing in 2% bromine-ethyleneglycol solution on the silk cloth. Process was performed for 30 seconds each side. Finally, samples were etched in 2% bromine-methanol solution for 1 minute to obtain mirror-like sample surfaces.

2.3. Annealing

Annealing of samples was performed in an evacuated quartz ampoule placed in a three-zone furnace (Fig.2.3). At first, a quartz ampoule was etched by 40% HF solution for approximately 1 hour followed by the cleaning using distilled water and drying in a dryer with low dustiness. Ampoule was then filled by the sample and metal source - 6N Cd or Te - produced by Nippon Ltd. Filled ampoule was pre-evacuated to 10^{-2}mbar by rotary oil pump and consequently evacuated to vacuum about 5×10^{-6}mbar by a turbomolecular pump, sealed and placed into the three-zone furnace. Three separated heating coils in the furnace were produced from the resistance wire KANTHAL. The temperature in zones was regulated separately by three-looped thermoregulator EUROTHERM 2704 and controlled using the software in PC. The sample was placed to the part with higher temperature, metal source to the coldest part of the ampoule for the pressure control. The temperature of the sample and metal source was checked by two thermocouples of type S (Pt; Pt-Rh) placed next to the ampoule.

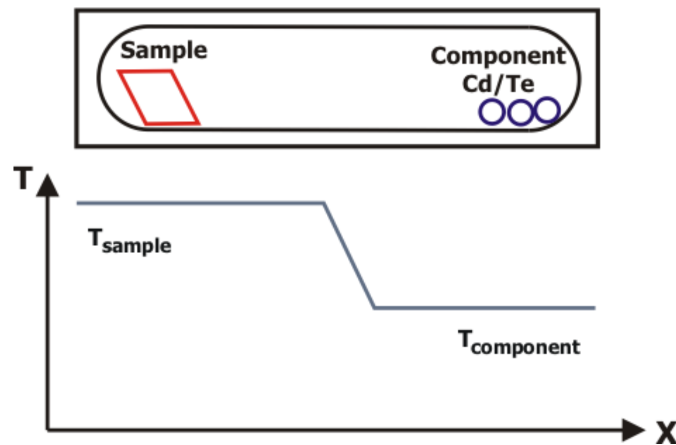

Fig.2.3: Scheme of annealing experiments in a three-zone furnace.

2.4. Microscopes

2.4.1. Infrared microscope

Optical inverted microscope OLYMPUS IX70 was used for investigation of second phase defects inside the CdTe crystals. A halogen lamp was used as a source of continuous emission spectrum. Radiation penetrating through CdTe crystal with IR transmission >60% was detected by CCD camera PULNIX TM765 with low signal to noise ratio $S/N = 50dB$. Since CdTe transmits

radiation with λ>830nm and CCD camera has the upper detection limit at λ~1100nm, the microscope imaging works with the near infrared radiation with λ~0.9µm (see the hatched area in Fig.2.4). For magnification of the defects, three objectives OLPYMPUS RMS 4x, 10x and 20x were used. When the microscope is in perfect alignment and has the objectives appropriately matched with the substage condenser, the numerical aperture *NA* of the optical system is given by NA_{obj} of used objective. If we consider the objective with the highest magnification 20x with $NA = 0.4$, then the resolution limit of the optical system is

$$resolution_{IR} = 0.61\frac{\lambda}{NA} \approx 1.4\mu m\,. \qquad (2.1)$$

Metal-based second phase defects present in CdTe absorb the near-infrared radiation and form dark objects in IR microscope images. Hence, IR microscopy is suitable technique for characterization of second phase defects with the size above 1µm. Specially prepared microscope slide with a backstop together with movable XY-stage enable to fix the sample always in the same orientation and investigate the same second phase defects before and after the annealing treatment. IR microscope images were taken using the NIS ELEMENTS software.

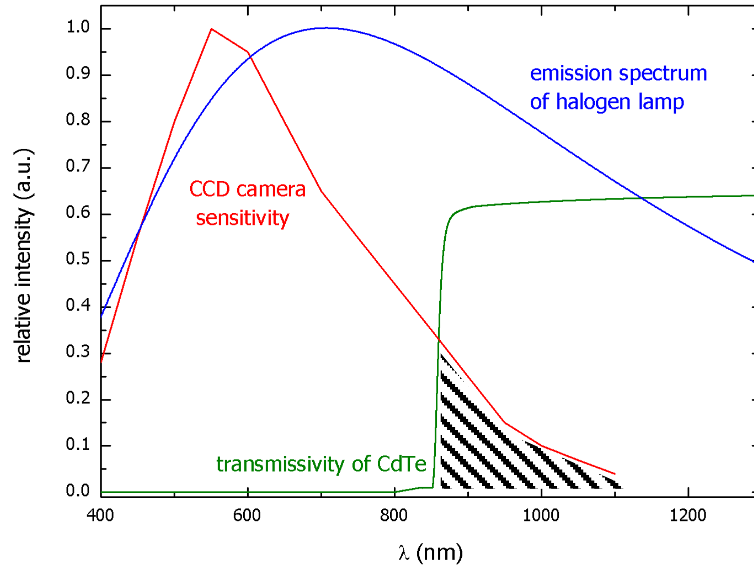

Fig.2.4: Relative intensity of emission spectrum of halogen lamp, sensitivity of CCD camera and transmittance of CdTe.

2.4.2. Optical microscope

Optical reflective microscope Leitz LABORLUX 12HL was used for detailed surface morphology investigations. Halogen lamp was used as a light source. Visible light was reflected from the upper surface of the sample placed in the movable XY-stage, was detected by the camera Leica DFC320 and processed by software IM50 in PC. The microscope was used mainly to characterization of second phase defects revealed on the sample surface by special etching or polishing treatment. Microscope has embedded four objectives NPL 10x, 20x, 50x and 100x. The resolution limit, using 50x objective with $NA_{obj} = 0.85$ and considering λ~500nm, was

$$resolution_{opt} = 0.61\frac{\lambda}{NA} \approx 360nm\,. \qquad (2.2)$$

2.4.3. Scanning electron microscope

Scanning electron microscope (SEM) CamScan S4 was intended to investigation of CdTe surface tomography and composition analysis of second phase defects revealed on the sample surface. SEM was working in two imaging and one spectroscopic mode. Surface morphology was investigated by the secondary electron and back-scattered electron imaging; chemical analysis was performed using the energy dispersive X-ray spectroscopy (EDX) system Oxford Instruments LINK ISIS 3000 with accuracy of the composition determination at level about 1%.

2.5. Transport properties

The electrical conductivity/resistivity, concentration and mobility of free carriers of CdTe were measured by three different experimental techniques. Two methods were used for measurements at room temperature depending on the sample resistivity. Electrical properties of crystals before and after the annealing with the resistivity lower than $10^7\Omega$cm were established by Hall effect measurements in the Van red Pauw configuration. Since the Hall effect method exhibited high leakage current for samples with $\rho>10^7\Omega$cm, the resistivity of semi-insulating samples ($\rho>10^6\Omega$cm) was evaluated using the contactless equipment COREMA. The free carrier concentration and mobility of samples were always measured by room-temperature Hall effect measurements. The third method was used for evaluation of transport properties directly at high temperature. These measurements were performed by "*in-situ*" Hall effect method using specially prepared welded contacts.

2.5.1. Hall effect measurements at room temperature

For determination of transport properties (electrical conductivity, carrier concentration and mobility) at room temperature the Hall effect measurements were used. Measurements were performed on samples with chemically deposited Au contacts (deposition of 10% $AuCl_3$ for 1min.). The sample with deposited contacts was glued on the holder with gold conductive channels by thermally conductive silicon paste. Gold channels on the holder were connected with gold contacts on the sample by silver wires with diameter 50μm. Silver wires were bonded with gold contacts on

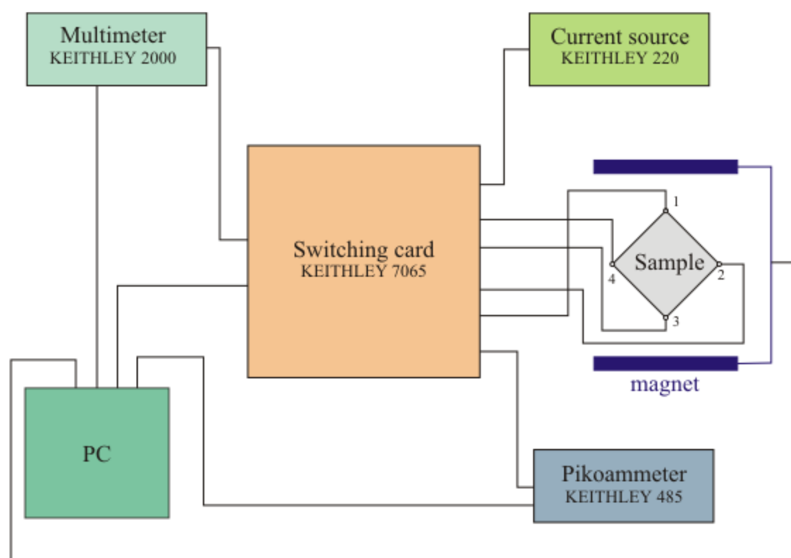

Fig.2.5: Experimental setup scheme of Hall effect measurements in the Van der Pauw configuration.

the sample by soldered indium, with gold contacts on the holder by a conductive silver or graphite paste.

The scheme of experimental setup is plotted on Fig.2.5. Hall switching card enables switching of various combinations of input current and measured voltage on contact samples. The maximal voltage applied on the switching card is limited to 10V. KEITHLEY 220 is used as a current source; the input current is controlled by a picoammeter KEITHLEY 485. Output voltage from the sample is measured by a multimeter KEITHLEY 2000. Standard bus IEEE 488 is used for communication among measuring devices and PC. The connection among the switching card, sample and measurement devices is realized by shielded cables with triaxial connectors.

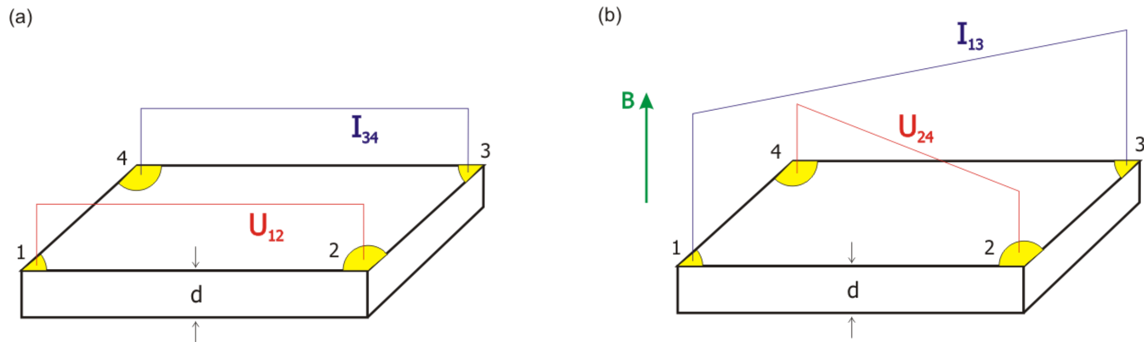

Fig.2.6: Measurement geometry for evaluation of (a) electrical conductivity and (b) Hall constant using the Van der Pauw method.

Transport properties of samples were measured by the Van der Pauw method (analogical to standard 4-point contacts technique). This method is suitable for measurement of planparallel arbitrary shaped samples (Fig.2.6). Assuming that contacts on the sample are ohmic, the electrical resistivity/conductivity measured by the Van der Pauw method is given by equation (using notation $R_{1234} = \frac{U_{12}}{I_{34}}$):

$$\rho \equiv \frac{1}{\sigma} \equiv \frac{\pi d}{\ln 2}\left(\frac{R_{1234} + R_{2341}}{2}\right) f\left(\frac{R_{1234}}{R_{2341}}\right) \tag{2.3}$$

where d is the sample thickness and f is a correction function for geometrical asymmetry of contacts (for small asymmetry $f \approx 1$). The Hall constant can be calculated from:

$$R_H = \frac{d}{B_z}\left(\frac{U_{24}^0 - U_{24}^H}{I_{13}}\right) \tag{2.4}$$

where B_z – intensity of the magnetic field oriented perpendicular to the plane of contacts

U_{24}^0 – intensity of measured voltage with $B=0$

U_{24}^H – intensity of measured voltage when the magnetic field is on.

The carrier concentration $n(p)$ and mobility $\mu_{n(p)}$ can be derived from:

$$n(p) = \frac{r_H}{e|R_H|} \tag{2.5}$$

$$\mu_{n(p)} = \frac{1}{r_H}\left|R_{H,n(p)}\sigma_{n(p)}\right| \tag{2.6}$$

where r_H is a scattering factor and usually $r_H \approx 1$.

2.5.2. COREMA

Contactless Resistivity Mapping equipment is designed for measuring of the material resistivity in the range of 10^5-$10^{12}\Omega$cm. The principle of resistivity evaluation is based on discharging of capacitor plates filled by the investigated resistive material. The lower resistivity sample has, the quicker is the capacitor discharged. The capacitor is created from the bottom gold electrode manufactured as a stationary holder "chuck" and from moving "capacitive probe" with diameter 1mm, which enables scanning of the sample area with maximal dimensions 140×140mm (see Fig.2.7). This method is suitable for quick and non-destructive resistivity mapping with submilimeter resolution. Measured samples should have planparallel etched surfaces and their thickness should not exceed 5mm.

COREMA evaluates the electrical resistivity ρ by recording the dynamic charge redistribution in a capacitive sensor that contains a portion of the material to be analyzed. The vertical resistance R_S and the vertical capacitance C_S of the material with area A and thickness d are given:

$$R_S = \rho \frac{d}{A} \tag{2.7}$$

and

$$C_S = \varepsilon\varepsilon_0 \frac{A}{d} \tag{2.8}$$

leading to

$$R_S C_S = \rho\varepsilon\varepsilon_0 \tag{2.9}$$

The arrangement to evaluation of ρ is schematically shown in Fig.2.7. The total capacity C is given by the material capacity C_S and the air gap capacity C_a (determined by the air gap capacity between the top electrode and the top sample surface) connected in series:

$$C = \frac{C_a C_S}{C_a + C_S} \tag{2.10}$$

Measurement procedure is based on rate of capacitor discharging. At time $t = 0$ a voltage step is applied to the capacitor electrodes with an initial charge

$$Q(0) = CU \tag{2.11}$$

For $t > 0$, the voltage across C_S causes a carrier transport through the sample resistance R_S, gradually discharging capacitor C_S. With decreasing voltage across C_S, additional charge is transported to C_a from the external source because the applied voltage U is held constant and

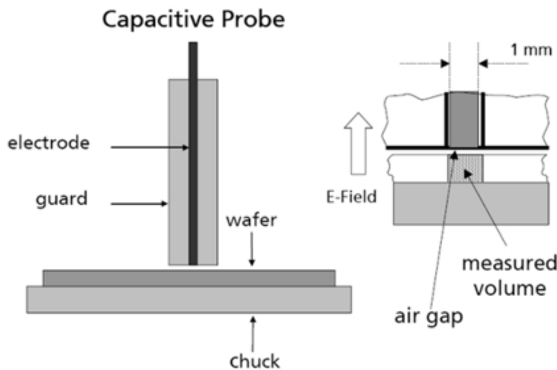

Fig.2.7: Schematic representation of the nonconctacting sensor assembly in COREMA [40].

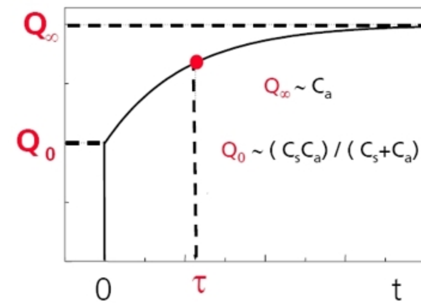

Fig.2.8: Time dependence of the total charge on the capacitors [40].

$C_a > C$. Eventually, C_S is completely discharged and the charge on C_a is

$$Q(\infty) = C_a U \tag{2.12}$$

The time dependent charge in the capacitors is described by

$$Q(t) = \frac{C_a^2}{C_a + C_S} U \left(1 - e^{-t/\tau}\right) + Q(0) \tag{2.13}$$

where $\tau = R_S(C_a + C_S)$. The transient *Q(t)*, illustrated in Fig.2.8, is recorded with a charge sensitive amplifier. By inserting the above relations for $Q(0)$, $Q(\infty)$ and τ into the equation (2.9) one can obtain

$$\rho = \frac{C_S \tau}{(C_a + C_S)\varepsilon\varepsilon_0} = \frac{Q(0)\tau}{Q(\infty)\varepsilon\varepsilon_0} \tag{2.14}$$

Desired ρ is completely determined by the material constant ε and the quantities $Q(0)$, $Q(\infty)$ and τ obtained by evaluating the time dependent charge in Fig.2.8.

2.5.3. High-temperature "*in-situ*" Hall effect measurements

This method enables measurements of transport properties directly at high temperature. Samples with dimensions 3×3×15mm were contacted in classical 6-point Hall geometry. Tungsten (or molybdenum) wires were welded under electrical discharge directly to the sample (Fig.2.9). Contacted samples together with metal source (Cd or Te) were placed to the etched quartz ampoule. The ampoule was evacuated to level about 5×10^{-6}mbar and sealed. Moreover, end of ampoule was hermetically sealed by the wax-picein. The experimental setup is plotted in Fig.2.10.

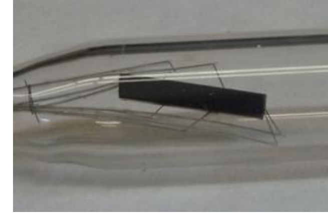

Fig.2.9: CdTe sample with welded tungsten wires.

The current source was embedded in the switching system and the output current was controlled by

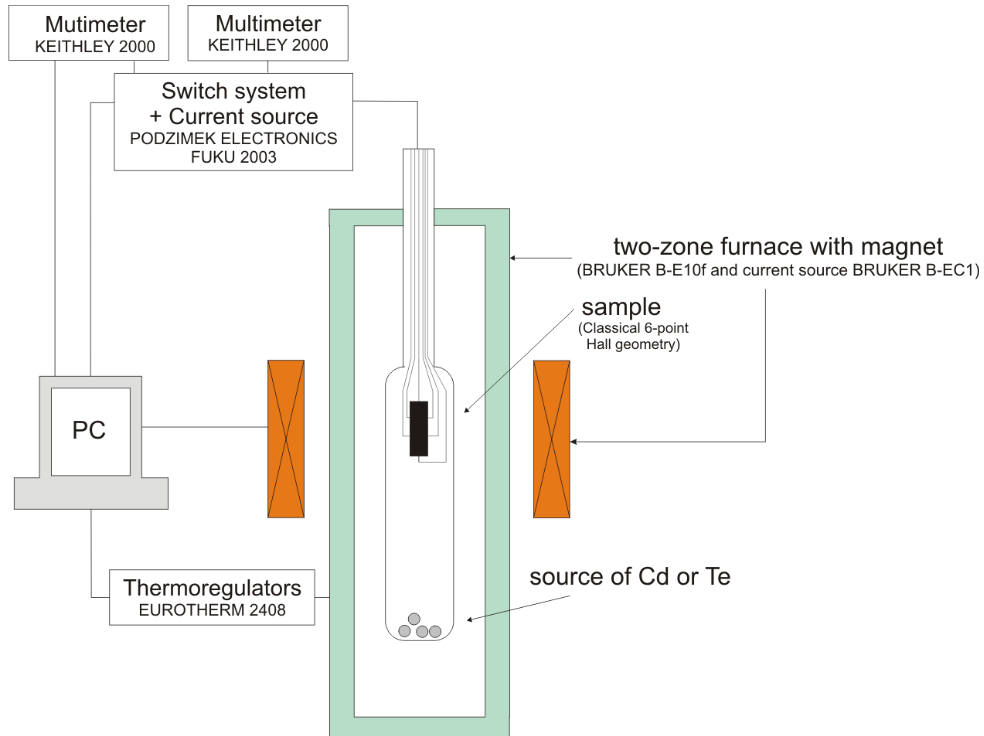

Fig.2.10: Experimental setup of the high-temperature "*in-situ*" Hall effect measurement.

one multimeter KEITHLEY 2000. Measured polarities were changed by the switching system and the output voltage was read by another KEITHLEY 2000. Temperature in the magnet-furnace system BRUKER B-E10f was set by two thermoregulators EUROTHERM 2408. All measurement devices were controlled by PC software.

Transport properties can be calculated from relations for classical 6-point geometry (Fig.2.11):

$$\sigma \equiv \frac{1}{\rho} = \frac{l}{dw} \frac{I_{56}}{U_{12}} \left(or \frac{I_{56}}{U_{43}} \right) \tag{2.15}$$

$$R_H = r_H \frac{d}{B} \frac{U_{14}^0 - U_{14}^H}{I_{56}} \left(or \frac{U_{23}^0 - U_{23}^H}{I_{56}} \right) \tag{2.16}$$

where d is the sample thickness, l is the distance between voltage contacts, w is the sample width, I is applied current, U is measured voltage and B is the magnetic field perpendicular to the contacts plane.

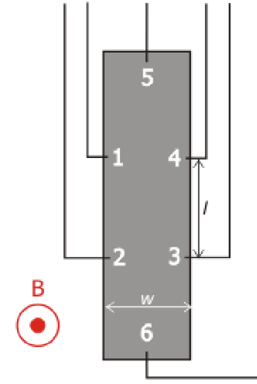

Fig.2.11: Classical Hall geometry.

Diffusion characteristics at elevated temperatures were determined based on electrical measurements. The carrier concentration and electrical conductivity represents a deviation from the stoichiometry given by the system temperature and partial pressure (P_{Cd} or P_{Te_2}). Diffusion parameters were measured as follows: sample temperature was held constant and the partial pressure was step-like changed. This step led to a relaxation of transport properties to a new equilibrium value and the diffusion constant was determined from relaxation curves using equation [31]:

$$\tilde{D}_{CdTe} = -\frac{1}{\pi^2} \left(\frac{l^2 w^2}{l^2 + w^2} \right) \frac{d}{dt} \left[\ln \left(\frac{1 - \tilde{\sigma}_t - \sigma_0}{\sigma_\infty - \sigma_0} \right) \right] \tag{2.17}$$

where σ_0 and σ_∞ are the initial and final conductivity, respectively, and $\tilde{\sigma}_t$ is the average sample conductivity at time t.

2.6. Optical properties

2.6.1. Infrared transmittance

Infrared (IR) transmittance of planparallel samples with dimensions 10mm×10mm×1.7mm was measured in the energy range of 0.1-1.6eV using two spectrometers. Spectra in the range of 0.1-0.5eV were obtained by FTIR (Fourier Transform Infrared) spectrometer Vector 33 with DTGS (deuterated triglycinsulfat) detector. DTGS is a thermal detector working on a principle of strong temperature dependence of the capacitance. Every absorption event of the infrared radiation heats the detector up and results in a capacitance change. IR transmission of samples at higher energies was measured by FTIR spectrometer Bruker IF66 (Fig.2.12) with construction ROCKSOLID, which suppresses polarization effects and increases the optical transmissivity of the equipment. The path difference between interferometer arms is determined by interference of radiation from He-Ne laser source (633nm, 1mW). The beam splitter is made from thin germanium layers deposited on the KBr substrate. The source of the light is GLOBAR – SiC rod heated at about 1000°C by the

electric current. The IR transmittance spectra were collected using the DTGS detector or Si photodiode. IR transmittance spectra with resolution 2cm^{-1} can be obtained.

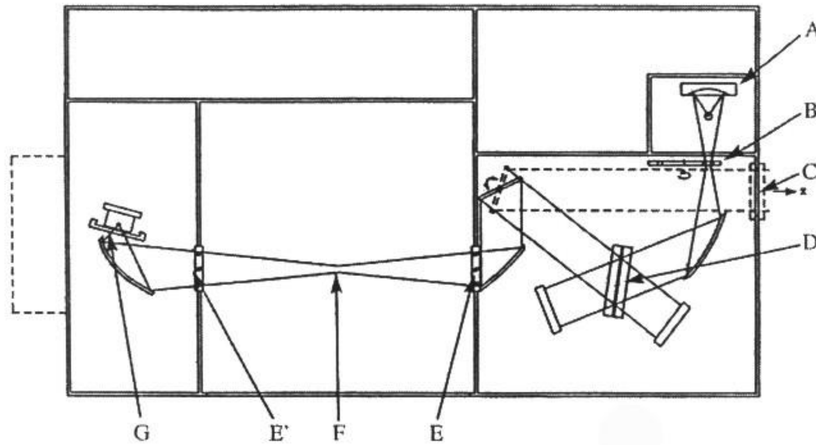

Fig.2.12: Optical scheme of FTIR spectrometer [41]. A – continuous spectrum source, B – carousel with apertures, C – aperture for external light source, D – beam splitter, E,E´ - apertures in the sample area, F – focus with the sample holder, G – detector.

2.6.2. Photoluminescence

The PL experimental setup is similar to the setup used for the infrared transmittance spectra measurements (Fig.2.12). In PL case, the source of continuous radiation was replaced by a well defined laser radiation. Samples were cooled to liquid helium temperature in the Leybold VSK 3-300 cryostat. Two lasers were used as an excitation source, either red laser Coherent Radius 635 (1.96eV) or tunable Ti:sapphire laser Spectra Physics 3900s (1.30-1.72eV). PL was detected using the Bruker IFS 66S Fourier spectrometer equipped with Si (1.05-1.82eV), Ge (0.7-1.48eV) or InSb (0.43-0.93eV) detector (see Fig.2.13).

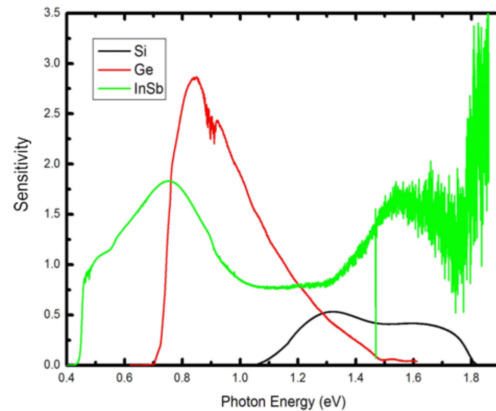

Fig.2.13: The sensitivity of Si, Ge and InSb detectors.

2.7. Detection system

Gamma-ray spectra of semi-insulating CdTe were measured on samples having planar electroless deposited Au ohmic contacts using ^{241}Am (59.5keV) gamma-ray source. The operation scheme of measurements is plotted in Fig.2.14. A current pulse created in the detector after the absorption of high energetic photon is integrated by a charge sensitive preamplifier Amptek A250 (with an input impedance 1.1GΩ) as a function of applied bias on the detector to measure the total induced charge [9]. Preamplifier produces a voltage pulse with amplitude proportional to the total induced charge. This voltage pulse is amplified by Ortec 671 and collected as a histogram in a multichannel analyzer Ortec Easy. γ-ray spectra were collected for 300 seconds at various voltages

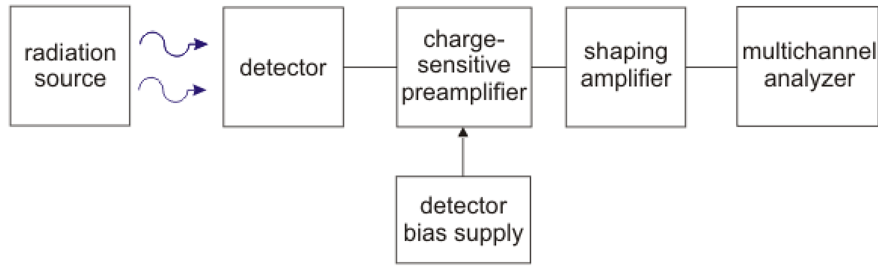

Fig.2.14: Setup for X-ray spectra collection. Based on [36].

in the range of 50-400V. The signal with energy lower than 50th channel was filtered out due to the high noise level. In case of an ideal charge collection, the energy of 59.5keV corresponds to the 270th channel in the gamma-ray spectrum.

The $\mu\tau$-product of electrons was evaluated by the α-spectroscopy using ^{241}Am (5.49MeV) source. The alpha particle source together with the detector was placed in an evacuated chamber. Then similar signal processing as in the case of γ-ray spectroscopy described in the previous paragraph was performed. In case of an ideal charge collection, the energy of 5.49MeV corresponds to the 1150th channel in the alpha-particle spectrum. The mobility-lifetime product characterizing the quality of the charge collection efficiency (CCE) can be obtained from the Hecht relation by fitting of the CCE as a function of the applied voltage *U*:

$$\eta = \frac{\mu\tau U}{d^2}\left[1 - \exp\left(-\frac{d^2}{\mu\tau U}\right)\right] \tag{2.18}$$

where *d* is the detector thickness.

Results and discussion

3. Elimination of second phase defects

3.1. Introduction

At this time, the production of high-quality substrate-grade and detector-grade CdTe-based crystals is still limited. Although more than 40 years of intensive research on this material, the size of monocrystalline grains in grown crystals is still at level of a few cm^3, the homogeneity (and resistivity in case of bulk detectors) of the material is not excellent and crystals usually contain a large number of structural defects degrading their quality. In the following paragraphs, an influence of second phase defects, especially inclusions with size of tens of micrometers, on quality of $Cd_{1-x}Zn_xTe$ substrates and CdTe-based detectors will be in more detail described.

In case of the substrate-grade material, inclusions on the substrate surface form local stress field in deposited $Hg_{1-y}Cd_yTe$ epitaxial layer. Inclusions below the deposited epilayer lead to a nonuniform layer thickness or even creation of holes or inclusions in the epilayer [6,7]. Such a deteriorate detection structure can lead to marked degradation of the infrared detector device.

Inclusions (mostly with triangle or hexagonal shape) present in CdTe-based X-ray and gamma-ray bulk detectors strongly affect their detection ability. As can be seen in Fig.3.1, even high-quality commercially produced semi-insulating CdTe:Cl or $Cd_{0.9}Zn_{0.1}Te:X_D$ (where X_D is an unknown donor) crystals contain these second phase defects [9]. Inclusions, whose size is usually few tens of microns, do not affect much the quality of large detectors ($1\times1\times1cm^3$) with two planar contacts on opposite surfaces. More problematic is situation in detectors with pixel arrays with pixel dimensions $25\times25\mu m^2$. If such a pixel contains an inclusion with the size about 20μm in diameter, inclusion plays role as a trapping center for electrons and decrease the collection of charge generated by absorption of a high-energetic photon (Fig.3.2). Finally, this pixel has different output height-pulse spectrum comparing to other pixels without inclusions (Fig.3.3), and the detection device cannot read the signal from the pixel with inclusion properly. This situation leads to formation of “dark pixels” in the detector array.

In both described problems the inclusions constitute one of the main reasons of detectors degradation. Hence, from technological point of view, it is desirable to suppress the formation of

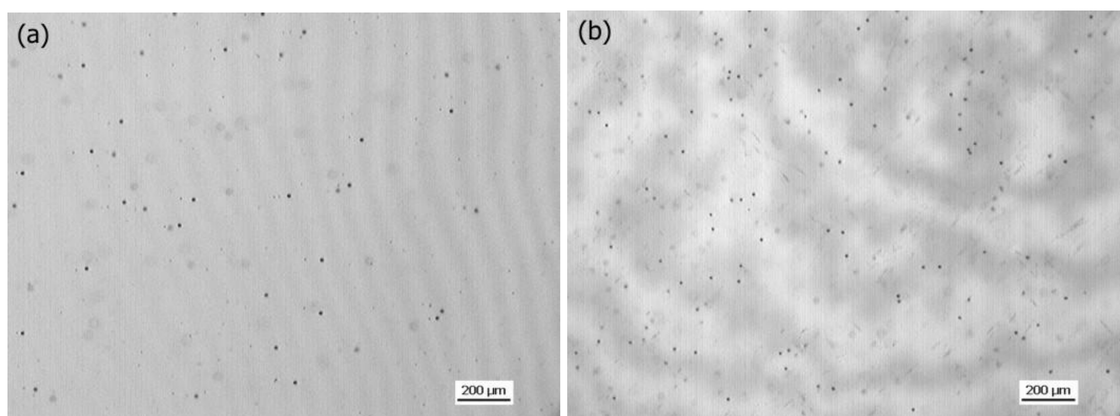

Fig.3.1: IR microscope images of inclusions present in (a) CdTe:Cl crystals produced by Acrorad Ltd. and (b) $Cd_{0.9}Zn_{0.1}Te:X_D$ crystals produced by Endicott Inc. (X_D represents an unknown donor).

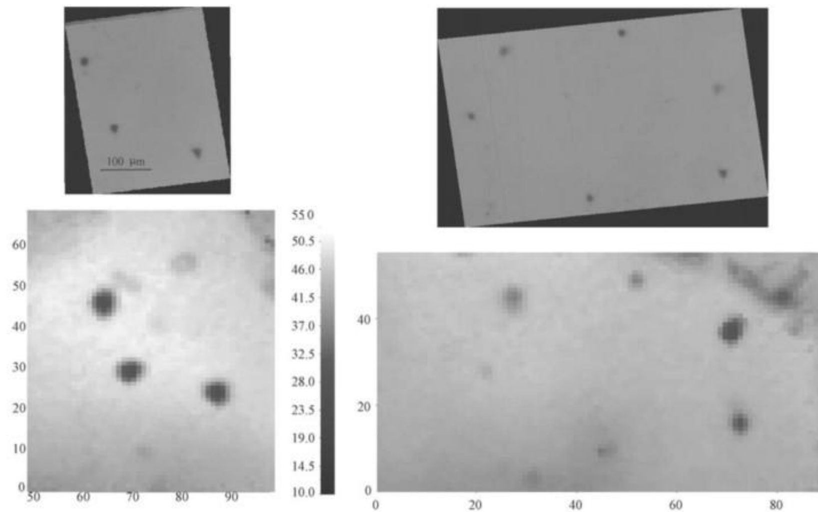

Fig.3.2: Upper two images represent maps of inclusions taken by IR microscope. Bottom two maps represent the same area as upper maps and were taken by highly collimated X-ray source with the beam dimensions 10×10μm^2, where dark areas represent marked decrease of the charge collection efficiency (CCE). As can be seen, very good correlation between the presence of inclusions and marked decrease of the CCE in detectors was found. From [47].

inclusions during the crystal growth or, if inclusions are already present in the grown crystal, to find an effective procedure for their post-growth elimination. An annealing in vapor of one of the component can take post of this procedure. However, at this time, there are few contradiction works describing the chemical composition of inclusions and suitable annealing treatment reducing the size of inclusions. There exist two types of inclusions in CdTe crystals – star-shaped and triangular-(or hexagonal-)-shaped inclusions. Rudolph et al. [29,42] reported six-pointed star-shaped Te inclusions, contrary to Brion et al. [43] and Sen et al. [8], whose star-shaped inclusions contained much more Cd than Te. In case of triangle-shaped inclusions, most of works describe them as Te-rich second phase defects [8,44,45,46].

The situation around annealing of CdTe crystals is even more complicated. Few works have been focused on improving of IR transmittance of substrate-grade CdZnTe by annealing under Cd overpressure [48,49]. They found out that annealing of as-grown p-type substrate in Cd vapor leads to an increase of its IR transmittance. However, no detail investigation of second phase defects was performed. The second set of works was concentrated on an influence of annealing on second phase defects. Shen et al. [50] obtained contradictory results of Cd-rich or Te-rich annealing

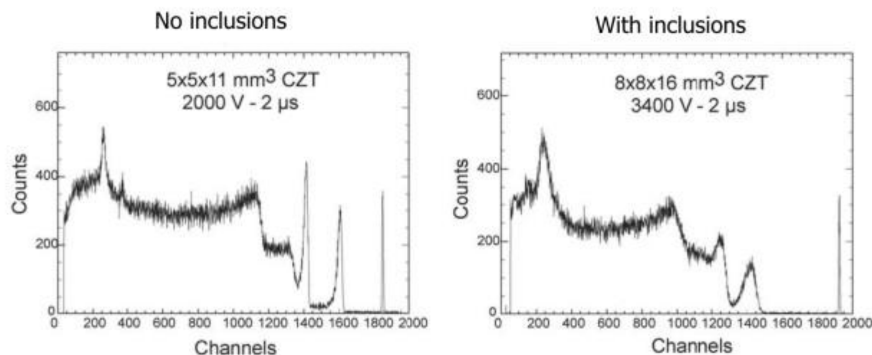

Fig.3.3: The effect of inclusions on the detection spectrum [47]. If the detector contains inclusions, the photopeaks are shifted to lower energies, their intensity decreases and their FWHM increases.

on inclusions. However, in his another work [45] he mentioned that triangle-shape inclusions can be reduced by annealing in Cd vapor at 700°C for more than 20 hours and these inclusions are not very affected by Te-rich annealing (700°C, 20h). Ayoub et al. [53,54] investigated an influence of annealing under vacuum, $CdCl_2$ and argon pressure on CdTe:Cl detector-grade material. He observed that annealing at about 450°C under argon pressure (and partly also annealing in $CdCl_2$ vapor) improved the material resistivity, nevertheless, triangle-shaped inclusions were reduced only partly. In addition, few experiments have been aimed at elimination of triangle-shaped inclusions by their thermomigration in a temperature gradient at temperature about 500°C (slightly above the melting point of tellurium) [7,51,52]. This technique was based on melting of the inclusion and consequent movement of the tellurium liquid droplet forward to the surface with higher temperature. However, it is difficult to distinguish from published experiments whether inclusions were reduced by thermomigration or by other physical process. Moreover, other properties of the material like IR transmittance or the resistivity weren't investigated.

As can be seen, a comprehensive view on problematic of second phase defects and annealing treatment is still missing. Hence, this part of the dissertation thesis will be aimed on detailed characterization of both types of inclusions by various microscope techniques and by EDX chemical analysis. Consequently, a systematic research of an influence of an annealing at constant temperature on the size and concentration of second phase defects and quality of substrate-grade and detector-grade material will be given. In case of $Cd_{1-x}Zn_xTe$ substrates, annealing research will be also focused on investigation of the influence of the annealing on the material infrared transmittance. Annealing of detector-grade materials will be aimed at reduction of second phase defects and preservation of a high material resistivity.

3.2. Characterization of star-shaped inclusions

CdTe-based crystals prepared from the cadmium-enriched melt or under Cd pressure higher than 1.2atm can contain star-shaped inclusions with diameters in the range of 5-120μm (see Fig.3.4). Inclusions exhibit usually six-pointed star shape and their size depend on the intensity of illumination of IR microscope in agreement with [43]. At very strong intensity of illumination an irregular-shaped core of the inclusion can be revealed (see Fig.3.4b) [55]. Hence, star-shaped inclusions consist of the irregular-shaped core and the star-shaped corona created from a large number of small inclusions/precipitates. To investigate detailed morphology of star-shaped inclusions, one of these inclusions was revealed on the surface of $Cd_{0.96}Zn_{0.04}Te$ substrate by a

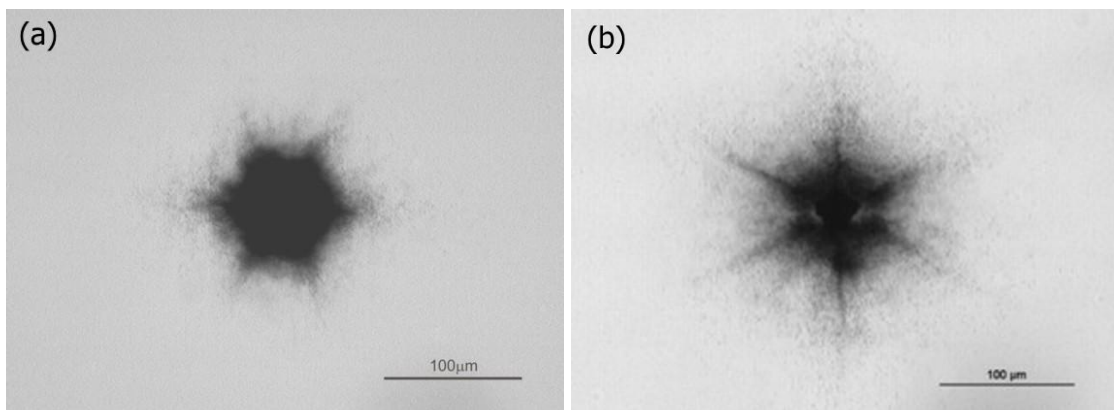

Fig.3.4: (a) – IR image of typical star-shaped inclusion. (b) – inclusion core visible at high intensity of illumination.

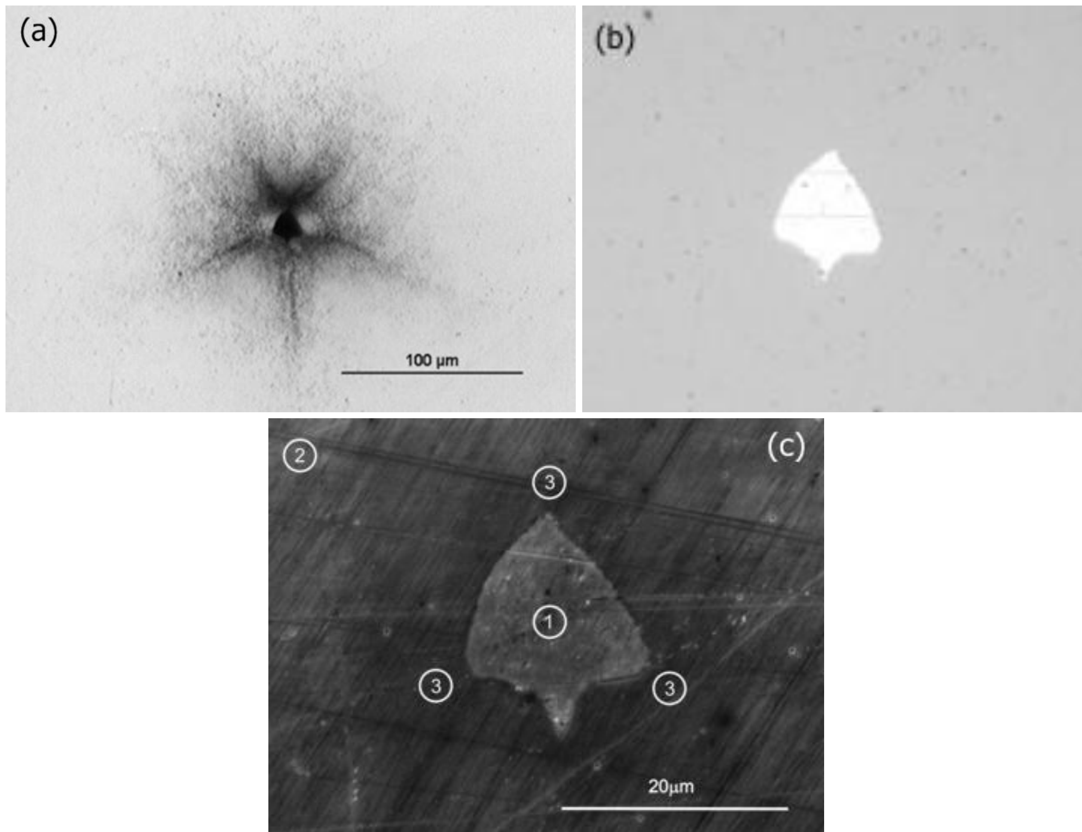

Fig.3.5: Star-shaped inclusion revealed on the surface characterized by (a) infrared, (b) optical and (c) scanning electron microscopy.

special polishing treatment using an abrasive with diamond particles [30]. The inclusion was characterized by IR microscopy (Fig.3.5a), where typical irregular core and star-shaped corona were visible; by optical microscopy (Fig.3.5b) and by scanning electron microscopy using the secondary electron imaging (Fig.3.5c). As can be seen in Figs.3.5b and 3.5c, after polishing only irregularly-shaped core of the inclusion was revealed on the surface. Numbers in Fig.3.5c represent the positions of the composition analysis shown in Tab.3.1. Irregular inclusion core contained only pure Cd and the matrix surrounding the core did not deviate from the stoichiometry. Obtained results are in agreement with Brion et al. [43] and Sen et al. [8] and star-shaped inclusions will be in the following text noted as Cd inclusions.

The question remains, what is the formation mechanism of Cd inclusion with star-shaped corona visible by the IR microscopy. The whole process of Cd inclusion creation begins during the solidification. At the crystallization interface, melt enriched by cadmium (due to the higher Cd concentration than Te in starting materials or due to the high applied cadmium pressure) is formed ahead of the solid-liquid interface. Cd-enriched droplets can be trapped from the melt at the interface (instabilities, constitutional supercooling) and are present in crystallized solid. During cooling of the crystal, CdTe crystallizes from the droplet, the size of droplet is decreasing and the

Tab.3.1: Composition of the $Cd_{0.96}Zn_{0.04}Te$ matrix and Cd inclusion determined by EDX.

Position of the Composition Analysis	Cd (at.%)	Te (at.%)	Zn (at.%)
1. Inclusion	100	0	0
2. Matrix	47.6	50.4	2.0
3. Matrix around the inclusion	48.3	49.5	2.2

Cd-enrichment of the droplet is increasing. Since the thermal expansion coefficient of Cd ($31\times10^{-6}K^{-1}$) is much higher than of CdTe ($4.5\times10^{-6}K^{-1}$), during cooling of the crystal a mechanical stress around Cd droplets is originating. This stress is relaxed by creation of screw dislocation narrow loops in <110> crystallographic directions (see the chapter 1.6). Simultaneously, due to the retrograde solubility of the solidus line, (rather Cd-rich) heterogeneous precipitates are formed preferentially on the dislocation loops around droplets. Below the temperature 321°C, Cd solidifies and Cd-rich inclusions decorated by precipitates on star-shaped dislocation loops are formed [30,43]. The size of precipitates is usually at level about 1μm.

3.3. Characterization of triangle-shaped inclusions

Triangle- or hexagonal- shaped inclusions are most common second phase defects present in CdTe-based crystals (Fig.3.6). The density of these inclusions is usually 10^4-10^5cm^{-3} and their size varies between 1 and 30 μm. The size of inclusions is independent of illumination intensity of IR microscope and the rim of the inclusions is sharp [43]. Detailed morphology and composition analysis was performed on one triangle-shaped inclusion revealed on the surface after etching in a 1% Br-methanol solution [30]. This inclusion was investigated by IR microscopy (Fig.3.6a), optical

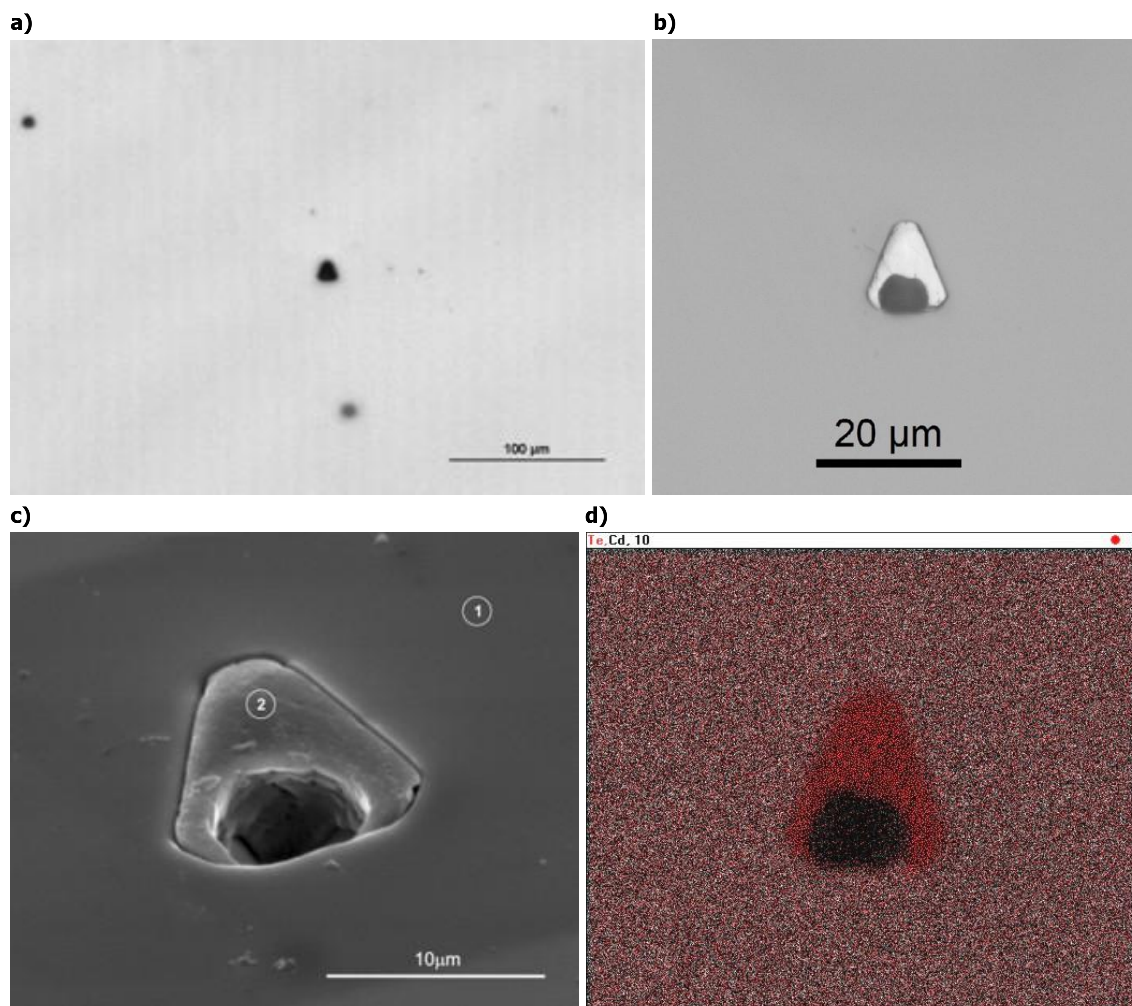

Fig.3.6: (a) IR microscope, (b) optical microscope and (c) SEM image of a triangle-shaped inclusion. Picture (d) represents the EDX spectrum, where red points correspond to pure Te and white points represent pure Cd.

microscopy (Fig.3.6b), scanning electron microscopy using the secondary electron regime (Fig.3.6c) and its composition was determined by the EDX analysis (Fig.3.6d). Numbers in Fig.3.6c represent the positions of the composition analysis listed in Tab.3.2. Investigated inclusion was completely filled by pure tellurium [30] in agreement with [8,44,45,46] and in the following text triangle- and hexagonal- shaped inclusions will be noted as Te inclusions. In addition, most of inclusions revealed on the surface contained an empty void inside. These voids were found also in [8] after polishing by Al_2O_3 and by special chemical treatment in [45]. Therefore, it is expected, that voids are not a result of the surface treatment but are more probably formed during either crystallization of the melt or during cooling down of the crystal.

Tab.3.2: Composition analysis of $Cd_{0.96}Zn_{0.04}Te$ matrix and Te-rich inclusion determined by EDX.

Position of the composition analysis	Cd (at.%)	Te (at.%)	Zn (at.%)
1. Matrix	47.3	49.8	2.9
2. Inclusion	0	100	0

It is supposed, that origin mechanism of Te inclusions is similar to mechanism of Cd inclusions formation [30]. During solidification of the melt proceeding on the Te-rich side of the *T*-*x* phase diagram, Te-enrichment ahead of the crystallization interface is created (due to the constitutional supercooling and thermodynamic instabilities) and Te-enriched droplets can be formed in the solidified matrix. During the cooling of the crystal, CdTe crystallizes from droplets, the size of droplets is decreasing and Te-enrichment is increasing. Similarly as in case of Cd inclusions, this process is connected with formation of the mechanical stress due to a thermal expansion coefficient misfit. However, the difference of thermal expansion coefficients between CdTe ($4.5\times10^{-6}K^{-1}$) and Te ($14.7\times10^{-6}K^{-1}$) is not so large [43]. In addition, in Te-enriched droplets, beside the stress relaxation by dislocations formation, segregation of V_{Cd} as dominant Te-rich defect can also participate on the stress relaxation. The segregation of V_{Cd} represents shrinkage of the droplet and an effective contraction of the lattice around the droplet. Hence, the mechanical stress is continuously relaxed by segregation of V_{Cd} leading to creation of an empty void inside the droplet. After solidification of the droplet below 451°C an inclusion completely filled by pure Te with a void and without dislocation loops (with precipitates) around the inclusion is created [30].

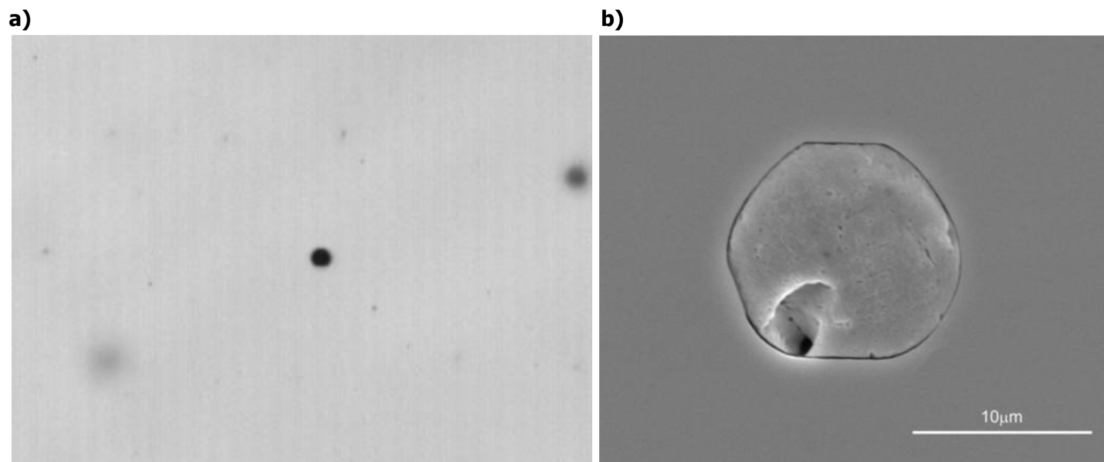

Fig.3.7: (a) IR microscope image and (b) SEM image of a hexagonal-shaped Te inclusion.

3.4. Inclusion reduction

Since the chemical composition of both types of inclusions was successfully determined, further experiments were focused on finding an optimal annealing recipe for their reduction. Annealing experiments were performed systematically for a wide range of annealing temperatures, pressures and cooling rates after the annealing. The aim was to effectively eliminate inclusions by a one-day annealing. Moreover, it was desirable to improve by annealing also the IR transmittance of $Cd_{0.96}Zn_{0.04}Te$ substrates and keep the resistivity of CdTe-based detectors above $10^8\Omega$cm after the annealing. Annealing was performed in an evacuated ampoule, where the sample was placed at the temperature plateau with higher temperature. 6N source of Cd/Te was placed to the coldest part of the ampoule for the partial pressure control. The notation e.g. 700/600°C used in next paragraphs will represent the sample temperature/temperature of the metal source. Applied temperature of the sample and partial pressure were determinate by the stability region of the *P-T* phase diagram (given by the sublimation line at low pressures and by the 3-phase line at high pressures). Atoms distribution in the crystal lattice was modified in dependence on applied annealing temperature and partial pressure by diffusion. The diffusion rate was given mainly by annealing temperature, but could be affected also by material parameters (faster in samples with grain boundaries, slower in samples with enhanced concentration of impurities in the crystal lattice).

At the beginning, samples containing Cd inclusions were annealed in Cd or Te vapor to inclusions reduction. Then similar experiments were performed also on crystals with Te inclusions. $Cd_{0.96}Zn_{0.04}Te$ substrates were characterized by IR microscopy, Hall measurements and IR transmittance measurements before and after every annealing step. Detector-grade materials needed more complex characterization and were investigated by IR microscopy, resistivity measurements, photoluminescence and detection measurements before and after annealing steps. Annealings under Cd overpressure were performed in the temperature range of 500-1000°C, Te-rich annealings were done in the range of 500-850°C. To conclude, the annealing experiments were aimed at finding of an effective method of inclusion reduction and IR transmission enhancement in substrate-grade materials. In case of detector-grade CdTe materials, the work was focused on effective inclusion reduction and the resistivity preservation using a suitable thermal treatment.

3.4.1 Annealing of crystals with Cd inclusions

Annealing in Cd vapor

$Cd_{0.96}Zn_{0.04}Te$ substrates containing Cd inclusions with diameters up to 120µm were

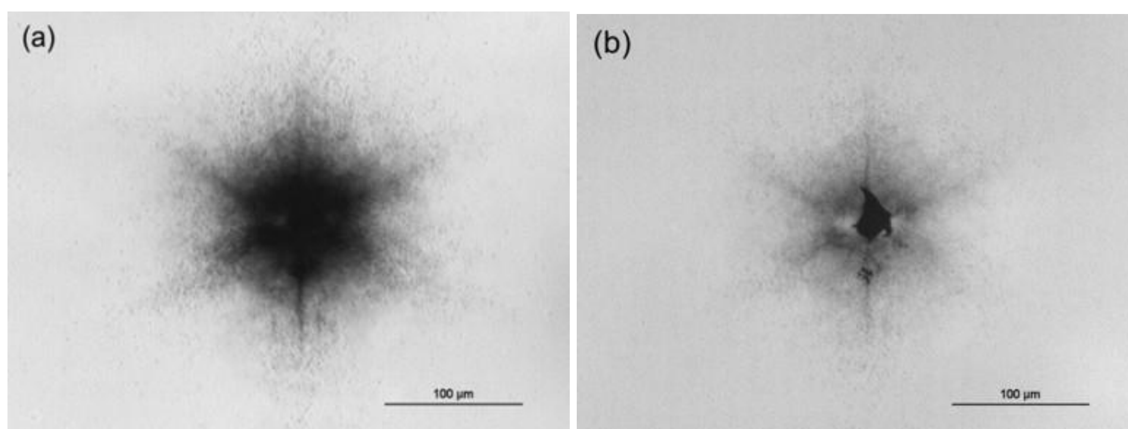

Fig.3.8: IR images of the same Cd inclusion (a) before and (b) after the annealing in Cd vapor.

annealed at various temperatures under Cd pressure in the temperature range of 600-900°C. It was found out that Cd-rich annealing reduces the inclusions size only partly [55]. Especially, inclusions corona was only partly reduced and irregular-shaped inclusion core was revealed (Fig.3.8). The IR transmittance of the substrate was high before annealing and remained excellent also after the Cd-rich annealing (see black and red lines in Fig.3.10). Even annealing at 900°C for 24 hours did not remove the inclusion corona completely. Since the corona of Cd inclusions was affected by Cd-rich annealing only slightly, it can be supposed that corona is formed from cadmium precipitates located on dislocation loops. Similar results were observed also in CdTe:In crystal with Cd inclusions.

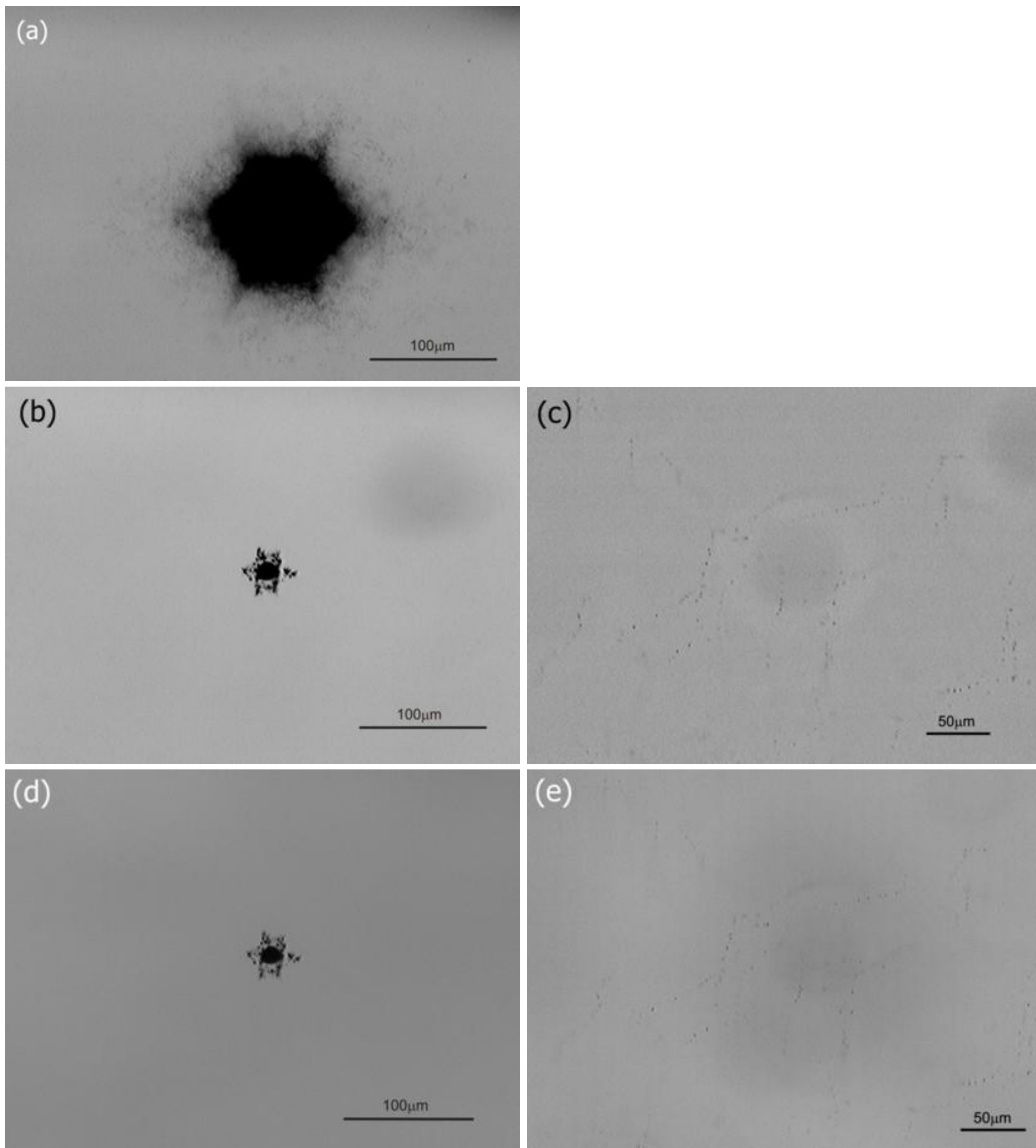

Fig.3.9: IR images of the sample with Cd inclusions (a) annealed in Te vapor at 700/590°C for 24 hours with a cooling rate of 1.5°C/min. The corona of Cd inclusion was completely removed (b) and new Te precipitates were created on dislocations (c). Re-annealing of the sample in a Cd atmosphere at 700/600°C for 24 hours with a cooling rate of 1.5°C/min. affected neither the size of inclusion core (d) nor the size of Te precipitates (e).

Annealing in Te vapor

Substrate-grade $Cd_{0.96}Zn_{0.04}Te$ samples and CdTe:In with Cd inclusions (Fig.3.9a) were annealed in a Te atmosphere in the temperature range of 500-850°C. It was found out that Te-rich annealing at temperature above 650°C completely removed the corona of Cd inclusions and the inclusion core exhibited more rounded shape (Fig.3.9b) [30]. Moreover, new type of small precipitates (~1μm) was created preferentially on dislocations (Fig.3.9c). Since precipitates were created at positions different from the original positions of as-grown Cd inclusions, they are expected to have a Te-rich composition. Based on obtained results it can be deduced that Te-rich annealing leads to a relaxation of dislocations surrounding the Cd inclusions. It is expected that Cd precipitates in the inclusion corona were eliminated by in-diffusion of cadmium vacancies during Te-rich annealing.

As a second step, the sample with Te precipitates shown in Fig.3.9b,c was re-annealed in Cd atmosphere at conditions 700/600°C for 24 hours with the aim of eliminating Te precipitates [30]. However, the concentration of Te precipitates remained unchanged (Fig.3.9e), probably because of the lower sensitivity of Te precipitates located on dislocations to Cd-rich annealing. The core of inclusions remained also unchanged after the second annealing step under Cd pressure (Fig.3.9d).

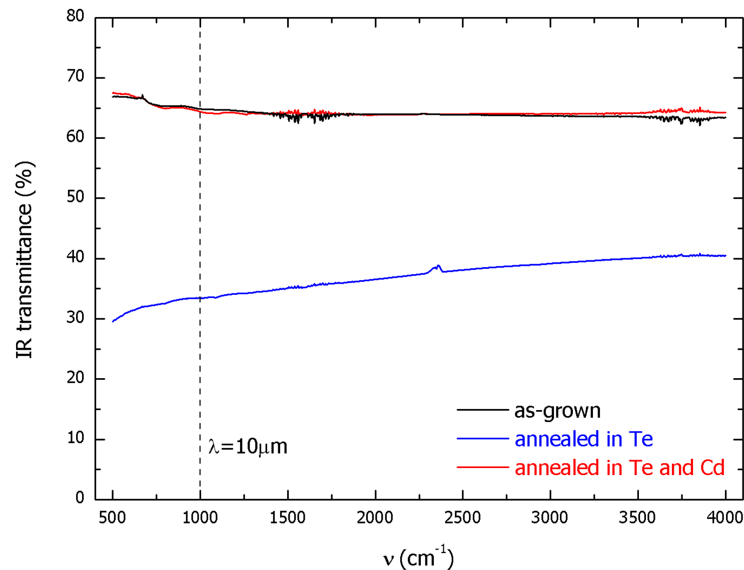

Fig.3.10: IR transmittance of as-grown Cd-rich $Cd_{0.96}Zn_{0.04}Te$ (black line), after annealing in Te vapor (blue line) and after re-annealing in Cd vapor (red line). The maximal IR transmittance of CdTe in measured range is about 65%.

Since annealing of crystals with Cd inclusions in Te vapor seemed to be more effective than annealing under Cd pressure, Te-rich annealing can be used for marked inclusions reduction. Simultaneously, also the effect of such an annealing on IR transmittance of substrate-grade material was investigated. It was found that Te-rich thermal treatment significantly decreased the IR transmittance of the substrate (Fig.3.10). However, restoration of initial excellent IR transmittance to value about 65% in the application attractive region around λ=10μm was observed after re-annealing of the material in a Cd atmosphere [30].

3.4.2. Effect of the post-anneal cooling rate

A new type of second phase defects was observed in samples after annealing in a Te atmosphere followed by a fast post-anneal cooling. Since V_{Cd} is the dominant native Te-rich point defect during Te-rich annealing, it is expected that the composition of precipitates is Te-rich and they consist of empty voids created by precipitation of V_{Cd}. The size and density of new Te precipitates depended on the applied annealing temperature, partial tellurium pressure and post-anneal cooling rate. It was found that the cooling rate after the annealing is the most important parameter determining the size and density of Te precipitates (Fig.3.11) [30]. The highest density of precipitates with size up to few microns was observed in samples quenched in the air after the annealing (Fig.3.11a). After application of slower cooling, precipitates were created mainly on dislocations and formed chain-like defects visible in IR microscope images (Figs.3.11b,c). It was found out that for suppression of Te precipitates formation below the resolution limit of the IR microscope, an application of a slow post-anneal cooling below 1°C/min is necessary (Fig.3.11d). This effect can be explained based on the analysis of the equilibrium phase diagram *T-x* of CdTe plotted in Fig.3.12. During Te-rich annealing [V_{Cd}] is set at elevated value. During slow post-anneal cooling (blue line in Fig.3.12) [V_{Cd}] reaches the maximal solubility of tellurium in the crystal lattice given by the solidus line. With decreasing temperature, [V_{Cd}] is equilibrated with the retrograde shape of the solidus line by out-diffusion of V_{Cd} from the crystal. Diffusion rate decreases with decreasing temperature. At a certain temperature, where the diffusion rate of V_{Cd} is too low to be able to equilibrate [V_{Cd}] with the maximal solubility, excess V_{Cd} starts to precipitate. Since the

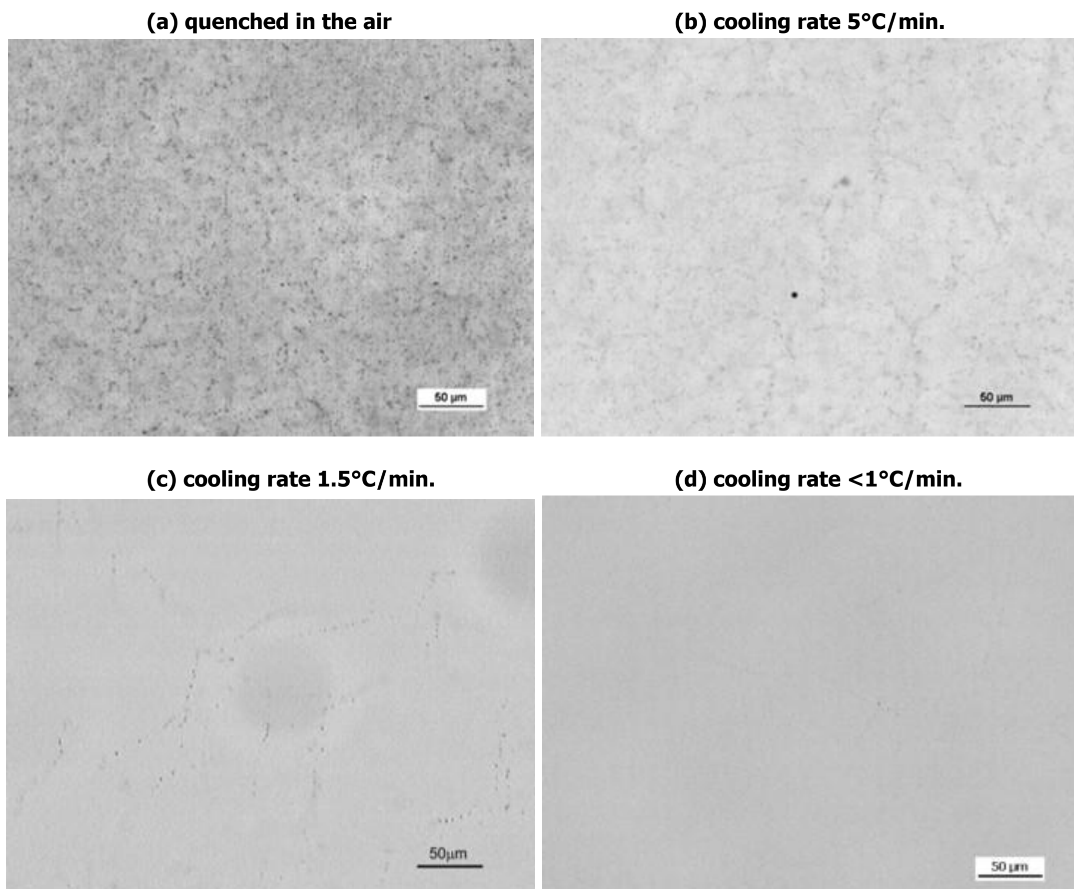

Fig.3.11: Dependence of the size and density of Te precipitates on the cooling rate after Te-rich annealing. Samples were annealed at similar annealing conditions under Te overpressure: 700/600°C for 24 hours, only sample (a) was quenched after annealing at 800/700°C for 24 hours.

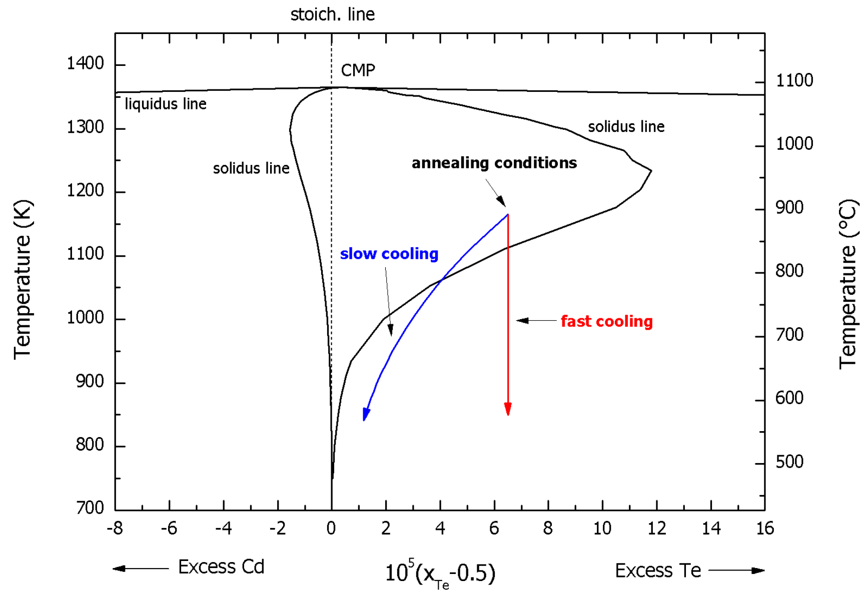

Fig.3.12: Schematic sketch of a slow (blue line) and fast (red line) post-anneal cooling in the equilibrium *T-x* phase diagram.

precipitation starts at temperature much lower than the annealing temperature, the excess of V_{Cd} during precipitation is not very large and only small precipitates are created. Different situation occurs during fast post-anneal cooling (red line in Fig.3.12). An elevated value of V_{Cd} set by annealing remains practically unchanged in the crystal during the whole cooling process. After the crossing of the solidus line, excess concentration of V_{Cd} starts to precipitate in the whole volume (and preferentially on dislocations). After creation of a huge number of small precipitates, the amount of precipitates remains unchanged and remaining excess of V_{Cd} starts to increase the size of precipitates created earlier. Hence, a huge density of large (few µm) precipitates is observed after the quick post-anneal cooling in IR microscope images.

In addition, an influence of the chlorine doping level on the size and density of Te precipitates was investigated. For this purpose, three types of CdTe:Cl samples with doping levels $n_{Cl}^1 = 3.4\times10^{16}\,cm^{-3}$, $n_{Cl}^2 = 6.9\times10^{16}\,cm^{-3}$ and $n_{Cl}^3 = 2\times10^{17}\,cm^{-3}$ were used. However, no

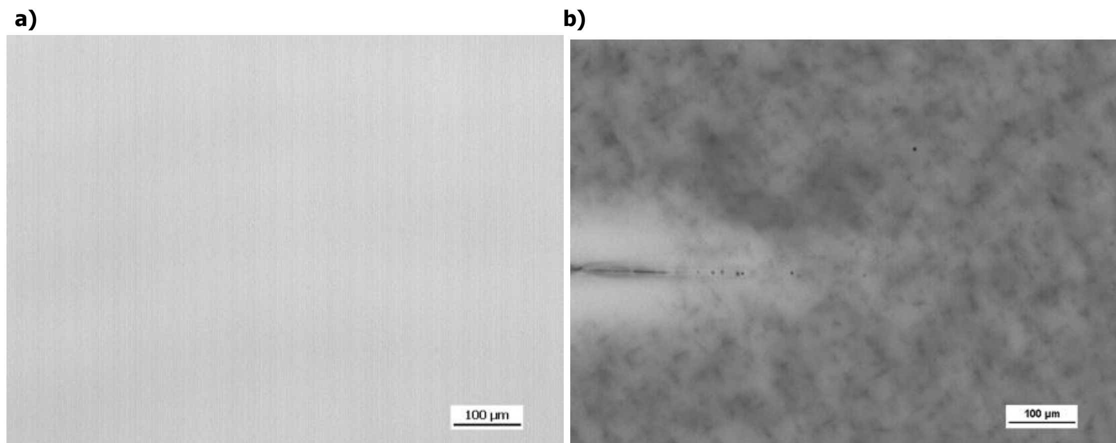

Fig.3.13: (a) Undoped CdTe sample after Cd-rich annealing followed by a slow cooling (<2°C/min.). (b) represents an undoped CdTe sample with Cd precipitates created after annealing in a Cd atmosphere at above 900°C for 24 hours followed by quenching in the air. Moreover, preferential (heterogeneous) precipitation of point defects on a crystal imperfection (chain-like imperfection) can be seen on the left side of Fig.3.13b.

dependence of Te precipitates morphology on the chlorine content was found.

Similar experiments were also performed under Cd overpressure. In this case, precipitates observable by IR microscopy were obtained by quenching of the sample after Cd-rich annealing at temperature above 850°C (Fig.3.13). The size of created Cd precipitates was below the resolution limit of the IR microscope (<1μm). The explanation of Cd precipitates formation can be based on similar analysis of the *T-x* phase diagram as for Te precipitates. During the annealing, the system state is near the Cd saturation given by the solidus line on the Cd-rich side. Fast post-anneal cooling leads to the precipitation of excess Cd-rich native defects (mainly Cd_i) formed during the annealing resulting in creation of Cd precipitates.

3.4.3. Annealing of crystals with Te inclusions

Annealing in Te vapor

Most of grown CdTe crystals usually contain the second type of inclusions – Te inclusions. At first, an influence of annealing in a Te atmosphere on Te inclusion morphology was investigated. Few undoped CdTe samples containing inclusions with the size up to 30microns were annealed in the temperature range 600-800°C under Te overpressure with a cooling rate of

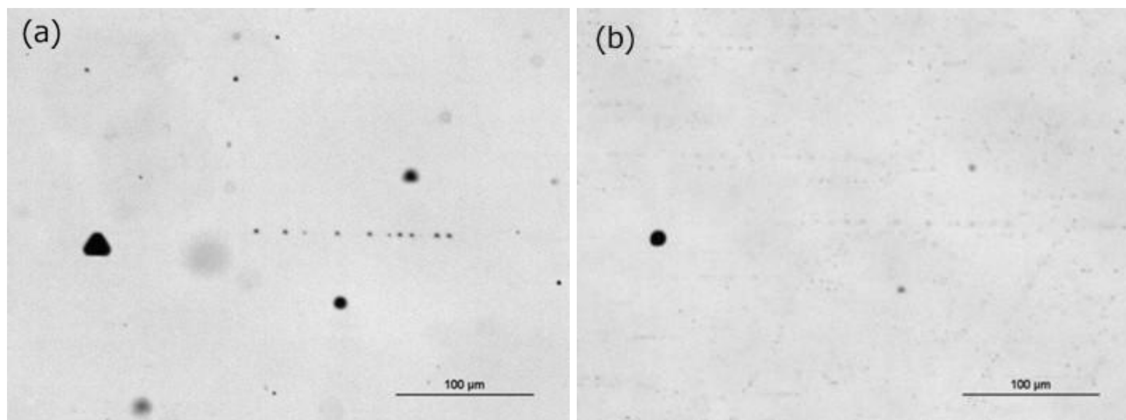

Fig.3.14: IR microscope image of the sample with Te inclusions (a) before and (b) after annealing in Te vapor at 800°C for 24 hours followed ba a cooling rate of 2°C/min.

2°C/min. Typical result of such an annealing is showed in Fig.3.14. The size of inclusions decreased only slightly and the morphology of inclusions was changed to a more circular shape [55]. After the annealing also Te precipitates with the size up to few micrometers were formed.

Annealing in Cd vapor

Since the Te inclusions were not much affected by annealing in a Te atmosphere, effect of Cd-rich annealing on these second phase defects was investigated. Experiments were performed on a large number of samples prepared from various crystals (CdZnTe substrates, undoped CdTe and CdTe:Cl detectors prepared by various growth techniques). A typical size of Te inclusions was in the range of 20-30μm. Beside these large inclusions, some crystals (CdZnTe samples and few undoped CdTe samples) contained also small inclusions with the size up to few microns, which usually formed “chain-like” structures visible by the IR microscopy. A systematic research of annealing under Cd-rich conditions was performed in a wide temperature range of 500-1000°C. After the annealing, a cooling rate of 1-2°C/min. was applied.

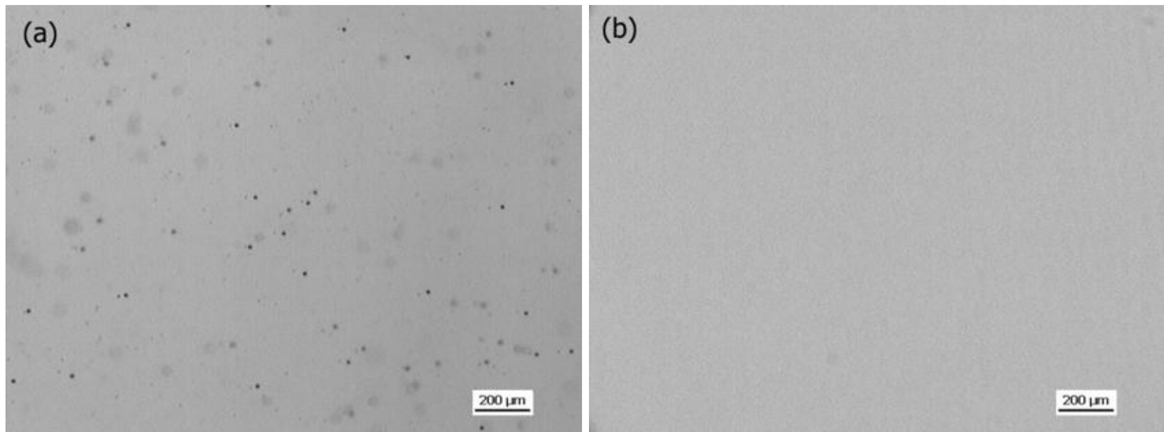

Fig.3.15: IR microscope image of CdTe:Cl crystal prepared by the THM technique (a) before and (b) after annealing in Cd vapor at 700/600°C for 24 hours.

It was found that the effect of Cd-rich annealing was slightly different for various crystals. The results can be divided into three groups. The first group is represented by CdTe:Cl crystal prepared by the Travelling Heater Method (THM) produced commercially by Acrorad Ltd. It is expected that these crystals were prepared from high-purity 7N starting materials. Hence, these crystals contain probably very low concentration of impurities. $Cd_{0.96}Zn_{0.04}Te$ and undoped CdTe crystals prepared by the Vertical Gradient Freeze (VGF) technique can be included into the second group. These crystals were prepared from 6N starting materials and, beside large Te inclusions, contained also small inclusions with the size up to few microns. The third group of crystals was formed by CdTe:Cl crystals prepared by VGF method using 6N Cd and Te and only 3N $CdCl_2$.

It was found out that Cd-rich annealing of the first group of crystals at 700/600°C for 24 hours with a cooling rate of 1.5°C/min. completely eliminated all Te inclusions (Fig.3.15) and no second phase defects were visible by IR microscopy in samples from the first group [56].

In samples from the second group, annealing in Cd vapor at temperature higher than 650°C for 24 hours with a cooling rate slower than 2°C/min. was found to be an effective thermal treatment for reduction of the size of larger Te inclusions (Fig.3.16). On the contrary, small inclusions (the size up to few micrometers) were not eliminated even after Cd-rich annealing at 1000/870°C for 24 hours. It is expected [30] that small inclusions, organized in the geometrical

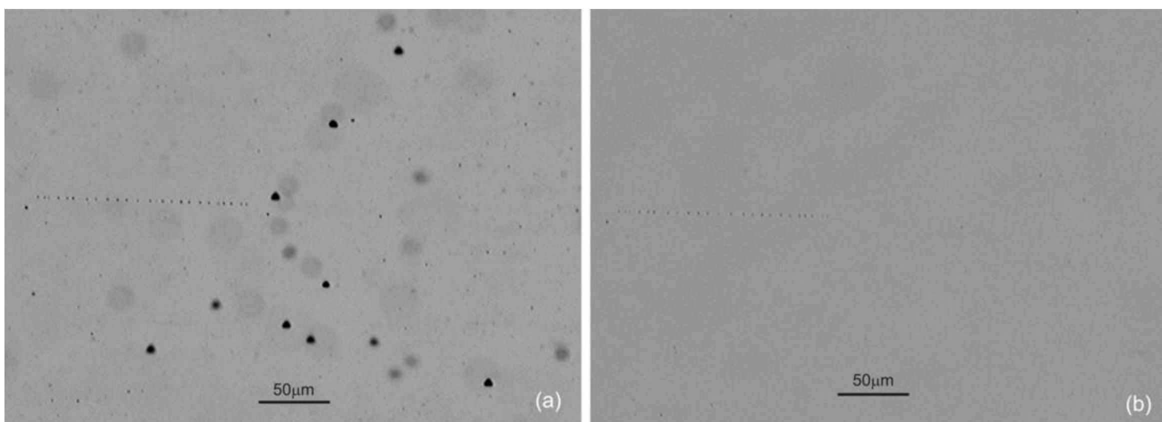

Fig.3.16: IR microscope image of $Cd_{0.96}Zn_{0.04}Te$ and undoped CdTe crystal prepared by the VGF method (a) before and (b) after annealing in Cd vapor at 700/600°C for 24 hours. Small inclusions forming a “chain-like” structure on the left side of the image remained practically unchanged even after annealing at 1000°C for 24 hours.

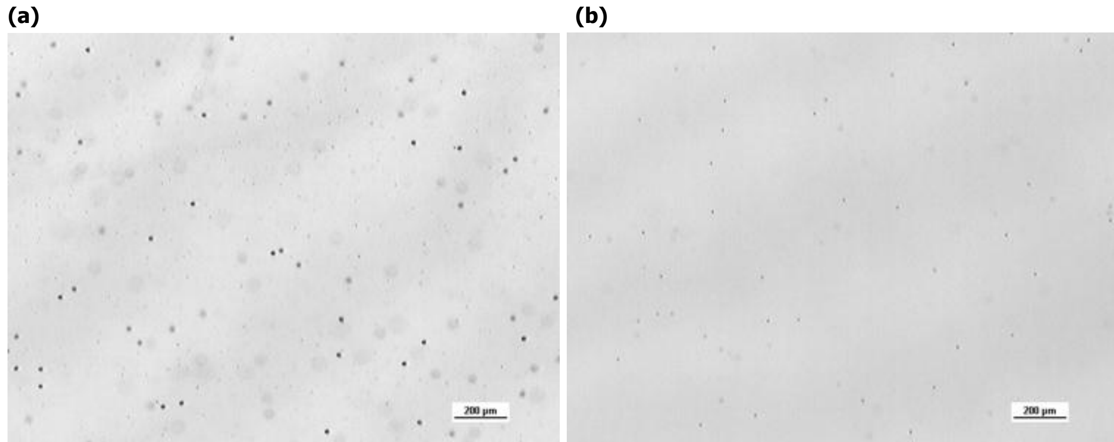

Fig.3.17: IR microscope image of CdTe:Cl prepared by the VGF method (a) before and (b) after annealing in Cd vapor at 700/600°C for 24 hours.

structures, are situated on grain boundaries, dislocations or other crystal imperfections, where they compensate the strain induced by the extended defects. Small inclusions are stabilized at their positions by relaxed strain energy, being consequently less sensitive to annealing and hardly eliminated by it. The nature of remained small inclusions after the Cd-rich annealing is unclear.

Annealing of crystals from the third group in a Cd atmosphere below 700°C for 24 hours was found to be not sufficient for significant inclusion elimination (Fig.3.17). Hence, Cd-rich annealing at 800/750°C for 24 hours was necessary for reduction of the inclusion size below 3μm [56]. It is expected that application of higher annealing temperature was necessary due to slower diffusion within this crystal. Slow diffusion was probably caused by increased concentration of impurities in the crystal lattice indirectly observed by photoluminescence, where increased amount of dominant peaks was observed in the bound exciton region (see Fig.3.23). This assumption was verified by "*in-situ*" high-temperature Hall effect measurements performed at 600°C under Cd overpressure (Fig.3.18). The relaxation time necessary to reach a new equilibrium state in CdTe:Cl prepared by the VGF was approximately 10-times longer comparing to undoped CdTe.

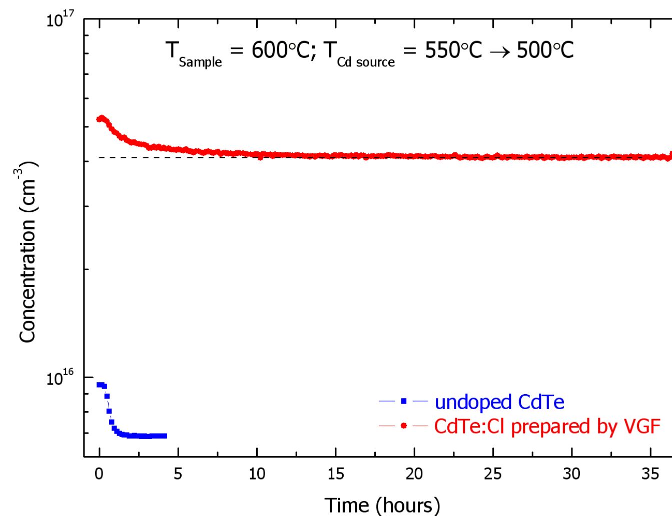

Fig.3.18: Relaxation of the carrier concentration of undoped CdTe and CdTe:Cl prepared by the VGF method measured by "*in-situ*" high-temperature Hall effect measurements under Cd overpressure. In both measurements the sample temperature was kept at 600°C and a step-like change of the Cd source temperature from 550°C to 500°C was performed. The relaxation to a new equilibrium carrier concentration was in CdTe:Cl sample approximately 10-times longer comparing to undoped CdTe.

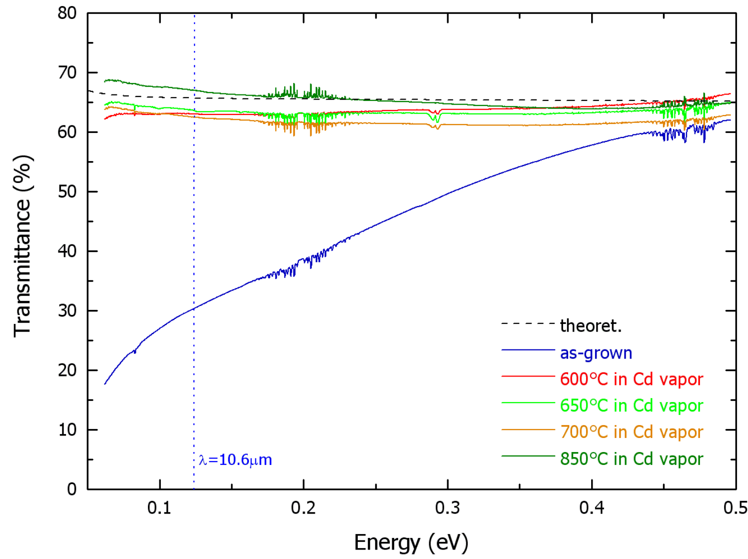

Fig.3.19: IR transmittance spectra of $Cd_{0.96}Zn_{0.04}Te$ substrates before and after annealing in Cd vapor at various temperatures.

In case of $Cd_{0.96}Zn_{0.04}Te$ substrate-grade material, an effect of Cd-rich annealing on the IR transmittance of samples was investigated. It was found that the IR transmittance reached practically maximal theoretical values after the annealing in a Cd atmosphere (Fig.3.19) [55]. On the other hand, properties of detector-grade CdTe:Cl crystals were strongly affected by Cd-rich annealing. Especially, one of the main parameter of the detector-grade material – the resistivity above 10^8Ωcm – was completely changed and low resistivity ($\rho<0.1$Ωcm) of samples was observed after the annealing. Hence, in case of the detector-grade CdTe:Cl, it was necessary to find an additional annealing treatment leading to a restoration of the material resistivity of detectors annealed in a cadmium atmosphere.

3.5. Resistivity restoration of CdTe:Cl crystals

Since Cd-rich annealing of the detector-grade CdTe:Cl led in to a significant decrease of the material resistivity and loss of the detection ability, an additional annealing treatment was necessary for increasing of the resistivity. Therefore, the second annealing treatment under Te overpressure performed with the aim of a restoration of the initial resistivity was investigated [56].

3.5.1. As-grown samples

In this part of the work, two CdTe:Cl crystals with high density of Te inclusions with the size up to 30μm prepared by two different techniques were used. The first crystal was prepared using the VGF method from 6N Cd and Te and 3N $CdCl_2$. The chlorine concentration along the VGF ingot approximately followed the chlorine segregation coefficient in CdTe [18]. Three wafers from different parts of the VGF crystal were sliced. Every wafer contained different chlorine

Tab.3.3: Properties of as-grown samples cut from different CdTe:Cl wafers.

wafer name	[Cl] (cm^{-3})	Resistivity (Ωcm)
VGF-1	3.4×10^{16}	**3.3×10^{5}**
VGF-2	6.9×10^{16}	**7×10^{7}**
VGF-3	2×10^{17}	**2×10^{9}**
THM	2.4×10^{17}	**2×10^{9}**

concentrations and also exhibited different resistivity (see Tab.3.3). From each wafer six samples were cut for resistivity restoration experiments. Generally, it is expected that the wafer resistivity is connected with the chlorine doping level [Cl]. Similar dependence of the material resistivity on [Cl] was found in [39], where CdTe:Cl with $\rho>10^8\Omega$cm was obtained in crystals with [Cl] > 1×10^{17} cm^{-3}. This can be explained based on results of Meyer et al. [57], who showed that the concentration of the dominant acceptor – chlorine A-center V_{Cd}-Cl_{Te} – exceeds in crystals with [Cl] < 1×10^{17} cm^{-3} the concentration of a dominant donor Cl_{Te} and the concentration of both dominant point defects is equal for [Cl] ≈ 1×10^{17} cm^{-3}. The second crystal was prepared commercially by the THM technique. It is expected that the crystal was grown from 7N starting materials. From this crystal only one wafer was available, the parameters of which are also listed in Tab.3.3.

3.5.2. The first annealing step – Annealing in Cd vapor

The aim of the Cd-rich annealing treatment was to eliminate Te inclusions. More detailed description of annealing conditions and their influence on Te inclusions was given in the section 3.4.3. Inclusions in both crystals were successfully eliminated by annealing in a Cd atmosphere, however, an adverse consequence of such a thermal treatment was a significant decrease of the material resistivity to $\rho<0.1\Omega$cm. All samples exhibited n-type conductivity after the annealing. This result can be explained by annihilation of V_{Cd} by in-diffusion of Cd_i into the crystal lattice during Cd-rich annealing, which leads to loss of the compensation and to setting the donor Cl_{Te} as the dominant point defect. Since chlorine atoms are incorporated in the tellurium sublattice and most of diffusion processes proceed in the cadmium sublattice, it is expected that [Cl] in the crystal lattice is affected by annealing in Cd vapor only slightly.

3.5.3. The second annealing step – Re-annealing in Te vapor

The aim of the second annealing step in a Te atmosphere was to increase the material resistivity. The main idea of such a thermal treatment step is showed in Fig.3.20. It is expected that high resistive CdTe:Cl is result of a good compensation between the dominant donor Cl_{Te} and

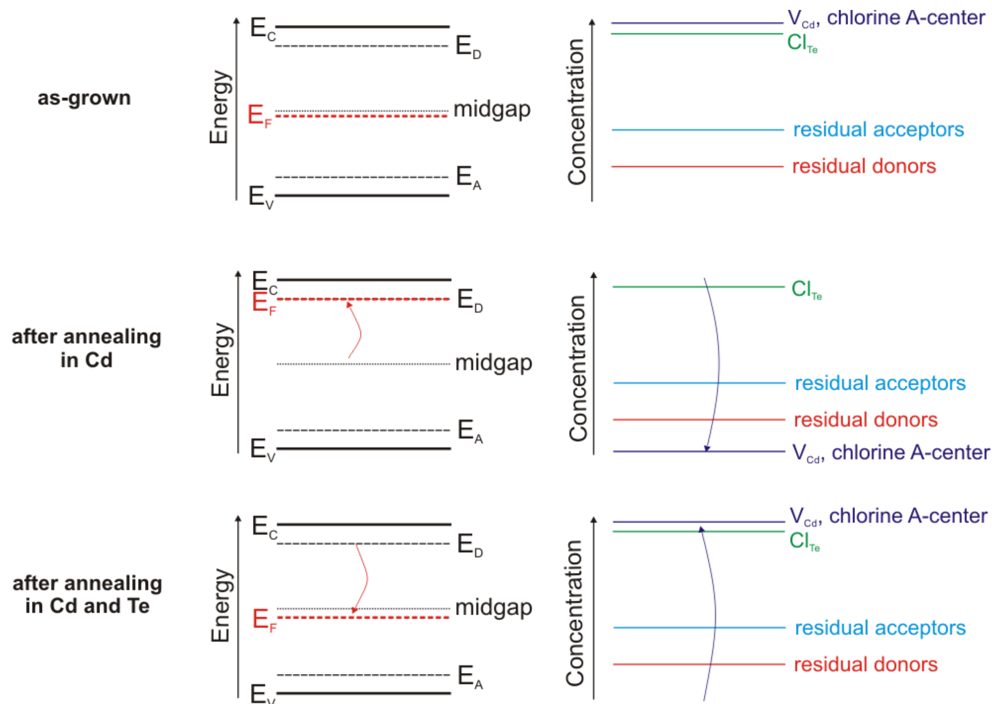

Fig.3.20: Schematic description of the effect of two-step annealing on the concentration of dominant point defects and position of the Fermi energy.

dominant acceptors V_{Cd} and chlorine A-center. If the concentration of both types of defects is close to each other, the Fermi energy is pinned on a deep level close to the midgap and semi-insulating (SI) material is formed. During Cd-rich annealing annihilation of V_{Cd} due to in-diffusion of Cd_i into the crystal lattice occurs and decrease of [V_{Cd}] (and consequently [A-centers]) is observed. Cl_{Te} becomes the dominant point defect and the Fermi energy is pinned on the dominant donor level. Hence, the aim of the second Te-rich annealing is to increase [V_{Cd}] (and consequently also [A-center]) close to [Cl_{Te}] (simultaneously, [Cl_{Te}] decreases due to the formation of a chlorine A-center). This leads to a compensation of dominant donor and acceptor defects and the Fermi energy is pinned again on a deep level close to the midgap, whose origin is unknown.

To find an optimal annealing treatment under Te atmosphere leading to increase of the material resistivity, a systematic investigation of annealing conditions was performed. The resistivity of samples after the second Te-rich annealing is plotted in Fig.3.21. As can be seen, the resistivity of all samples significantly increased after the re-annealing of samples in a Te atmosphere. From three types of VGF samples, the highest resistivity was achieved in VGF-3 samples. Resistivity of VGF-1 and VGF-2 samples after two-step annealing did not reach the initial resistivity and was over one order of magnitude lower. On the other hand, VGF-3 samples exhibited practically identical resistivity $\rho = 2\times10^{9}\,\Omega cm$ before and after two-step annealing. Te-rich annealing of VGF samples at 700°C for 24 hours with the temperature of the Te source in the range of 550-600°C was found to be optimal concerning the annealing time, sample resistivity, sample homogeneity and negligible sample sublimation. The cooling rate after the annealing was kept lower than 1°C/min. for suppression of Te precipitates formation [30]. The size of the created Te precipitates was below the resolution limit of the IR microscopy. Most of samples exhibited the p-type conductivity, only one VGF-3 sample annealed at the lowest Te pressure was n-type (in Fig.3.21 labeled by the black circle).

THM samples were annealed in Te vapor at 700°C at various Te pressures for 24 hours

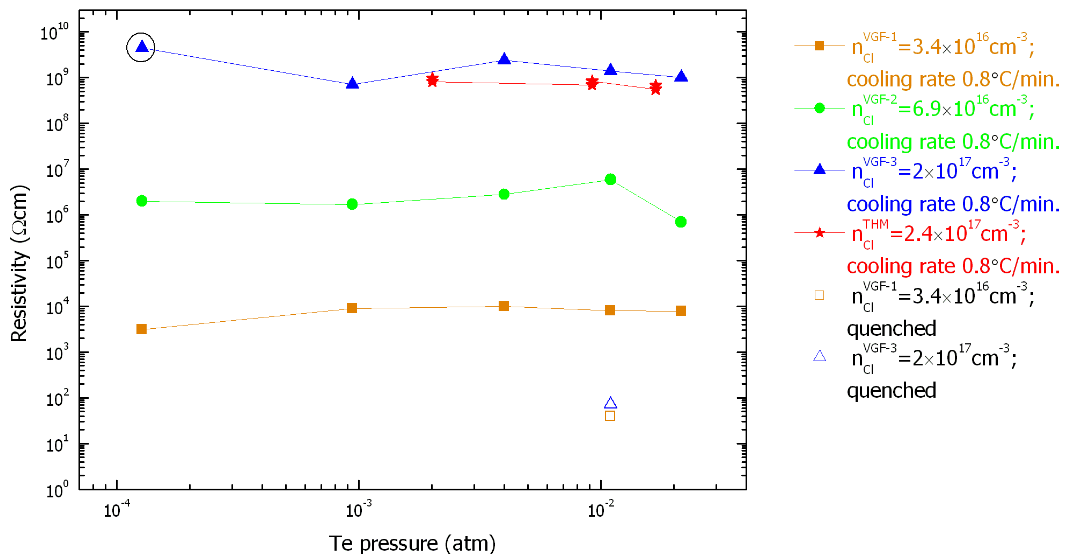

Fig.3.21: The resistivity dependence on Te overpressure after the second annealing step in Te vapor. Every point represents the resistivity of one sample after two-step annealing. Most of the samples were annealed at 700°C for 24 hours. Samples annealed at the lowest Te pressure 1.26×10^{-4}atm were annealed at 600°C for 50 hours. Filled symbols are samples cooled slowly after the second Te-rich annealing. Empty symbols represent samples quenched in the air after the second Te-rich annealing step. Lines are guides for eyes only.

with a cooling rate of 0.8°C/min. After the two-step annealing, no Te precipitates visible by IR microscopy were observed. The final resistivity of samples did not reach the initial resistivity of as-grown material and was in the range of ρ=5-9×10^{8}Ωcm depending on the applied Te overpressure. The highest resistivity was observed after the annealing at 700/540°C for 24 hours. All annealed samples exhibited the p-type conductivity. To prove the reproducibility of the two-step annealing treatment, two THM samples were always annealed together in the same Te-rich annealing run. After the annealing, their mutual difference of the resistivity was below 30%.

VGF-1, VGF-2 and THM samples after two-step annealing exhibited lower resistivity than before the annealing treatment. The reason for this effect remains unclear. It is difficult to decide, whether it was caused by a contamination of the material during annealing process or whether this phenomenon rather had a physical origin.

From results, plotted in Fig.3.21, can be concluded that the final resistivity of samples was determined mainly by the chlorine doping concentration and was practically independent of the applied Te pressure P_{Te_2} during the Te-rich re-annealing. Observed weak pressure dependence can be explained by two models:

MODEL I: It is expected that the dynamic processes concern mainly the Cd sublattice in CdTe, where the volatile Cd may be easily removed from the lattice and the formation energy of the relevant point defects is low [58]. The defect density at Cd sublattice, Cd vacancy, is determined by the Cd pressure P_{Cd} linked to P_{Te_2} via the reaction constant $K_i(T)$ [59]

$$P_{Cd} = K_i(T) / \sqrt{P_{Te_2}} \, . \tag{3.1}$$

In an ideal case of an isothermal annealing at thermal equilibrium the sample temperature T_{sample} should be used for the calculation of the reaction constant $K_i(T)$. At the two-zone furnace annealing, however, the component pressures are ruled by the cold zone temperature $T_{component}$ where Te is disposed. Consequently, P_{Cd} in a two-zone furnace at Te annealing can be significantly reduced and, moreover, the cooling/heating of the Te source does not entail the usually expected increase/decrease of P_{Cd} according eq. (3.1), even an opposite dependence can be obtained. The value of P_{Cd} becomes more doubtful, if pure Te in the cold zone is used. In that case P_{Cd} near the sample is set by highly unspecific dynamic process of the evaporation of Cd from the sample, Cd flux toward the cold zone and dissolution in Te. Such methodological shortcomings of the two-zone annealing can result in the conductivity apparently independent on Te pressure. Final properties of the material depend only slightly on applied Te pressure at Te-rich annealing and the process resembles rather the annealing in vacuum than the annealing at defined pressures.

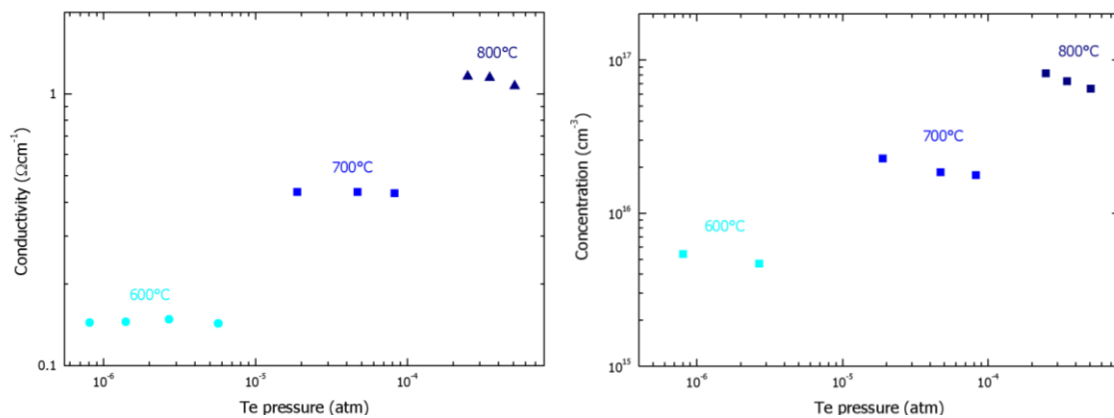

Fig.3.22: "*In-situ*" high-temperature conductivity and carrier concentration of VGF-3 sample measured at temperatures 600, 700 and 800°C at various Te pressures.

MODEL II: The second explanation can be based on a compensation process during Te-rich annealing concerning shallow donors Cl_{Te} and acceptors V_{Cd} and Cl_{Te}-V_{Cd}. During the Te-rich annealing [V_{Cd}] is set at elevated value. During slow cooling after the annealing, Cd vacancies together with Cl_{Te} form chlorine A-centers whose concentration is determined by [Cl]. With decreasing temperature, V_{Cd} start to precipitate or vanish on extended defects and [V_{Cd}] decreases. Therefore, the concentration of acceptors is given mainly by chlorine A-centers and depends more on the chlorine doping level than on the applied Te pressure during the Te-rich annealing.

The first model can be supported by results from "*in-situ*" high-temperature Hall effect measurements of VGF-3 sample performed under Te overpressure (Fig.3.22), where a relatively weak pressure dependence of the conductivity and carrier concentration was observed at 600, 700 and 800°C. Contrary to this, to prove the second suggested model, one VGF-1 and one VGF-3 sample was cooled down rapidly in the air after the second Te-rich annealing step. Both samples, in Fig.3.21 plotted as empty symbols, exhibited low resistivity ($\rho_{quenched}^{VGF-1} = 40\Omega cm$ and $\rho_{quenched}^{VGF-3} = 72\Omega cm$) and the p-type conductivity. We suppose that during the fast cooling V_{Cd} mainly remain "frozen" in the crystal lattice or start to create precipitates and formation of chlorine A-centers is not dominant. This leads to an increased concentration of acceptor defects (mainly [V_{Cd}]) compared to [Cl_{Te}] and low-resistive p-type material is obtained. This experiment supports the idea that the compensation occurs during cooling of the material and is based mainly on the compensation of the donor Cl_{Te} and acceptor chlorine A-center. To conclude, both models seem to have an experimental rationale, however, it is difficult to decide, which model explains the weak pressure dependence of the resistivity after two-step annealing more accurately.

High-resistive CdTe:Cl usually exhibits the p-type conductivity [56] compared to CdTe:In with typical n-type conductivity [60]. This phenomenon can be explained by a compensation model concerning dominant point defects – doping donors (In_{Cd} or Cl_{Te}) and acceptors (V_{Cd}; In_{Cd}-V_{Cd} or Cl_{Te}-V_{Cd}) [61]. Within this model, the position of the Fermi energy E_F is given by the relation:

$$E_F = \frac{1}{2}\left(f(T,p) + E_{V_{Cd}} + E_A + E_i^{V_{Cd}} + E_i^A\right) \tag{3.2}$$

where $f(T,p)$ is a function depending on temperature and pressure of the system; $E_{V_{Cd}}$ and E_A is the formation energy of cadmium vacancy and A-center, respectively; and $E_i^{V_{Cd}}$ and E_i^A is the ionization energy of V_{Cd} and A-center, respectively. The parameters E_A and E_i^A depend on the type of an A-center. For crystals doped by indium $E_A = -0.3eV$ and $E_i^A = 140meV$ [10] can be used. In chlorine doped crystals $E_A = -0.5eV$ and $E_i^A = 120meV$ [10]. Based on equation (3.2), the position of the Fermi level in CdTe:Cl is shifted approximately 110meV closer to the valence band in comparison with CdTe:In crystals. Therefore, high-resistive chlorine doped CdTe exhibits usually the p-type conductivity and high-resistive CdTe:In is typically n-type.

From the obtained results, it can be concluded that the chlorine doping level is the most important parameter determining whether CdTe:Cl crystal is high-resistive ($\rho > 10^8 \Omega cm$) after two-step annealing or not. This effect can be explained by a compensation model based on the compensation of the donor Cl_{Te} and acceptor chlorine A-center. Our experiments and also results of Ohmori et al. [39] and Meyer et al. [57] lead to the conclusion that a good compensation occurs in the CdTe:Cl material with chlorine doping level above $10^{17} cm^{-3}$.

3.5.4. Photoluminescence spectra

PL spectra of VGF-3 (Fig.3.23) and THM (Fig.3.24) samples before and after two-step annealing were measured in the energy range of 0.5-1.62eV. Two significant differences were observed in annealed samples. The first one was an increase of the peak intensity at 1.576eV; the second effect was a creation of a non-standard emission at 1.26eV. In earlier PL studies [62],[63], a similar emission about 1.27eV was observed in Au doped CdTe. In Hamann's work [62], a broad

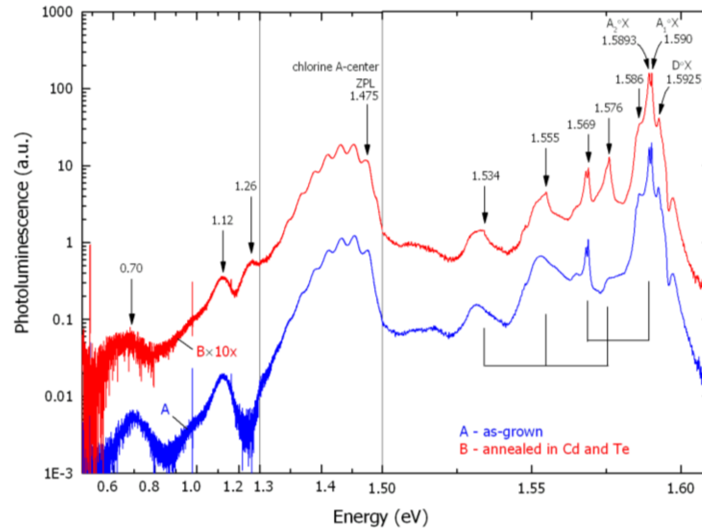

Fig.3.23: PL spectra of VGF-3 sample before and after two-step annealing measured at 4.2K.

peak at 1.27eV was found. Molva et al.[63] observed a structure with phonon replicas at about 1.27eV, which was attributed to a donor-acceptor pair (DAP) formed by the acceptor Au_{Cd} and an unknown donor. The peak at 1.576eV was in both works connected with the shallow acceptor Au_{Cd}. In this work, both appeared emissions were observed in samples without any Au doping or surface deposition during and between annealing steps, and a connection of both emissions with Au_{Cd} is questionable.

The same emission at 1.26eV with phonon replicas structure was also observed in In-doped CdTe crystals annealed in Te vapor [64]. Since the emission in CdTe:Cl and CdTe:In is located at the same position, the origin of the emission is not connected with the type of doping donor Cl or In (see Fig.3.25). The character of the emission at 1.26eV was investigated on samples annealed

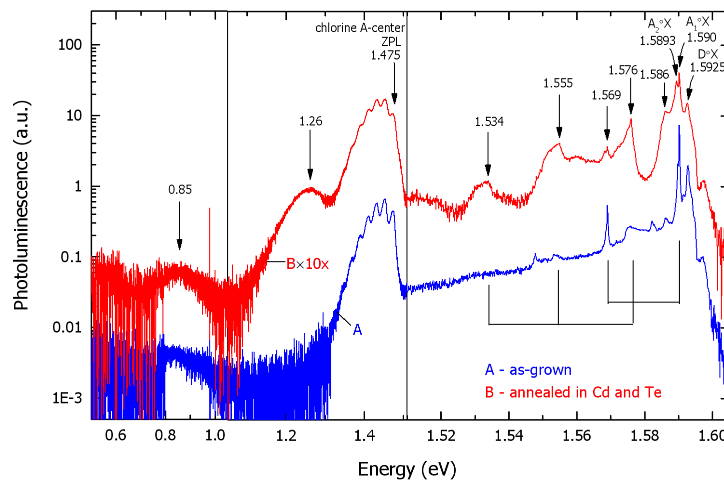

Fig.3.24: PL spectra of THM sample before and after two-step annealing measured at 4.2K.

under various Te pressure to study, whether the emission is formed by native defects. However, no dependence on the applied Te pressure was found. To conclude, the emission at 1.26eV with phonon replica structure can be attributed to a DAP defect with unclear composition. The origin of the peak at 1.576eV can be assigned to an unknown bound exciton or to the phonon replica of free exciton FE-LO usually observed at 1.575eV.

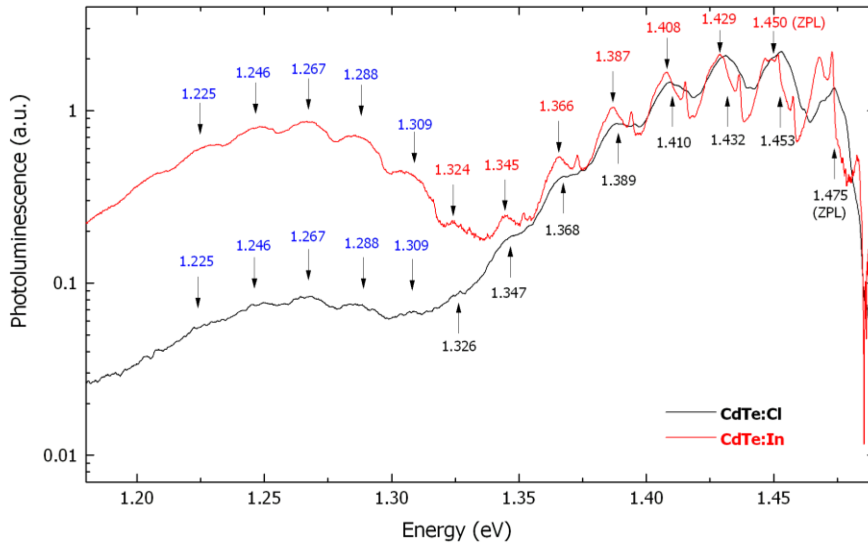

Fig.3.25: Comparison of the A-center and DAP emissions in CdTe:In annealed in Te vapor and CdTe:Cl after two-step annealing. Positions of peaks of indium and chlorine A-centers are different by 2meV in agreement with their different formation energies. Since the positions of DAP peaks are identical for both types of crystals (blue marks), it can be concluded that the origin of a DAP is not connected with the type of doping atoms (In or Cl).

3.5.5. Gamma-ray and Alpha-particle spectra

Gamma-ray and alpha-particle spectroscopy of VGF-3 and THM crystals were performed before and after two-step annealing treatment. In γ-ray spectra of the VGF-3 crystal, the main photopeak was shifted to lower energies and the photopeak height decreased (Fig.3.26). Observed high noise at low energies was caused by a significant surface leakage current. The $(\mu\tau)_e$ remained

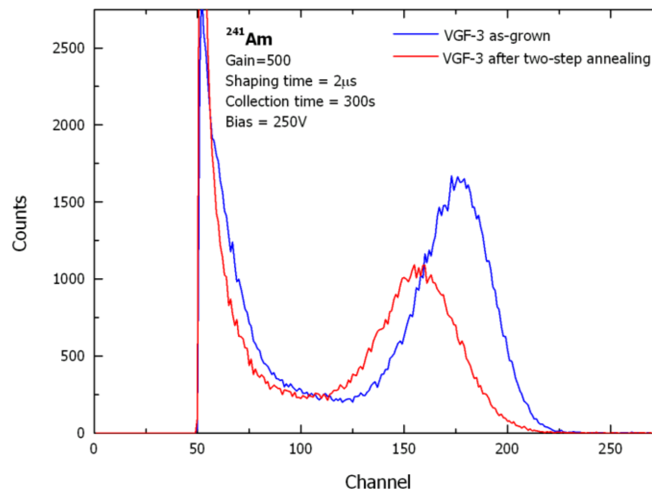

Fig.3.26: Gamma-ray spectra of VGF-3 sample (a) before and (b) after two-step annealing.

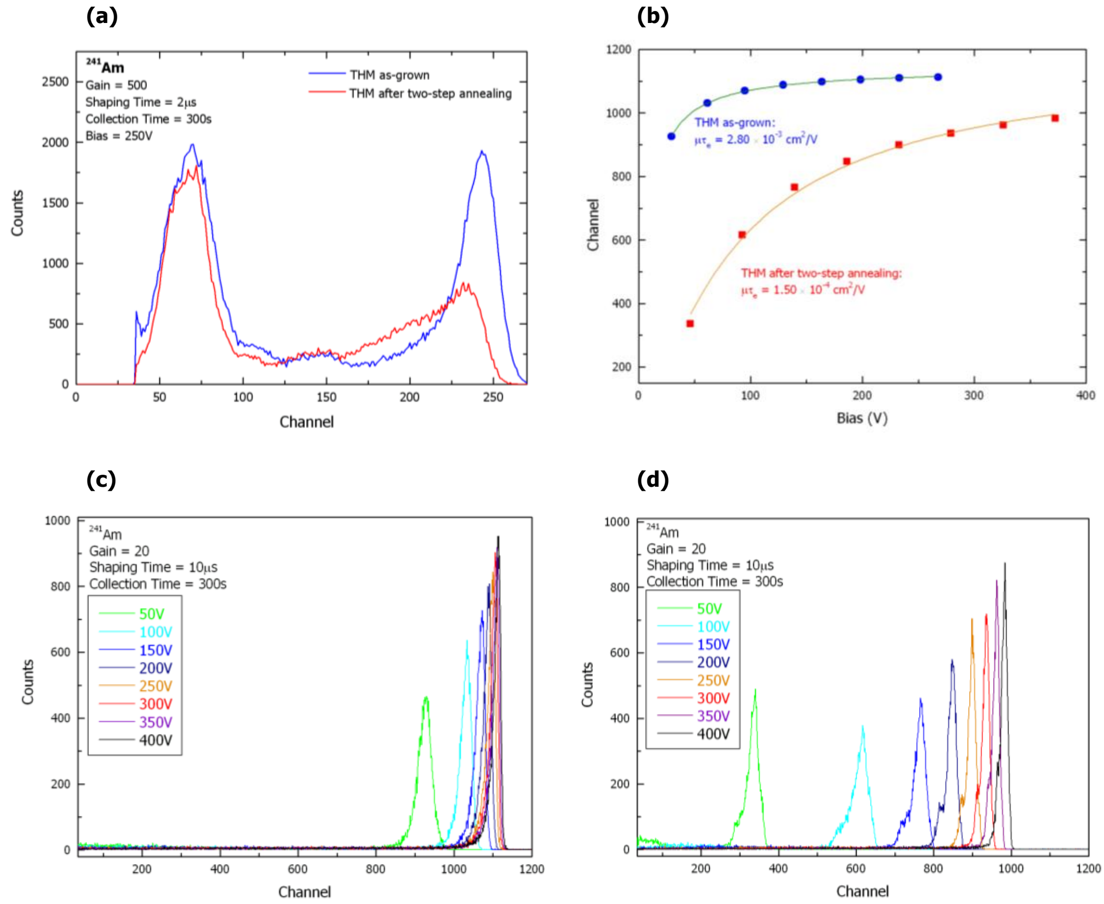

Fig.3.27: (a) – gamma-ray spectra of THM sample before and after two-step annealing. (b) – evaluation of $\mu\tau_e$-product based on the Hecht analysis. Alpha-particle spectra of THM sample (c) before and (d) after two-step annealing.

practically unchanged at a level of 2.7×10^{-4}cm^2/V (see Tab.3.4). The main photopeak in γ-ray spectra of annealed THM samples was shifted to lower energies, the photopeak height decreased and the FWHM increased (Fig.3.27a). Moreover, a significant drop of the $(\mu\tau)_e$ from 2.8×10^{-3}cm^2/V to 1.5×10^{-4}cm^2/V was observed (Fig.3.27b). In both crystals two effects could affect the detection ability after application of a two-step annealing: a) redistribution of impurities from Te inclusions during Cd-rich annealing and b) contamination of the material during the annealing treatment. Both effects could lead to incorporation of impurities into the crystal lattice and formation of an unknown deep level, which is not possible to seen in PL spectra and which markedly decreases the CCE. It is expected that the THM wafer was prepared from purer (7N) starting materials comparing to the VGF crystal (6N starting materials). Hence, the described effects had probably bigger influence on the detection ability of THM samples than of VGF-3 samples. Moreover, it is expected that the CCE was not affected by the defect with the emission line at 1.26eV found by PL, because this defect assigned to DAP is attributed to too shallow (acceptor and donor) defects.

Tab.3.4: The resistivity and µτ-product of electrons of as-grown and annealed samples.

sample	Resistivity (Ωcm) as-grown	$\mu\tau_e$ (cm^2/V) as-grown	Resistivity (Ωcm) annealed	$\mu\tau_e$ (cm^2/V) annealed
VGF-3	2×10^9	2.8×10^{-4}	2×10^9	2.7×10^{-4}
THM	2×10^9	2.8×10^{-3}	8×10^8	1.5×10^{-4}

3.6. Summary

This part of the work was focused on characterization and elimination of both types of inclusions present in CdTe materials. It was found out that star-shaped inclusions are formed from a pure cadmium core surrounded probably by Cd-rich precipitates situated at dislocation loops around the core. On the other hand, triangle-shaped inclusions were completely filled by pure tellurium and lot of inclusions contained also a void inside. Model of inclusion creation was suggested for both types of inclusions. From experiments can be concluded that the size of Cd inclusions can be reduced by an annealing in Te vapor at temperature above 700°C. However, the core of Cd inclusion cannot be eliminated by any type of investigated annealing treatments. Moreover, in the substrate-grade $Cd_{0.96}Zn_{0.04}Te$ material, Te-rich annealing leads to marked decrease of the IR transmittance at about λ=10μm and re-annealing of the material in Cd vapor is necessary for the high infrared transmittance restoration. Detector-grade CdTe usually doesn't contain this type of inclusions and hence this type of material was not investigated in detail. Contrary to Cd inclusions, Te inclusions can be in most cases successfully eliminated by annealing in a Cd atmosphere at temperatures above 650°C. Such an annealing treatment leads to an increase of the IR transmittance of a substrate-grade material close to maximal values. In CdTe:Cl detector-grade material, Cd-rich annealing leads to a loss of the high-resistivity and detection ability. Hence re-annealing of the material under Te overpressure is necessary for the resistivity restoration. Slow post-anneal cooling (<1°C/min.) was applied for suppression of Te precipitates formation. It was found that the final resistivity depends mainly on the chlorine doping level and the highest resistivity was observed in crystals with $n_{Cl}>10^{17}cm^{-3}$. Moreover, a weak dependence of the resistivity on applied Te pressure during the second re-annealing step was observed. Two models were proposed as an explanation of this behavior and discussed. In addition, two-step annealing led to an appearance of two new emissions in PL spectra and also to decrease of the detection ability of commercially prepared detectors.

4. High-temperature transport properties of CdTe

4.1. Introduction

Properties of the grown crystal strongly depend on the crystallization process and following cooling of the crystal to the room temperature. Both growing parameters (crystallization conditions, post-growth cooling rate) affect the deviation of stoichiometry and distribution of defects in the solidified crystal lattice. Electrical measurements (electrical conductivity/resistivity; carrier concentration and mobility) are very sensitive to crystal properties at atomic level. Hence, electrical measurements performed directly at high temperature can provide lot of information about dominant charged point defects, or diffusion processes and rates. During "*in-situ*" Hall effect measurements (transport measurements performed directly at high temperatures) the CdTe sample is held at constant temperature and surrounding vapor pressure is defined by cadmium or tellurium temperature. If a pressure step-like change is performed, electrical properties start to relax to new equilibrium values. Since the chemical diffusion is faster at higher temperatures, also the relaxation of electrical properties after the pressure step-like change is faster at higher temperature of the sample. The relaxation exhibits an exponential character and diffusion coefficient can be determined by fitting of the relaxation decay. After relaxation, all electrical properties reach new values given by a new redistribution of point defects in the crystal lattice. Such measurements can be performed at various temperatures in the range of 450-1000°C. Analysis of pressure dependence of electrical entities at various temperatures can provide useful information about the point defect distribution at high temperatures.

Electrical properties of CdTe at elevated temperature were measured for the first time by de Nobel [1]. He measured electrical conductivity of CdTe:In and CdTe:Cu crystals annealed at high temperatures (700, 800 and 900°C) at various Cd pressures followed by their quenching to room temperature after the annealing. He observed an increase of the electrical conductivity with higher applied Cd pressure during the annealing resulting in a dependence of $\sigma \sim P_{Cd}^{1/2}$. He attributed this behavior to native singly ionized donor defects (Cd_i^+ or V_{Te}^+). Near tellurium saturation (low P_{Cd}) the samples exhibited relatively strong dependence on applied pressure explained by the presence of a dominant native acceptor V_{Cd}. The first real "*in-situ*" Hall effect measurements were performed by Whelan and Shaw [65]. Contrary to de Nobel, their experiments on undoped CdTe led to pressure dependence of $\sigma \sim P_{Cd}^{1/3}$ resulting in a model, in which native doubly ionized donor defects (Cd_i^{++} or V_{Te}^{++}) are dominant point defects at high temperatures (490-950°C) near the cadmium saturation. Similar results were also observed by Zanio [31] and Smith [66]. Moreover, Smith [66] found relatively weak pressure dependence near to the tellurium saturation. He explained this behavior by the presence of an acceptor impurity rather than by the presence of a native acceptor defect. Zanio [31] evaluated for the first time the diffusion coefficient from "*in-situ*" Hall effect measurements based on the relaxation of the electrical conductivity after a step-like change of pressure: $\tilde{D}_{CdTe} = 4\exp(-1.15 \pm 0.1 eV/kT) cm^2/s$. Direct comparison of quenching experiments and "*in-situ*" measurements was performed by Selim et al. [67]. His results were in a good agreement with quenching experiments of de Nobel [1] and "*in-situ*" measurements of Whelan and Shaw [65], Zanio [31] and Smith [66]. The difference in results between quenching and "*in-situ*" experiments was attributed to precipitation of native defects and dopants occurring during fast cooling of the crystal after the annealing. Based on mentioned works and review studies of Chern [68,69,70],

Berding [58], Grill [21] and Fochuk [71]; a basic behavior of the point defect structure at high temperatures (700-900°C) can be summarized:

<u>undoped CdTe:</u> high P_{Cd} — Cd_i^{++} and partly V_{Te}^{++} dominate, typical slope $\sigma \sim P_{Cd}^{1/3}$

low P_{Cd} (high P_{Te_2}) — V_{Cd}^{--}, V_{Cd}^{-}, Te_{Cd}^{--}, Te_{Cd}^{-} and partly Te_i^{-} dominate

<u>CdTe doped by a donor:</u> high P_{Cd} — donor dopant D^+ and Cd_i^{++} dominate

low P_{Cd} (high P_{Te_2}) — A-center $\left(V_{Cd}^{--} - D^+\right)^-$ and singly and doubly ionized acceptors V_{Cd} and Te_{Cd} dominate

As was mentioned earlier, the situation in quenched samples is more complicated due to precipitation of dominant point defects during a fast cooling.

This work will be aimed at measuring of "*in-situ*" high-temperature electrical properties in the temperature range of 450-1000°C under both cadmium and tellurium overpressure. The goal of this work is to perform detailed measurements at low temperature (450-600°C) under the Cd pressure and detailed measurements under Te overpressure, where only few data have been published. Moreover, a non-standard double relaxation after a specific step-like pressure change under Cd atmosphere will be investigated. And finally, a simulation of the second Te-rich annealing step of the two-step annealing will be performed by "*in-situ*" measurements.

4.2. "*In-situ*" high-temperature Hall effect measurements of undoped CdTe, CdTe:In and CdTe:Cl

Pressure dependence of the conductivity and carrier concentration of undoped CdTe and CdTe:In with $n_{In} = 5\times10^{15}\text{cm}^{-3}$ [60] is shown in Fig.4.1 and Fig.4.2, where data from both crystals are not distinguished because they are very similar. With the aim of plotting data obtained at Cd or Te pressures into one figure, Te pressure was transferred into the corresponding Cd pressure (P_{Cd}) according to the CdTe partial pressure equation

$$P_{Cd}\sqrt{P_{Te_2}} = \exp\left(\Delta G_f^0 / k_B T\right) \qquad (4.1)$$

where $\Delta G_f^0 = 287.190 + 188.0290T\left(J/mol\right)$ [59] is the Gibbs formation energy and k_B is the Boltzmann constant. Te-rich data are divided from Cd-rich data by a dotted line in both figures. Measured data (red and blue points) are shown together with older data published in [72] (grey points). Similar data from both crystals can be explained by low In concentration in CdTe:In, which is comparable with the concentration of other unintentionally doped impurities. Measured data (red and blue points) in the Te-rich side, which agree with the defect model [72] better than old (grey) data, were obtained in the temperature interval 600-900°C. The results of the simulations within the defect model [72] support the model of native defect structure of undoped Te-rich CdTe characterized by dominating acceptor V_{Cd} and possibly partly compensated by a donor Te_{Cd}.

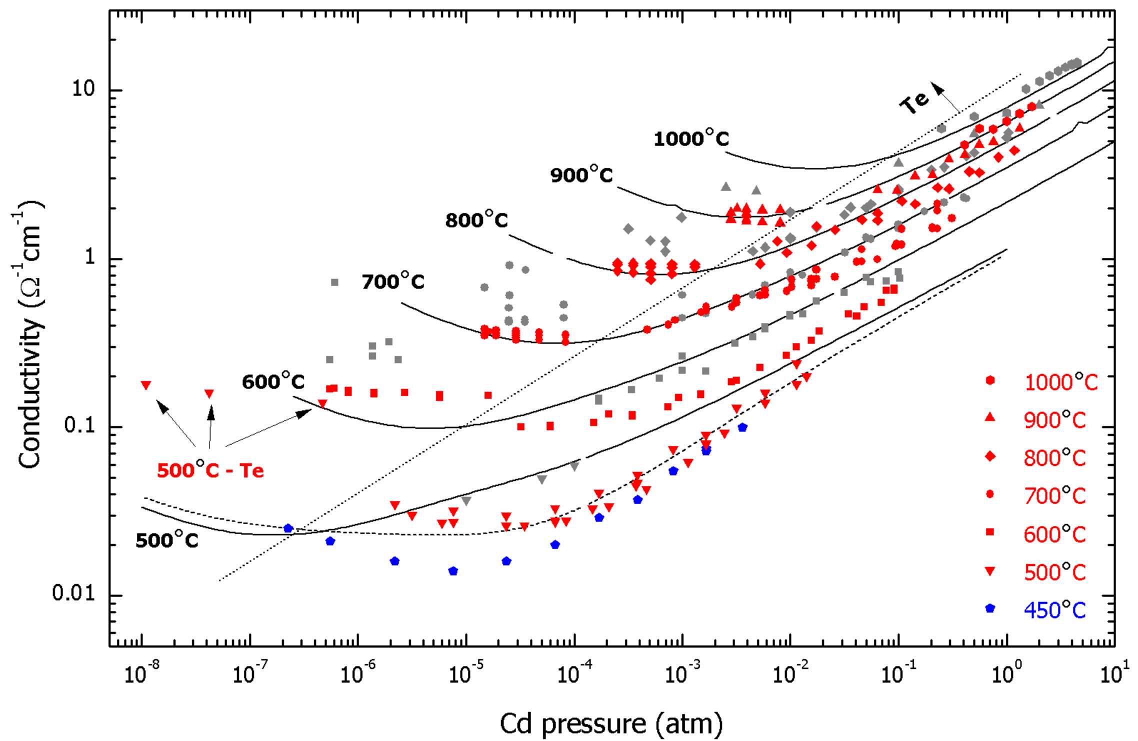

Fig.4.1: "*In-situ*" high-temperature Hall effect measurements of conductivity at various Cd or Te overpressures [60]. Grey points represent data published in [72], red and blue points represent new data. Solid lines are results of the defect structure calculation of undoped CdTe and the dashed line is a fit at 500°C with additional acceptor level with the density of 4×10^{15}cm^{-3}.

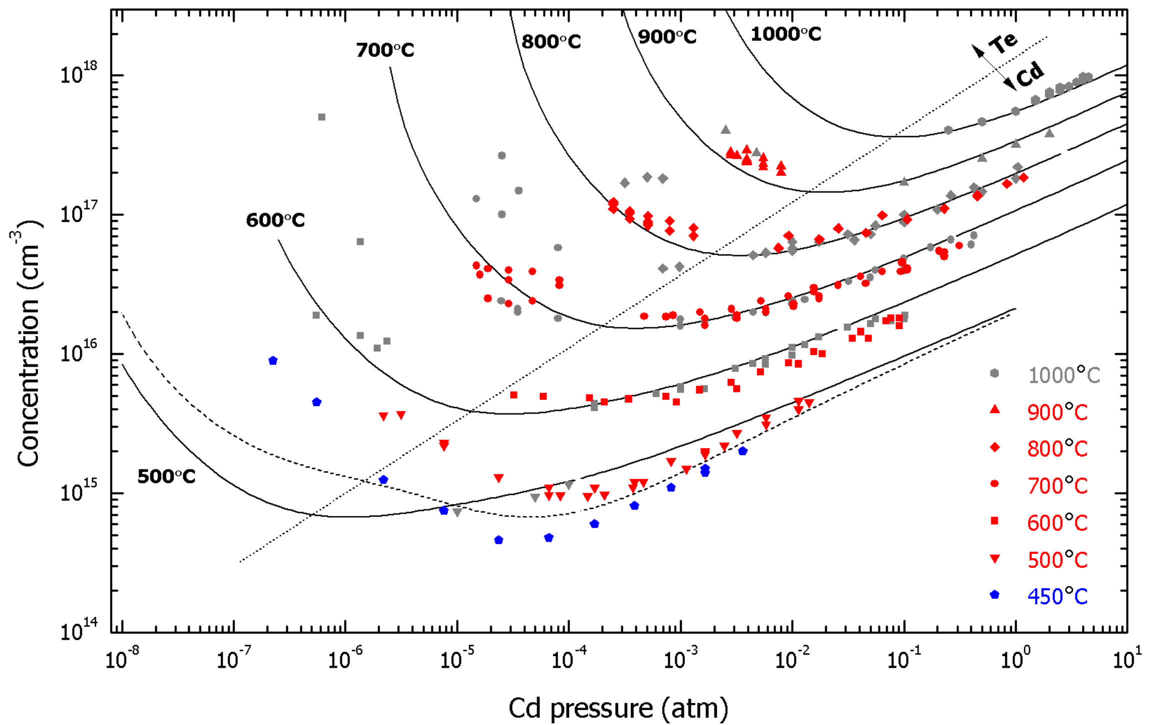

Fig.4.2: "*In-situ*" high-temperature Hall effect measurements of carrier concentration at various Cd or Te overpressures [60]. Grey points are data published in [72], red and blue points represent new data. Solid lines represent the results of the defect structure calculation of undoped CdTe and the dashed line is a fit at 500°C with additional acceptor level with the density of 4×10^{15}cm^{-3}.

A systematic slight shift was observed at low temperature (450-600°C) under Cd pressure comparing to old data [72] due to the presence of an unknown acceptor level. The data at 500°C were fitted separately and a dominant acceptor with a concentration of 4×10^{15}cm^{-3} was identified. The Clausius-Clapeyron equation and thermodynamic data [73] were used to extrapolate known saturated vapor pressure ($P_{Cd\text{-}sat}$) [22] below the melting point of Cd at 321°C, where no experimental data have been published yet. The new temperature dependence of $P_{Cd\text{-}sat}$ is expressed as

$$T < 321°C \qquad P_{Cd-sat}(atm) = 10^{5.6626-5640/T} \tag{4.2}$$

$$T > 321°C \qquad P_{Cd-sat}(atm) = 10^{5.119-5317/T}\,. \tag{4.3}$$

As can be seen from Figs. 4.1 and 4.2, the present defect model doesn't describe well all experimental data. The pressure independent conductivity at 500°C and 600°C observed in the Te-rich side is not in agreement with the model. This effect could be explained by some acceptor contamination deduced from the Cd-rich measurements at 450°C and 500°C. In case of measurement at Cd pressure the shallow acceptor level with density 4×10^{15}cm^{-3} improves the fit above P_{Cd} ~ 10^{-4}atm at 500°C plotted as the dashed line. The results at P_{Cd} ~ 10^{-4}atm, however, strongly deviate from the theory and no improvement could be obtained within the present defect model. At higher temperatures (above 600°C) reduced slopes point to unstable or amphoteric-like acceptors (e.g., phosphorus) being active at maximum Cd pressure. Since similar data were observed for undoped CdTe and CdTe:In (n_{In}=5×10^{15}cm^{-3}), possible acceptor contamination during the sample preparation should be also taken into account. Based on chemical analysis of the tungsten wire used for the contact preparation, potassium can diffuse from wires during the measurements and contaminate the sample.

Similar high-temperature "*in-situ*" transport measurements were also performed on CdTe:Cl crystals with doping levels n_{Cl} = 3.4×10^{16}cm^{-3} and n_{Cl} = 2×10^{17}cm^{-3}. The pressure

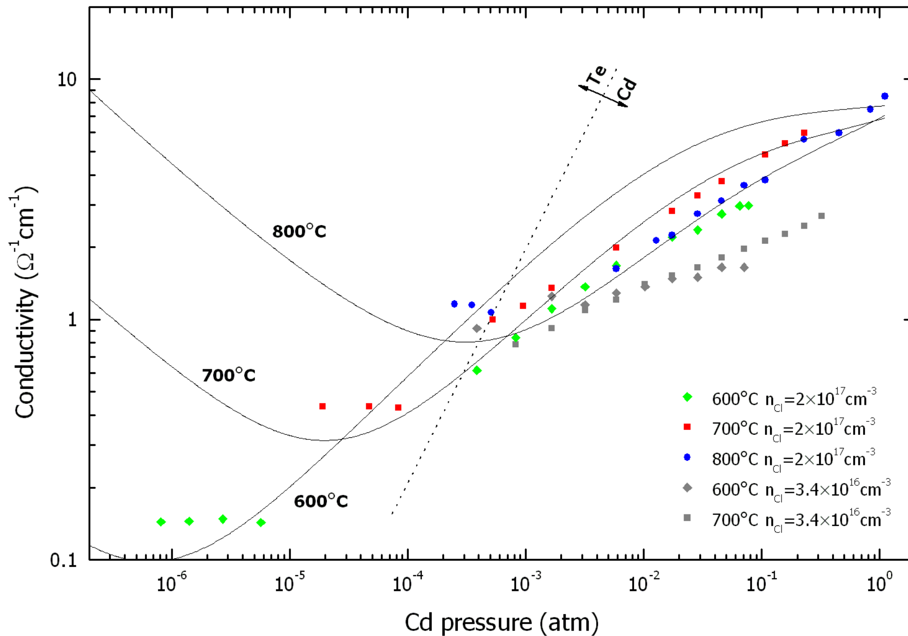

Fig.4.3: "*In-situ*" high-temperature Hall effect measurements of the conductivity at various Cd or Te overpressures of CdTe:Cl with two different chlorine doping levels. Solid lines represent the defect structure calculation of CdTe:Cl with [Cl]=2×10^{17}cm^{-3}.

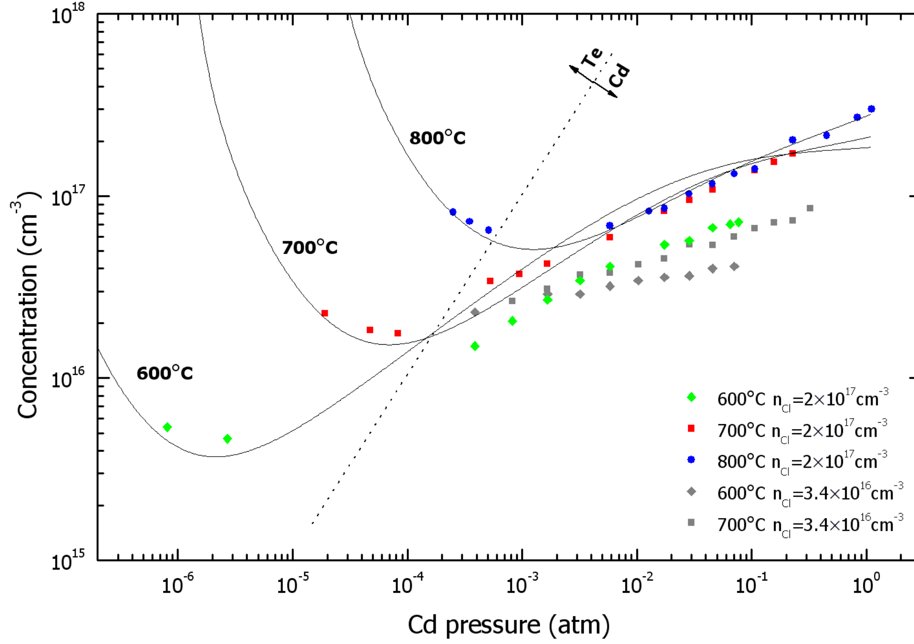

Fig.4.4: "*In-situ*" high-temperature Hall effect measurements of the carrier concentration at various Cd or Te overpressures of CdTe:Cl with two different chlorine doping levels. Solid lines represent the defect structure calculation of CdTe:Cl with [Cl]=$2\times10^{17}cm^{-3}$.

dependencies of the electrical conductivity and carrier concentration are plotted in Figs.4.3 and 4.4, respectively. Measured data of samples with n_{Cl} = $2\times10^{17}cm^{-3}$ (green, red and blue points) are plotted together with the defect model proposed in [72] for CdTe:Cl crystals (solid lines). A deviation of the conductivity and carrier concentration from the theoretical calculations at 600°C at the Cd-rich side was found. This can be explained by presence of an acceptor impurity with the concentration of $4\times10^{16}cm^{-3}$ (probably acceptor-like Cu_{Cd} from only 3N purity $ClCd_2$ starting materials) or by a more complicated defect structure, which is not involved in the defect structure model [72]. Data from samples with n_{Cl} = $3.4\times10^{16}cm^{-3}$ are plotted as grey symbols and are not fitted by the defect structure calculations.

The defect model proposed by [72] results in a very similar defect structure for undoped CdTe and CdTe:In with [In]=$5\times10^{15}cm^{-3}$. Slightly different parameters are used for fitting of CdTe:Cl with [Cl]= $2\times10^{17}cm^{-3}$ (see Tab.4.1). In case of CdTe:In crystals, [In]=$5\times10^{15}cm^{-3}$ was used. In addition, configuration degeneracy factor of an indium A-center is $g_A^{In}=12$ and the

Tab.4.1: Parameters used in the defect model [72]. E_g is the temperature dependent energy bandgap from [1]. Two energies for Cd_i correspond to the two tetrahedral interstitial sites.

defect	Formation energy (eV)	First ionization energy (eV)	Degeneracy factor g_1/g_0	Second ionization energy (eV)	Degeneracy factor g_2/g_0
Cd_i	0.90; 1.10	0; $0.16E_g$	2	$0.17E_g$; $0.27E_g$	1
V_{Cd}	3.84	$0.12E_g$	2	$0.3E_g$	1/3
In_{Cd}	-	0.014	-	-	-
In_{Cd}-V_{Cd}	-0.3	0.12	12	-	-
Cl_{Te}	-	0.014	-	-	-
Cl_{Te}-V_{Cd}	-0.5	0.14	4	-	-

formation energy is $E_A^{In} = -0.3eV$. On the other hand, [Cl]= $2\times10^{17}cm^{-3}$ was used to fit the data obtained from CdTe:Cl crystals. Moreover, $g_A^{Cl} = 4$ and $E_A^{Cl} = -0.5eV$ for CdTe:Cl was used.

4.3. Non-standard double relaxation

Typical "*in-situ*" high-temperature Hall effect measurements are performed in such conditions that the sample is kept at constant temperature and the partial pressure is changed by a step-like change. After this change, measured conductivity or carrier concentration relaxes to a new equilibrium value. An example of such a relaxation is plotted in Fig.4.5. Theoretically, the relaxation time for pressure step-up-change and for identical pressure step-down-change should be the same. In reality, however, the pressure step-change under Cd pressure to lower P_{Cd} exhibits slower relaxation comparing to the same pressure step-change to higher P_{Cd}. This effect was observed also in [69,70] and [32]. If the pressure step-change is large enough, one can observe even a non-standard double relaxation behavior after the pressure step-change to lower P_{Cd} (for the first time seen in [74]). This effect was investigated in detail on two different CdTe:Cl crystals with $n_{Cl} \approx 2\times10^{17}cm^{-3}$. In both crystals, observed relaxations were very similar. Double relaxation phenomenon was investigated in dependence of various types of the pressure step-changes (see Figs.4.6,4.7,4.8 and 4.9). At first, step-like pressure changes from high P_{Cd} to different lower P_{Cd} were investigated (Fig.4.6). It can be seen in Fig.4.6a, that the conductivity relaxes to the first metastable state and after some time relaxes again to the final equilibrium state. This metastable state extends with higher pressure change. From Fig.4.6b can be deduced that the relaxation behavior of conductivity in Fig.4.6a is given practically only by relaxation of the carrier concentration and is not affected by a relaxation of the mobility. Moreover, it should be noted that the double relaxation was observed in cases, when the pressure step passed through the stoichiometric line in the *P-T* phase diagram (see arrows in Fig.4.6c) from the Cd-rich to Te-rich side of the crystal. Fig.4.7 shows the pressure step-like changes from different higher P_{Cd} to the same lower P_{Cd}. Similarly as in the previous case, the time of the metastable state was increasing with increasing of the pressure step-change. It was also found out that the double relaxation doesn't depend on the time spent on the higher P_{Cd} (Fig.4.8). It means that the properties of the double relaxation don't depend on the previous history of the thermal treatment. Finally, an influence of pressure step-like changes by a constant pressure on the double relaxation phenomenon was studied

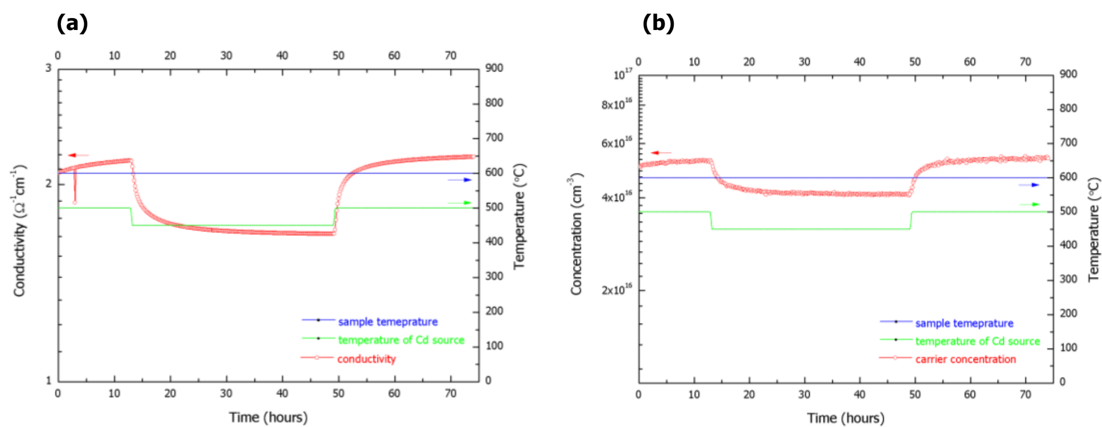

Fig.4.5: Relaxation of (a) the conductivity and (b) carrier concentration in CdTe:Cl after pressure-down-step and pressure-up-step. The relaxation time after both pressure step-changes is practically identical.

(Fig.4.9). From Fig.4.9 can be seen that the metastable state survives longer, when the pressure step-like change is performed at lower P_{Cd}. From obtained results can be concluded that the double relaxation takes longer time if the pressure step-change to lower P_{Cd} is larger, is independent of the previous annealing history and is also more marked at lower cadmium pressures. In earlier works [32,70] the slower relaxation after a step-change to lower P_{Cd} comparing to relaxation to higher P_{Cd} was attributed to temporal precipitation of point defects during the relaxation after the pressure step-change to lower P_{Cd}. The double relaxation investigated in detail in this chapter can be also attributed to a precipitation of point defects during the step-like change of pressure from the Cd-rich crystal to Te-rich crystal enrichment. However, proposed interpretation has not been supported by any theoretical calculations yet.

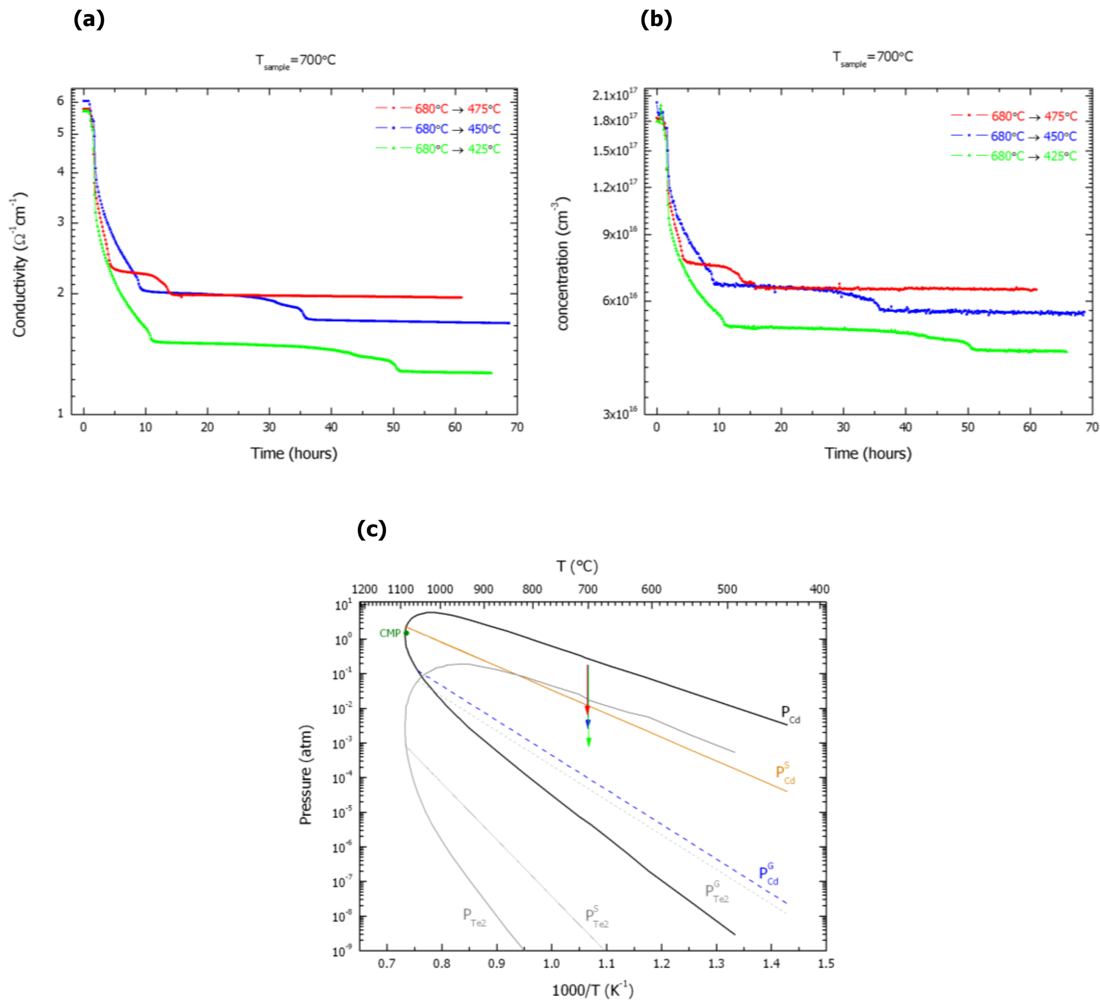

Fig.4.6: (a) The conductivity and (b) carrier concentration relaxation after pressure step-like changes from the same higher P_{Cd} to different lower P_{Cd}. Pressure is represented by the temperature of the cadmium source. (c) is the *P-T* phase diagram (black line is the 3-phase line, orange line is the stoichiometry line and dashed blue line is the sublimation line), in which the arrows represent corresponding step-like pressure changes from figures (a) and (b).

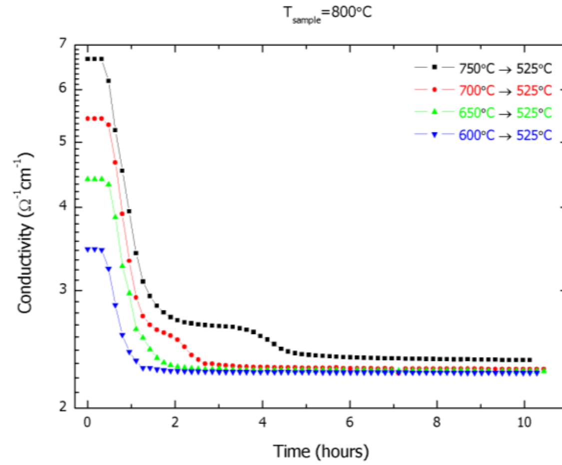

Fig.4.7: Relaxation of the conductivity after pressure step-like changes from different higher P_{Cd} to the same lower P_{Cd}. Pressure is represented by the temperature of the Cd source.

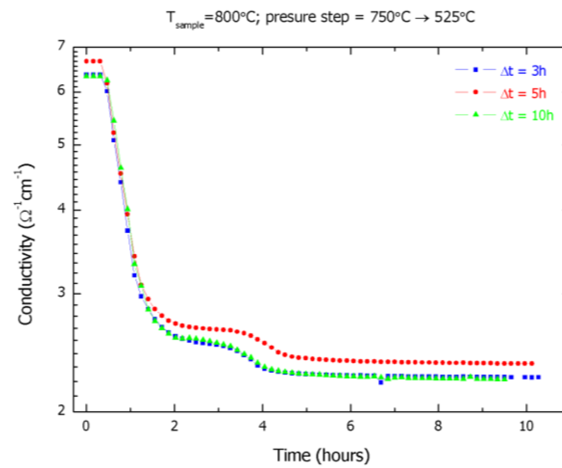

Fig.4.8: Relaxation of the conductivity after pressure step-like changes from the same P_{Cd} to the same lower P_{Cd} after different time of dwell Δt at higher pressure before the pressure step-like change. Pressure is represented by the temperature of the Cd source.

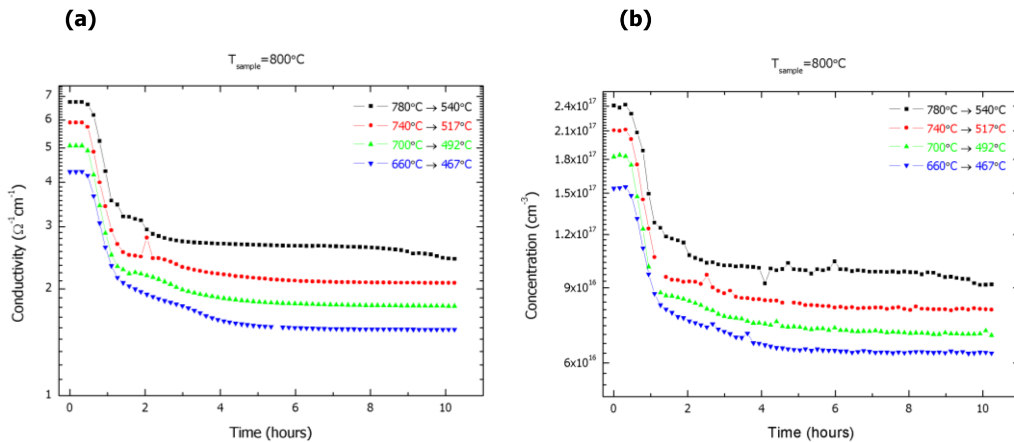

Fig.4.9: (a) The conductivity and (b) carrier concentration relaxation after pressure step-like changes from different higher P_{Cd} to different lower P_{Cd} keeping the pressure difference constant ΔP=30x. Pressure is represented by the temperature of the cadmium source.

4.4. "*In-situ*" measurement of the second Te-rich annealing during two-step annealing

In the chapter 3.5. a two-step annealing treatment of CdTe:Cl crystals was used for the Te inclusion elimination and consequent resistivity restoration. Here the second Te-rich re-annealing process is investigated on CdTe:Cl sample using the "*in-situ*" Hall effect measurements. The sample from VGF-3 crystal with as-grown resistivity $2\times10^{9}\Omega$cm was pre-annealed by a standard Cd-rich annealing at conditions 800/750°C for 24 hours with a cooling rate of 1°C/min. (see the chapter 3.5.). The sample annealed in a Cd atmosphere exhibited resistivity $\rho<0.1$ Ωcm and carrier concentration $n = 2\times10^{17}cm^{-3}$. After this treatment, "*in-situ*" Hall effect measurements of the second Te-rich re-annealing step was performed. The measurements were performed at 700°C for 24 hours with temperature of the Te source 600°C followed by a cooling rate of 0.8°C/min. These conditions were the same as in case of a standard Te-rich re-annealing. Fig.4.10 shows the time evolution of the conductivity, carrier concentration and mobility during the second Te-rich annealing. During the heating up (between the 1st and 4th hour) the electrical properties were determined by properties of the sample after the first Cd-rich annealing. This can be seen especially in Fig.4.10b, where the carrier concentration exhibits a value of about $\sim2\times10^{17}cm^{-3}$. After the temperature stabilization at annealing conditions 700/600°C (temperature of the sample/Te source) all three electrical parameters of the material were set to values which were in equilibrium with outside Te pressure and exhibited the n-type conductivity. During the following slow cooling down to the room temperature a conversion of the material into the p-type conductivity was observed at temperature approximately 450°C (clearly visible in Figs.4.10b,c). After the conversion, the conductivity of the material slightly decreased (see Fig.4.10a, at time later than the 37th hour) and finally reached the value of $\sim10^{-2}\Omega^{-1}cm^{-1}$. Final resistivity of the sample ($\rho\sim10^{2}\Omega$cm) was seven order of magnitude lower than after the standard annealing treatment without welded contacts ($\rho\sim10^{9}\Omega$cm) using the same annealing conditions. This large discrepancy can be explained by a contamination of the material during the "*in-situ*" measurement by acceptor-like impurities (probably potassium) from tungsten wires. This can lead to disturbance of the compensation balance resulting in a final low resistive p-type material. However, it is expected that the basic behavior of the electrical properties during the second Te-rich re-annealing remains unchanged despite of the presence of an acceptor-like impurity.

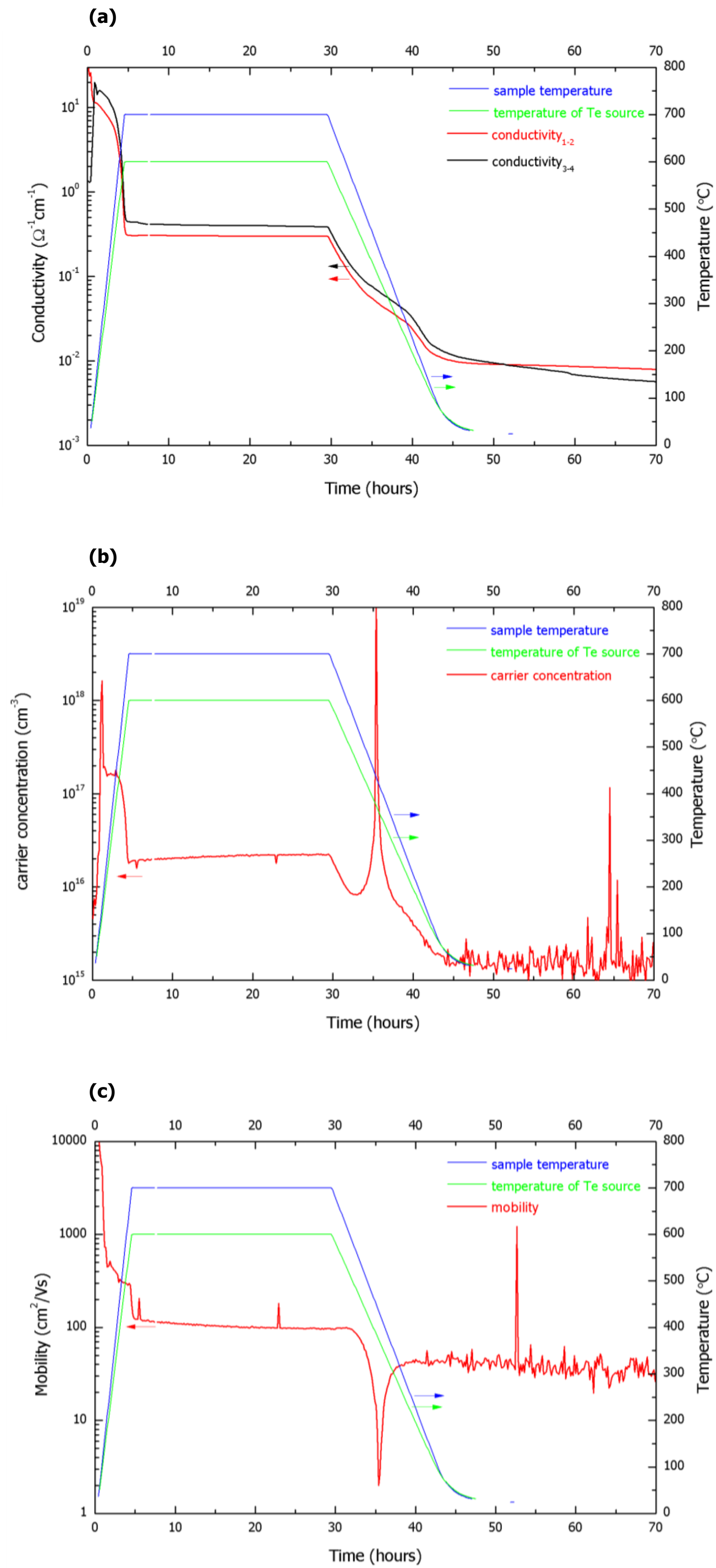

Fig.4.10: "*In-situ*" measurements of (a) the conductivity, (b) carrier concentration and (c) mobility during Te-rich annealing of CdTe:Cl sample pre-annealed in a Cd atmosphere.

4.5. Summary

"*In-situ*" high-temperature Hall effect measurements were performed on undoped CdTe, CdTe:In and CdTe:Cl with the aim of detailed characterization of the material electrical properties in the temperature range of 450-1000°C. A large number of new experimental values measured on undoped and slightly In-doped CdTe were obtained in conductivity(P_{Cd}) and carrier concentration(P_{Cd}) diagrams at Te-rich pressures in the range of 500-900°C and at Cd-rich pressures at low temperatures (450-600°C). Deviations from the defect model described in the literature were attributed to the contamination of the samples by an acceptor-like impurity during the "*in-situ*" measurements. Moreover, a non-standard double relaxation of the conductivity and carrier concentration in CdTe:Cl was observed during measurements, in which the partial cadmium pressure was lowered by a large pressure step-like change. Observed metastable state was investigated in dependence on different parameters of the pressure step-like change. Observed double relaxation could be explained by a precipitation occurring during the large pressure-down-step proposed in the literature. Finally, the second Te-rich annealing step in a two-step annealing treatment of CdTe:Cl crystals was investigated by "*in-situ*" measurements. A conversion of the material from low resistive n-type to slightly resistive p-type was observed. Final resistivity of the sample was lower than the resistivity of the sample annealed by a standard annealing process using the same annealing conditions. The discrepancy can be explained by contamination of the material by an acceptor-like defect during the "*in-situ*" experiments.

5. Infrared transmittance of CdTe

5.1. Introduction

The infrared (IR) transmission has been usually investigated in CdTe as a complementary method for investigation of CdTe. Observed transmittance spectra have exhibited various characters and some common tendencies will be described here.

Many works have been focused on preparation of $Cd_{1-x}Zn_xTe$ (x=0.04) substrates for epitaxial growth resulting in back-illuminated HgCdTe/CdZnTe infrared detectors working at λ=10.6μm (0.124eV). Since the detected IR radiation is absorbed in HgCdTe epitaxial layer deposited on the back side of the substrate, radiation has to pass through the substrate and it is necessary to suppress the absorption of IR light in the substrate. Increase of the substrate IR transmission is usually achieved by annealing of the material under Cd overpressure [49]. This annealing step leads to increase of the transmittance to maximal values of 66% at λ=10.6μm. However, other material properties like electrical properties or the presence of second phase defects in annealed substrates were not investigated in detail in [49].

Other works were aimed at investigation of basic properties of doped CdTe crystals. Usually, the IR transmission was high in well compensated semi-insulating materials. Some works were focused on investigation of overdoped CdTe crystals by acceptors (P and Te in [75]; Na+Li in [76]) or donors (Al, B, In in [77]), which exhibited very strong p-type or n-type conductivity, respectively. These crystals exhibited decrease of the IR transmittance at energies below 0.2eV (λ>8μm), which was attributed to the free carrier absorption (FCA) phenomenon observed in crystals with the free carrier concentration (p or n) higher than $3\times10^{15}cm^{-3}$ [75,77,78] (see the chapter 1.11.2). In p-type crystals an additional decrease of the IR transmission at about 0.3eV inexplicable by the FCA was observed [75,76,78]. This additional temperature independent [75] decrease has been explained by Mie scattering of the IR radiation on Te precipitates with the size up to tens of nanometers [76,78,79,80]. This explanation was also supported by theoretical calculations [78,79]. The Mie scattering is a scattering mechanism based on scattering of the light with a wavelength λ, which is comparable with the dimension of the scattering object R: $\lambda \sim R$.

In this work, most of the study is aimed at investigation of the IR transmittance of crystals, whose electrical and structural properties were changed by an annealing treatment. Spectra modulations are mainly given by the applied annealing temperature, type and intensity of vapor overpressure and cooling rate after the annealing. Similar transmittance properties of $Cd_{0.96}Zn_{0.04}Te$ and undoped CdTe crystals are supposed. Moreover, an investigation of as-grown crystals heavily doped by In or Cl is carried out. The maximal theoretical transmittance in the band gap range is calculated based on Hlidek's data [81] and is plotted together with measured spectra.

5.2. Annealing followed by a slow cooling

One of the main demand for $Cd_{0.96}Zn_{0.04}Te$ used as substrate for epitaxial growth is as high as possible transmittance at λ=10.6μm (0.124eV) [49]. Since $Cd_{0.96}Zn_{0.04}Te$ substrates are undoped, the free carrier concentration of as-grown crystals is given mainly by two dominant groups of point defects - residual acceptor impurities and cadmium vacancies. The concentration of residual acceptor-like impurities (Na, Li, Cu..) is usually at level about $p \sim 10^{15}cm^{-3}$, the concentration of cadmium vacancies depends on the crystal growth process. If the crystal is prepared by the

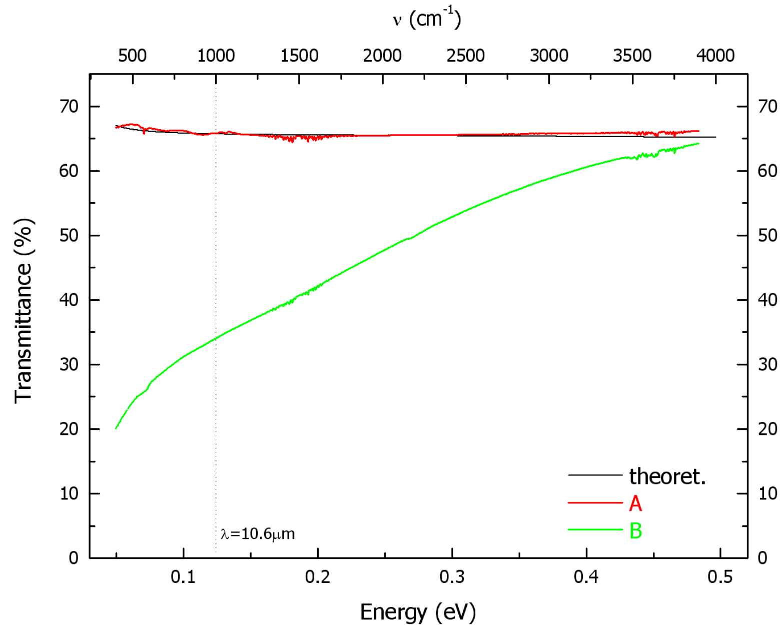

Fig.5.1: Typical IR transmittance spectra of Cd-rich (red line) and Te-rich (green line) CdTe crystals.

Bridgman method (or its modification) at high cadmium pressure P_{Cd}>1.2atm, grown ingot contains low concentration of V_{Cd} and exhibits the carrier concentration below 10^{15}cm^{-3}. The type of conductivity is given by residual donors and acceptors. Typical transmittance spectrum of such a crystal is plotted as a red line A in Fig.5.1 [49,80,82,83]. If the crystal contains tellurium enrichment (crystals prepared by the Bridgman technique or its modifications at low P_{Cd}<1.2atm), beside acceptor-like impurities the ingot contains also native acceptor V_{Cd} with concentration above 10^{15}cm^{-3}. Hence, the overall carrier concentration can reach even p=10^{16}cm^{-3} and typical IR transmittance spectrum of such Te-rich crystal is plotted as a green line B in Fig.5.1 [76,78,83].

The line C in Fig.5.2 shows typical IR transmittance spectrum in the energy range of 0.5-

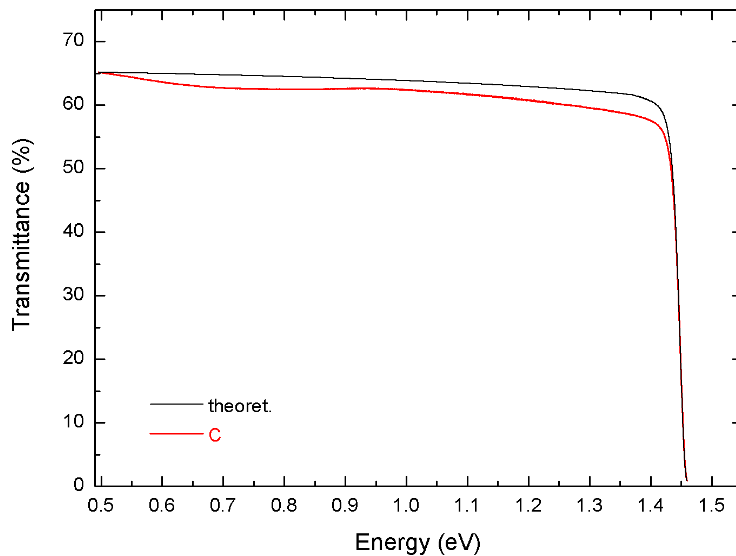

Fig.5.2: Red line represents a typical IR transmittance of the most of investigated as-grown undoped CdTe, CdZnTe, CdTe:In and CdTe:Cl samples as well as samples cooled slowly (<2°C/min.) after the annealing.

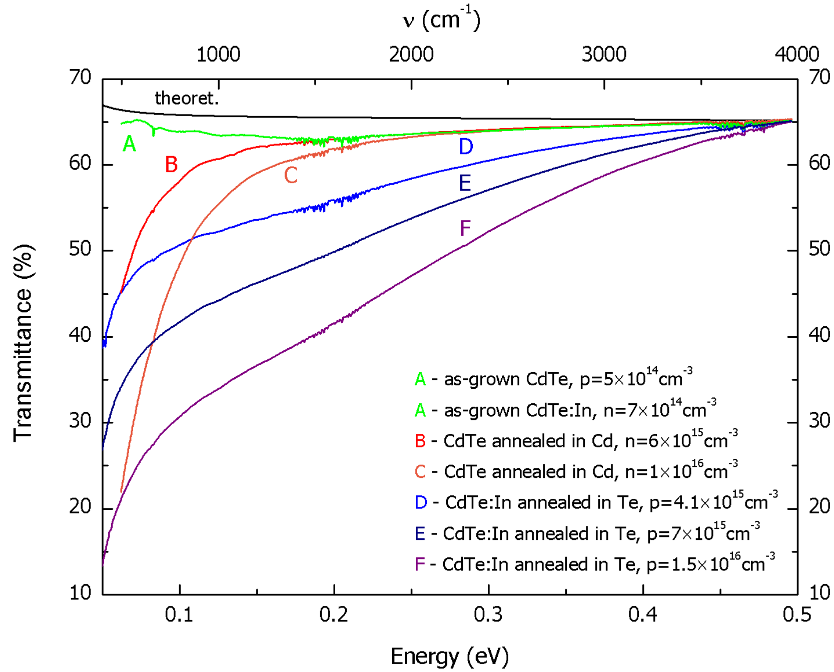

Fig.5.3: IR transmittance spectra of as-grown samples (line A), samples annealed in Cd vapor (lines B and C) and samples annealed in a Te atmosphere (lines D, E and F).

1.5eV for as-grown samples and samples annealed at temperature below 700°C with slow post-anneal cooling (<2°C/min.). It can be seen that measured spectra are very close to the theoretical limit. Similar spectra were also observed in as-grown samples with high density of Te inclusions with diameter up to 30μm. The density of inclusions was probably too low to affect the IR transmittance spectra by any type of absorption and their size was too large to affect the spectra by any type of scattering mechanism.

Annealing of Cd-rich and Te-rich undoped CdZnTe and CdTe crystals in a Cd atmosphere in the temperature range of 600-700°C for 24 hours followed by a slow cooling (<2°C/min.) led to an increase of the IR transmittance and spectra exhibited behavior as the line A in Fig.5.1 [49,80,82,83]. This can be explained by an annihilation of V_{Cd} by in-diffusion of Cd_i into the CdTe matrix during the Cd-rich annealing and resulting in a marked decrease of [V_{Cd}]. Hence, annealed samples exhibit usually the carrier concentration below 10^{15}cm^{-3}. When the applied annealing temperature during the Cd-rich annealing was higher than 850°C, a decrease of the IR transmittance at energies below 0.2eV was observed (see lines B and C in Fig.5.3) [83]. In this case, the electron concentration of annealed samples was higher than n=3×10^{15}cm^{-3} and the free carrier absorption was activated. Since the diffusion of native defects, especially Cd_i under Cd-rich conditions, is very fast at temperature above 850°C, [Cd_i] quickly decreases during post-anneal cooling and the carrier concentration higher than 3×10^{15}cm^{-3} of samples cooled back to the room temperature is rather caused by a diffusion of donor-like impurities from the annealing ampoule to the sample during the high-temperature annealing. The origin of impurities is not clear.

Annealing of undoped samples under Te overpressure was performed in the temperature range of 700-850°C. Annealed samples exhibited the final p-type concentration p=2×10^{16}cm^{-3} independently on applied annealing conditions (sample temperature, Te pressure) and transmittance spectra were similar to the line B in Fig.5.1 [76,78,83]. To find more significant dependence of the IR transmittance on annealing conditions in samples annealed in Te vapor, slightly In-doped CdTe

with $n=7\times10^{14}cm^{-3}$ were used for annealing experiments. Obtained spectra are plotted as lines D, E and F in Fig.5.3 [83]. Since the concentration of dominant donor level In_{Cd} in CdTe:In was constant, the final p-type concentration of samples was given by $[V_{Cd}]$ and $[Te_{Cd}]$ modulated by applied Te-rich annealing conditions. The final spectra can be analyzed by taking into account interplay of the FCA phenomenon (E<0.2eV) and scattering of the IR radiation on Te nanoparticles (E=0.2-0.4eV).

5.4. Annealing followed by a fast cooling

The next part of experiments was focused on high-temperature annealing of undoped samples under Cd or Te overpressure followed by a fast post-anneal cooling (>5°C/min. or quenching in the air) [83]. Annealing of the samples in Cd vapor in the temperature range of 850-1030°C for 24 hours followed by fast cooling led to a non-standard absorption at energies higher than 0.5eV (see the line B in Fig.5.4). The absorption did not exhibit any temperature dependence in the range of 5.6-300K, except the transmission modulation at about 0.85eV. In addition, high density of small (estimated size ~1μm) Cd precipitates created during (>5°C/min.) fast post-anneal cooling and examined by IR microscopy (Fig.5.5b) was observed in annealed samples. Hence, the non-standard decrease of the IR transmittance can be rather explained by the Mie scattering mechanism of the IR light on Cd precipitates than by any type of the absorption mechanism. The explanation of temperature modulation around 0.85eV is not clear at this moment.

In all samples annealed in Cd vapor followed by a slow cooling, the electron concentration increased with applied annealing temperature and Cd pressure. However, the quicker cooling after the annealing was, the lower electron concentration and larger density of Cd precipitates were found. This effect can be explained by enhanced capture of donor-like extrinsic defects in precipitates. Therefore, only charged particles on the surface of precipitates are electrically active and contribute to the electrical conductivity.

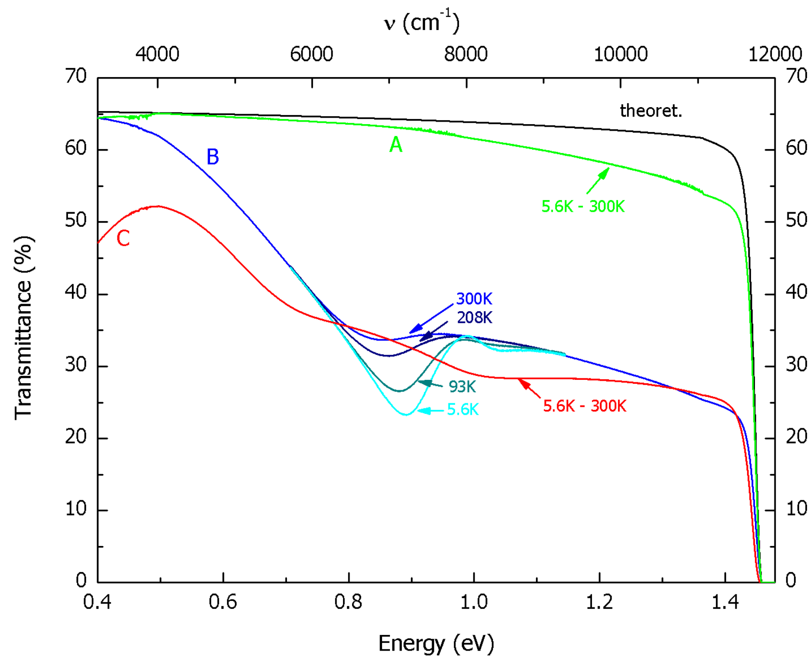

Fig.5.4: IR transmittance of as-grown sample (line A), sample quenched after Cd-rich annealing (line B) and sample quenched after Te-rich annealing (line C).

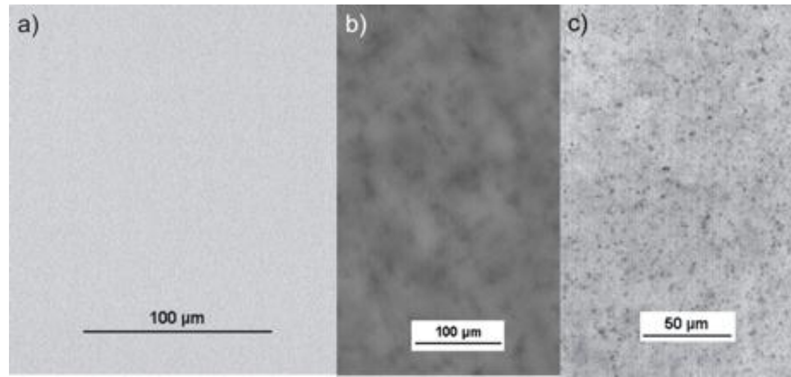

Fig.5.5: IR microscope images of (a) as-grown sample without any second phase defects, (b) sample quenched after the Cd-rich annealing in the temperature interval 900-1030°C for 24 hours and containing Cd precipitates and (c) sample quenched after Te-rich annealing in the temperature range of 700-850°C for 24 hours and containing Te precipitates.

Quenching of samples annealed in Te vapor also led to an occurrence of a non-standard absorption in the transmittance spectra at energies above 0.5eV (line C in Fig.5.4). In samples annealed in a Te atmosphere no temperature dependence was found. Moreover, in all quenched samples a large density of Te precipitates formed probably by precipitation of V_{Cd} and Te_{Cd} with size around 1µm was observed (Fig.5.5c). Similarly as in Cd-rich case, the non-standard absorption can be rather attributed to the scattering of the IR light on Te precipitates than to any type of absorption mechanism.

5.5. As-grown crystals highly doped by In and Cl

Samples from highly doped CdTe:In and CdTe:Cl were cut from different parts of CdTe:In and CdTe:Cl ingot to investigate their IR transmittance behavior. The dopant concentration in both crystals exceeded all other point defects present in crystals and the free carrier concentration of samples was n=[In] and n=[Cl], respectively, and was in good agreement with the segregation

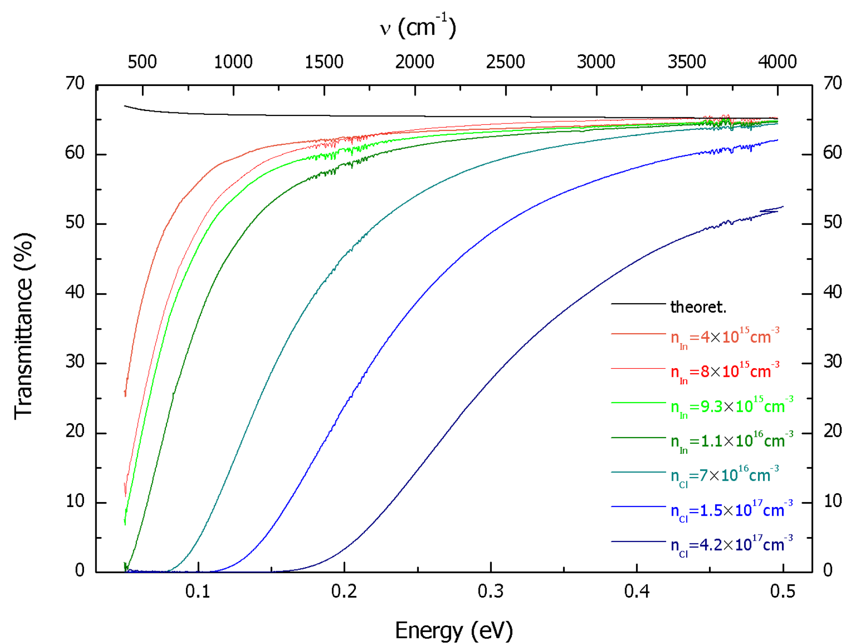

Fig.5.6: IR transmittance of highly doped CdTe:In and CdTe:Cl.

coefficients of In and Cl in CdTe crystals [18]. The IR transmittance spectra measured at energies below 0.5eV are shown in Fig.5.6 [83]. The IR transmittance at low energies decreased proportionally with increasing free carrier concentration of samples and can be described by the FCA phenomenon. No additional absorption was observed at energies above 0.5eV and spectra followed the theoretical transmittance values (see the line C in Fig.5.2). The additional absorption above 0.2eV observed in some studies [84] in heavily doped CdZnTe crystals usually attributed to a scattering of IR light on Te precipitates was not observed in CdTe crystals investigated in this work. Hence, the additional absorption observed in [84] can be connected with the presence of Zn in the CdTe lattice. However, no more detail investigation of heavily doped CdZnTe crystals was carried out.

Similar spectra as in Fig.5.6 were also observed in semi-insulating CdTe:In and CdTe:Cl annealed in Cd vapor. In these crystals a good initial compensation was disturbed by a Cd annealing resulting in samples with high free electron concentration given by dominant donor-like point defect In_{Cd} or Cl_{Te}, respectively.

5.6. Absorption coefficient analysis

From measured transmittance spectra additional information about the mechanism of the free carrier absorption (FCA) can be determined. The analysis is based on the evaluation of the slope, when the absorption coefficient versus wavelength is plotted. Calculated values of the exponent for three typical spectra modulated by the FCA are shown in Fig.5.7. Spectra of highly doped CdTe:In and CdTe:Cl samples exhibited m=2.68 (black line in Fig.5.7), what can be explained by the FCA on optical phonons. Even if samples contained [Cl]~ 4×10^{17}cm^{-3}, no change of the exponent and simultaneously the absorption mechanism was found. Undoped CdTe and CdZnTe samples annealed in a Cd atmosphere at temperature above 850°C exhibited similar exponent m=2.72 connected with the FCA on phonons (blue line in Fig.5.7). A non-standard exponent m=0.74 was found in Te-rich crystals and in samples annealed in Te vapor (red line in Fig.5.7). The reason for this result cannot be explained within the theoretical predictions and remains unclear.

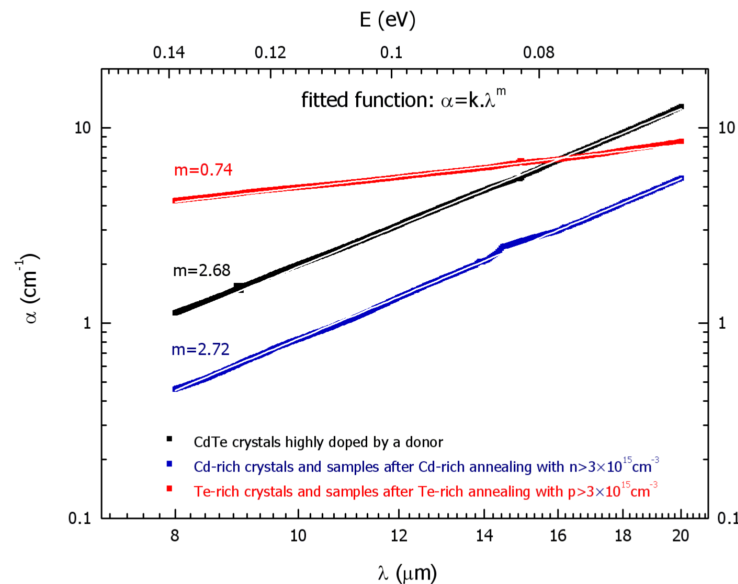

Fig.5.7: An analysis of the absorption coefficient α of various types of CdTe/CdZnTe samples.

5.7. Summary

IR transmittance spectroscopy is one of the typical optical characterization method describing CdTe-based crystals. Values of IR transmission at about λ=10μm are crucial for $Cd_{0.96}Zn_{0.04}Te$ substrates used for preparation of HgCdTe infrared detectors. Transmittance properties of different types of as-grown CdTe-based material were in detail investigated. Moreover, the properties of crystals were modified by an application of various annealing treatments. From obtained results, few characteristic tendencies of IR transmittance spectra can be distinguished.

Very good correlation between obtained spectra and measured free carrier concentration of samples highly doped by donor-like dopants (In or Cl) was found and observed dependence was attributed to the free carrier absorption mechanism. Similar results were obtained after annealing of semi-insulating CdTe:In and CdTe:Cl samples annealed in Cd atmosphere and also in undoped CdTe samples annealed in Cd vapor at high temperature followed by slow post-anneal cooling.

Typical "Te-rich" spectrum at energies below 0.5eV was found in as-grown Te-rich crystals with $p>3\times10^{15}cm^{-3}$ and in samples annealed in Te vapor. The spectrum was modulated by interplay of the FCA mechanism and scattering of the IR light on Te nanoparticles.

A non-standard absorption at energies above 0.5eV was observed in samples quenched after high temperature annealing in Cd (or Te) atmosphere. The absorption was attributed to Mie scattering of the IR radiation on Cd (or Te) precipitates with the size about 1μm observed in quenched samples by IR microscopy.

Conclusions

The dissertation was focused on investigation of structural, electrical and optical properties of CdZnTe substrates for epitaxial growth and CdTe/CdZnTe bulk detectors of X-ray and gamma-ray radiation. As-grown samples were investigated by various characterization techniques and their properties were modified by an annealing treatment. The quality of both types of materials is strongly affected by the presence of the second phase defects – inclusions. Two types of inclusions were identified in CdTe/CdZnTe crystals – cadmium and tellurium inclusions. Their size and density was successfully reduced by application of a suitable post-growth annealing in a cadmium/tellurium overpressure. Moreover, an application of a slow post-anneal cooling was necessary for suppression of Cd/Te precipitates formation. In case of the substrate-grade $Cd_{0.96}Zn_{0.04}Te$ material, an annealing in Cd vapor at temperature below 850°C was found to be effective for increase of the infrared transmittance near application interesting region λ=10.6μm. On the other hand, CdTe/CdZnTe detectors contain usually Te inclusions and Cd-rich annealing was applied for their elimination. However, this thermal treatment led to a significant decrease of the material resistivity and re-annealing of the material in a Te atmosphere was necessary for the high-resistivity restoration. This reproducible method was found to be effective in CdTe:Cl crystals with [Cl]=2×10^{17}cm^{-3}. However, another important parameter of CdTe-based radiation detectors – mobility-lifetime product – markedly dropped after application of a two-step annealing on commercially produced detectors. Hence, study of the annealing conditions leading to improvement of the detection ability of semi-insulating CdTe:Cl crystals should follow.

The next part of the work was focused on investigation of transport properties of CdTe crystals directly at high temperatures. The measurements were performed at various temperatures and partial pressures. Obtained data were in good agreement with the theoretical calculations published in the literature. In addition, a non-standard double relaxation after a large step-like change of pressure to lower P_{Cd} was observed and investigated. Obtained data can be used as a feed-back for crystal growers for optimization of the crystal growth process, provide a deep understanding of electrical properties during cooling of the crystal and can be also used for optimization of post-growth annealing conditions (temperature, time, post-anneal cooling rate..) leading to improvement of the material properties.

In the last part of the thesis, an effect of high-temperature annealing followed by various cooling regimes on the infrared transmittance of CdTe-based materials was investigated. Crystals with the carrier concentration above 3×10^{15}cm^{-3} exhibited decrease of the infrared transmittance at low energies attributed to the free carrier absorption. A non-standard decrease of the transmittance was observed in the samples, which were quenched after the annealing. Obtained results give an extensive review of physical phenomena affecting the IR transmittance behavior. Results can be used for improvement of the annealing conditions leading to a maximization of the IR transmittance in application interesting infrared regions.

To conclude, this work attempts to provide a comprehensive understanding of the annealing processes and to investigate the effect of annealing conditions on structural, electrical and optical properties of bulk CdTe-based crystals.

In future continuation of the research an optimization of a two-step annealing treatment of semi-insulting CdTe:Cl detectors should be performed resulting in improvement of the detection ability, especially improvement of the mobility-lifetime product. This research should be supported by further high-temperature "*in-situ*" Hall effect measurements with purified tungsten wires. These

experiments with as pure as possible wires can provide additional information about the point defects behavior at high temperatures and also optimize the annealing conditions. On the other hand, obtained knowledge from annealing and infrared transmittance experiments can be utilized in measurements of the position of the absorption edge of CdTe in the temperature interval 0-1000°C.

References

[1] D.de Nobel; *Philips Res. Repts.* **14**, 361 (1959); **14**, 430 (1959)

[2] D.M.Henderson, R.L.Abrams; *Optics Commun.* **2**, 223 (1970)

[3] P.Norton; *Opto-electronics review* **10**, 159 (2002)

[4] A.Rogalski; *Rep. Prog. Phys.* **68**, 2267 (2005)

[5] W.D.Lawson, S.Nielson, E.H.Putley, A.S.Young; *J. Phys. Chem. Solids* **9**, 325 (1959)

[6] J.J.Kennedy, P.M.Amirtharaj, P.R.Boyd, S.B.Quadri, R.C.Dobbyn, G.G.Long; *J. Cryst. Growth* **86**, 93 (1988)

[7] H.R.Vydyanath, J.Ellsworth, J.J.Kennedy, B.Dean, C.J.Johnson, G.T.Neugebauer, J.Sepich; *J. Vac. Sci. Technol.* **B10**, 1476 (1992)

[8] S.Sen, C.S.Liang, D.R.Rhiger, J.E.Stannard, H.F.Arlinghaus; *J. Electron. Mater.* **25**, 1188 (1996)

[9] C.Szeles; *phys. stat. sol. (b)* **241**; 783 (2004)

[10] R.Triboulet, P.Siffert; *„CdTe and related compounds: physics, defects, hetero- and nano-structures, crystal growth, surfaces and applications – Part I.: physics, CdTe-based nanostructures, semimagnetic semiconductors, defects“* Elsevier 2010

[11] J.R.Chelikowsky, M.L.Cohen; *Phys. Rev. B* **14**, 556 (1976)

[12] R.Balasubramanian, W.R.Wilcox; *Mater. Sci. Engineer. B* **16**, 1 (1993)

[13] P.Norton; *Opto-electron. Rev.* **10**, 159 (2002)

[14] G.H.Su; *J. Appl. Phys.* **103**, 084903 (2008)

[15] S.Gilliland, J.Gonzalez, H.S.Gueder, A.Segura, I.Mora, V.Munoz; *phys. stat. sol. (b)* **235**, 441 (2003)

[16] D.A.Porter, K.E.Easterling; *Phase Transformations in Metals and Alloys*; ISBN 0748757414, Nelson Thornes Ltd. (2001)

[17] P.Kratochvil, P.Lukac, B.Sprusil; *Introduction to physics of metals I.*; SNTL (1984) (in Czech)

[18] K.Zanio; *J. Electron. Mater.* 3, 327 (1974)

[19] J.H.Greenberg; *Prog. Cryst. Growth. Char. Mater.* **47**, 196 (2003)

[20] A.Haloui, Y.Feutelais, B.Legendre; *J. Alloys Comp.* **260**, 179 (1997)

[21] R.Grill, A.Zappettini; *Prog. Cryst. Growth Char. Mater.* **48/49**, 209 (2004)

[22] R.Fang, R.F.Brebrick; *J. Phys. Chem. Solids* **57**, 443 (1996)

[23] F.A.Kröger; *The Chemistry of Imperfect Crystals*; North-Holland Publishing Company, 2nd edition, 1974

[24] S.H.Wei, S.B.Zhang; *phys. stat. sol. (b)* **229**, 305 (2002)

[25] J.Kubát; *Diploma thesis: Photoelectric spectroscopy of deep electronic levels in high-resistance CdTe*; Charles University in Prague (2006)

[26] *Properties of Narrow Gap Cadmium-based Compounds*, edited by P. Capper, Institution of Electrical Engineers, London (1994)

[27] J. Schreiber, L. Höring, H. Uniewski, S. Hildebrandt, H. S. Leipner; *phys. stat. sol. (a)* **171**, 89 (1999)

[28] P.D.Brown, K.Durose, G.J.Russel, J.Woods; *J. Cryst. Growth* **101**, 211 (1990)

[29] P.Rudolph; *Cryst. Res. Technol.* **38**, 542 (2003)

[30] E.Belas, M.Bugár, R.Grill, J.Franc, P.Moravec, P.Hlídek, P.Höschl; *J. Electron. Mater.* **37**, 1212 (2008)

[31] K.Zanio; *J. Appl. Phys.* **41**, 1935 (1970)

[32] R.Grill, B.Nahlovskyy, E.Belas, M.Bugár, P.Moravec, P.Höschl; *Semicond. Sci. Technol.* **25**, 045019 (2010)

[33] U.Roessler; *Systematics of Semiconductor Data*, Springer (2008)

[34] P.Horodyský; *Dissertation thesis Optical properties of $Cd_{1-x}Zn_xTe$*; Institute of Physics, Charles University in Prague, 2007

[35] R.D.S.Yadava, B.S.Sundersheshu, M.Anandan, R.K.Bagai, W.N.Borle; *J. Electron. Mater.* **23**, 1349 (1994)

[36] G.F.Knoll; *"Radiation Detection and Measurement"*, John Wiley & Sons Inc.; Third Edition 2000

[37] J.Kubát, J.Franc, R.Grill, P.Horodyský, P.Hlídek, E.Belas; *J. Electron. Mater.* **36**, 871 (2007)

[38] B.Nahlovskyy; *Dissertation thesis*: *The study of chemical diffusion and properties of electric contacts on CdTe for gamma ray detector applications*; Institute of Physics, Charles University in Prague (2010)

[39] M.Ohmori, Y.Iwase, R.Ohno; *Mater. Sci, Eng.* **B16**, 283 (1993)

[40] COREMA-WT, Hardware user manual, SemiMap GmbH, Germany, Version 2008-1 (Charles University)

[41] P.Hlidek; *Infrared spectroscopy – practicum*, Charles University (2004) (in Czech)

[42] P.Rudolph, A.Engel, I.Schnetke, A.Grochovski; *J. Cryst. Growth* **147**, 297 (1995)

[43] H.G.Brion, C.Mewes, I.Hahn, U.Schäufele; *J. Cryst. Growth* **134**, 281 (1993)

[44] M.Wada, J.Suzuki; *Jap. Journ. Appl. Phys.* **27**, L972 (1988)

[45] J.Shen, D.K.Aidun, L.Regel, W.R.Wilcox; *J. Cryst. Growth* **132**, 250 (1993)

[46] J.R.Heffelfinger, D.L.Medlin, R.B.James; *SPIE* **3446**, 49 (1988)

[47] G.A.Carini, A.E.Bolotnikov, G.S.Camarda, G.W.Wright, R.B.James, L.Li; *Appl. Phys. Lett.* **88**, 143515 (2006)

[48] W.J.Kim, M.J.Park, S.U.Kim, T.S.Lee, J.M.Kim, W.J.Song, S.H.Suh; *J. Cryst. Growth* **104**, 677 (1990)

[49] S.Sen, D.R.Rhiger, C.R.Curtis, M.H.Kalisher, H.L.Hettich, M.C.Curie; *J. Electron. Mater.* **30**, 611 (2001)

[50] J.Shen, D.K.Aidun, L.Regel, W.R.Wilcox; *Mater. Sci. Eng. B* **16**, 182 (1993)

[51] H.R.Vydyanath, J.A.Ellsworth, J.B.Parkinson, J.J.Kennedy, B.Dean, C.J.Johnson, G.T.Neugebauer, J.Sepich, P.K.Liao; *J. Electron. Mater.* **22**, 1073 (1993)

[52] T.S.Lee, J.W.Park, Y.T.Jeoung, H.K.Kim, C.H.Chun, J.M.Kim, I.H.Park, J.M.Chang, S.U.Kim, M.J.Park; *J. Electron. Mater.* **24**, 1053 (1995)

[53] M.Ayoub, M.Hage-Ali, A.Zumbiehl, R.Regal, J.M.Koebel, C.Rit, P.Fougeres, P.Siffert; *IEEE Trans. Nucl. Sci.* **49**, 1954 (2002)

[54] M.Ayoub, M.Hage-Ali, J.M.Koebel, A.Zumbiehl, F.Klotz, C.Rit, R.Regal, P.Fougeres, P.Siffert; *IEEE Trans. Nucl. Sci.* **50**, 229 (2003)

[55] E.Belas, M.Bugár, R.Grill, P.Horodyský, R.Feš, J.Franc, P.Moravec, Z.Matěj, P.Höschl; *J. Electron. Mater.* **36**, 1025 (2007)

[56] M.Bugár, E.Belas, R.Grill, J.Procházka, Š.Uxa, P.Hlídek, J.Franc, R.Fesh, P.Höschl; *IEEE Trans. Nucl. Sci.* (2011) – Article accepted for publication

[57] B.K.Meyer, W.Stadler; *Journ. Cryst. Growth* **161**, 119 (1996)

[58] M.A.Berding; *Phys. Rev. B* **60**, 8943 (1999)

[59] R.F.Brebrick; *J. Electron. Mater.* **33**, L24 (2004)

[60] E.Belas, M.Bugár, R.Grill, J.Franc, P.Höschl; *IEEE Trans. Nucl. Sci.* **56**, 1758 (2009)

[61] R.Grill, P.Fochuk, J.Franc, B.Nahlovskyy, P.Höschl, P.Moravec, Z.Zakharuk, Ye. Nykonyuk, O.Panchuk; *phys. stat.sol. (b)* **243**, 787 (2006)

[62] J.Hamann, A.Burchard, M.Deicher, T.Filz, V.Ostheimer, F.Strasser, H.Wolf, ISOLDE Collaboration, Th.Wichert; *Physica B* **273**, 870 (1999)

[63] E.Molva, J.M.Francou, J.L.Pautrat, K.Saminadayar, L.S.Dang; *J. Appl. Phys.* 56, 2241 (1984)

[64] J.Procházka, E.Belas, R.Fesh, J.Franc, P.Hlídek; *Nucl. Instr. and Meth. A*, in Press (2010), doi: 10.1016/j.nima.2010.06.131

[65] R.C.Whelan, D.Shaw; *phys. stat. sol.* **29**, 145 (1968)

[66] F.T.J.Smith; *Metallurg. Trans.* **1**, 617 (1970)

[67] F.A.Selim, V.Swaminathan, F.A.Kröger; *phys. stat. sol. (a)* **29**, 465 (1975)

[68] S.S.Chern, H.R.Vydyanath, F.A.Kröger; *J. Solid State Chem.* **14**, 33 (1975)

[69] S.S.Chern, H.R.Vydyanath, F.A.Kröger; *J. Solid State Chem.* **14**, 44 (1975)

[70] S.S.Chern, H.R.Vydyanath, F.A.Kröger; *J. Solid State Chem.* **14**, 299 (1975)

[71] P.Fochuk, R.Grill, O.Panchuk; *J. Electron. Mater.* **35**, 1354 (2006)

[72] R.Grill, J.Franc, P.Höschl, I.Turkevych, E.Belas, P.Moravec; *IEEE Trans. Nucl. Sci.* **52**, 1925 (2005)

[73] *CRC Handbook of Chemistry and Physics*; D.R.Lide, Ed.; 79th ed. Boca Raton, FL: CRC (1998)

[74] Yu.V.Rud, K.V.Sanin; *Sov. Phys. Semicond.* 6, 764 (1972)

[75] V.Čápek, K.Zimmerman, Č.Koňák, M.Popova, P.Polívka; *phys. stat. sol. (b)* **56**, 739 (1973)

[76] A.Koyama, A.Hichiwa, R.Hirano; *J. Electron. Mater.* **28**, 683 (1999)

[77] B.M.Vul, A.F.Plotnikov, V.M.Salman, A.A.Sokolova, V.A.Chapnin; *Sov. Phys. Semicond.* **2**, 1045 (1969)

[78] U.Becker, P.Rudolph, R.Boyn, M.Wienecke, I.Utke; *phys. stat. sol. (a)* **120**, 653 (1990)

[79] R.D.S.Yadava, B.S.Sundersheshu, M.Anandan, R.K.Bagai, W.N.Borle; *J. Electron. Mater.* **23**, 1349 (1994)

[80] L.Yujie, G.Zhi, L.Guoqiang, J.Wanqi; *J. Electron. Mater.* **33**, 861 (2004)

[81] P.Hlídek, J.Bok, J.Franc, R.Grill; *J. Appl. Phys.* **90**, 1672 (2001)

[82] B.Li, J.Zhu, X.Zhang, J.Chu; *J. Cryst. Growth* **181**, 204 (1997)

[83] M.Bugár, E.Belas, J.Procházka, P.Hlídek, R.Grill, J.Franc, P.Höschl; *Nucl. Instr. and Meth. A*, Article in Press (2011), doi: 10.1016/j.nima.2010.06.130

[84] Q.Li, W.Jie, L.Fu, T.Wang, G.Yang, X.Bai, G.Zha; *J. Cryst. Growth* **295**, 124 (2006)